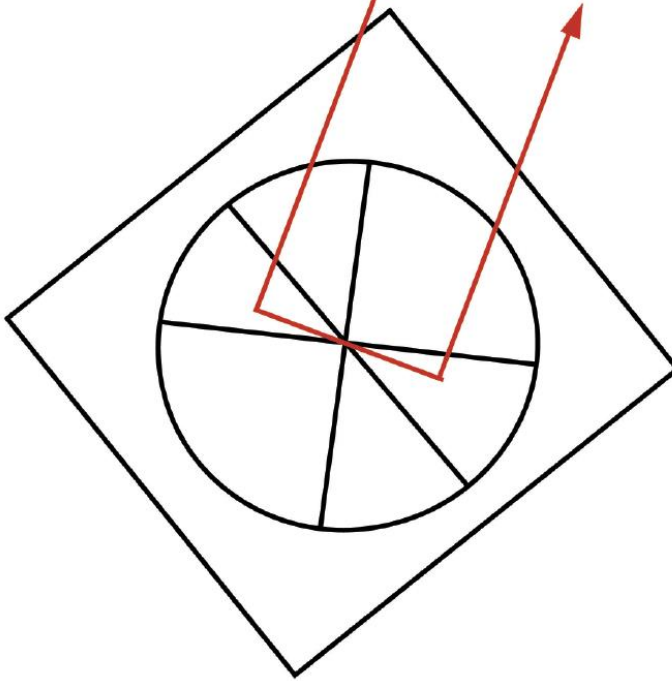


# Laser Metrology and Machine Performance XIV



Edited by: A. Archenti & L. Blunt



***LASER METROLOGY  
AND  
MACHINE PERFORMANCE XIV***

14<sup>th</sup> International Conference and Exhibition on Laser  
Metrology, Machine Tool, CMM & Robotic Performance

**Lamdap 2021**

Organised by:



Sponsors:



## Conference Chairmen

Professor Liam Blunt  
University of Huddersfield, UK

Professor Andreas Archenti  
KTH Royal Institute of Technology, Sweden

## Additional members of the Organising Committee

Prof. Andrew Longstaff, University of Huddersfield, UK  
Prof. BG Rosén, Halmstad University, SE

## Scientific Committee

Prof. A. Archenti, KTH Royal Institute of Technology, Sweden  
Prof. L. Blunt, University of Huddersfield, UK  
Dr H. Bosse, Physikalisch-Technische Bundesanstalt (PTB)  
Germany  
Prof. K. Cheng, Brunel University London, UK  
Dr W. Knapp, Engineering Office Dr. W. Knapp, Switzerland  
Dr A. Longstaff, University of Huddersfield, UK  
Dr O. Riemer, Leibniz-Institut für Werkstofforientierte  
Technologien, Germany  
Dr H. Schwenke, Etalon, Germany  
Mr S. Smith, Aerotech Ltd, UK



***LASER METROLOGY  
AND  
MACHINE PERFORMANCE XIV***

Edited by Professor Liam Blunt & Professor Andreas Archenti

“Random results are the consequence of random procedures.”

Portas’ Law, Mr. G. Portas, CUPE

© euspen Headquarters March 2021  
Building 90, Cranfield University Campus  
Bedfordshire  
MK43 0AL  
UK  
[www.euspen.eu](http://www.euspen.eu)

ISBN: 978-0-9957751-8-3

## PREFACE

This text contains the papers presented at the Fourteenth International Conference on Laser Metrology, Coordinate Measuring Machine and Machine Tool Performance (LAMDMAP 2021) which was organised by **euspen** in collaboration with KTH Royal Institute of Technology, Sweden and hosted online from **euspen** headquarters Cranfield UK.

This year, the conference will focus on performance evaluation of machine tools, dimensional measurement, new developments in measurement and fabrication techniques and the rise of digital twins in machine tool and process technology. In particular the emergence of metal additive manufacturing as the route to precision components will be explored.

The organising committee have due to the online format decided to increase the number of keynote presentations for the conference and to allow our industrial colleagues to deliver invited keynotes and technical presentations. The keynotes will cover the future of global manufacturing and machine tool industry. Emerging metrology technologies and the movement to robotic machining. Increasing implementation of digital twins and data driven manufacturing software support system will be addressed in the keynotes. The theme of metal additive manufacturing will be reviewed in the context of dimensional measurement traceability by X-ray computed tomography and machine performance evaluation. An update on standards for machine tools will be given. A tutorial on metrology of machine tools and industrial robots geometry and compliance will be organized in connection to the conference.

We thank our sponsors, Heidenhain (GB) for providing the student scholarships, the companies forming the commercial presentations, the members of the Scientific Committee and the staff of **euspen** for their valuable support.

Professor Liam Blunt  
Conference Chairman

Professor Andreas Archenti  
Conference Co-Chairman

March 2021

## CONTENTS

### Keynotes

- The future of global manufacturing and machine tool industry** 13  
M. Mori  
*DMG MORI, JP*
- Metrology enabled robotic machining** 14  
P. Keogh  
*University of Bath, UK*
- Machine performance evaluation for metal additive manufacturing** 15  
S. Moylan  
*National Institute of Standards and Technology, US*
- Correction of thermo-elastic errors in machine tools – How digital twins help to minimize TCP deviations** 16  
S. Ihlenfeldt  
*Fraunhofer Institute for Machine Tools and Forming Technology IWU, DE*
- Enabling technologies for data and knowledge driven software services in manufacturing** 17  
T. McLeay  
*Sandvik Coromant, SE*
- Additive manufacturing with electrons** 18  
I. Laidler  
*Wayland Additive, UK*
- Next generation measurement sensors and the disconnect with traditional metrology requirements** 19  
C. Ivory, O. Noakes  
*Hexagon Manufacturing Intelligence, UK*

**Dimensional measurement traceability by X-ray  
computed tomography – where are we? 20**

M. Ferrucci

*National Institute of Standards and Technology, US*

**Invited Presenters**

**Recent developments in freeform grinding for large  
EUV lithography optics and head-up display mirrors  
using a bespoke tool path generation package,  
MöbiusCAMX 22**

M. Stocker

*Cranfield Precision, Division of Fives Landis Ltd, UK*

**Standards for machine tools, an update 23**

W. Knapp

*Engineering Office, Switzerland*

**Session 1: Machine Tools**

**Machine tool thermal state representation using  
modal analysis 25**

N. Ariaga, A.P. Longstaff, S. Fletcher, W. Pan

*Center for Precision Technologies, University of  
Huddersfield, Huddersfield, UK*

**Comparison of measured static and quasi-static  
deflections of industrial manipulators 35**

N.A. Theissen, M.K. Gonzalez, T. Laspas, A. Archenti

*KTH Royal Institute of Technology, Sweden*

**Quantitative assessment of machine tools precision states through fractal analysis of machine error parameters** 43

K. Xing<sup>1</sup>, X. Rimpault<sup>1,2</sup>, J.R.R. Mayer<sup>1</sup>, J-F. Chatelain<sup>2</sup>, S. Achiche<sup>1</sup>

<sup>1</sup>*Department of Mechanical Engineering, Polytechnique Montréal, Montréal, QC H3T 1J4, Canada*

<sup>2</sup>*Department of Mechanical Engineering, École de technologie supérieure, Montréal, QC H3C 1K3, Canada*

**Session 2: Design**

**Design of a structural strain measurement system based on slotted photomicrosensors** 54

S. Fletcher, D. Chuku, T. Furness, A.P. Longstaff  
*Center for Precision Technologies, University of Huddersfield, Huddersfield, UK*

**Modal analysis of a sensing CBN grinding wheel** 60

L. Hu, J. Zha, Z. Chen, M. Bilal, Y. Chen  
*School of Mechanical Engineering, Xi'an Jiaotong University, 28 Xianning Road, Xi'an, Shaanxi 710049, P.R. China.*

**Session 3: Process Control**

**Optimization of volumetric error calibration procedures based on a digital twin** 67

B. Iñigo<sup>1</sup>, N. Colinas-Armijo<sup>1</sup>, G. Aguirre<sup>1</sup>, L.N. López de Lacalle<sup>2</sup>

<sup>1</sup>*Design and Precision Engineering Group, IDEKO, 20870 Elgoibar, Basque Country, Spain*

<sup>2</sup>*Department of Mechanical Engineering, EHU-UPV, 48013 Bilbao, Basque Country, Spain*

- Background noise assessment of low-cost vibration sensors in precision manufacturing applications** 78  
A. Iqbal, N. S. Mian, A. P. Longstaff, S. Fletcher  
*Centre for Precision Technologies, University of Huddersfield, Queensgate, Huddersfield, HD1 3DH, UK*

#### **Session 4: Additive Manufacturing and Standards**

- Evaluation of the electron beam spot size in electron beam melting for additive manufacturing** 89  
Z. Lin, X. Zhao, S. Dadbakhsh, A. Rashid  
*Production Engineering Department, KTH Royal Institute of Technology, Brinellvägen 68, Stockholm 11428, Sweden*

#### **Session 5: Associated Measurement**

- Optical 3D measurement of cooling holes in gas turbine and aircraft engines** 94  
K. Zangl, R. Danzl, D. Urlep, F. Helmlí  
*Bruker Alicona, Austria*

- Novel signal processing module of Fabry-Perot interferometer** 99  
S-C. Chang<sup>1</sup>, Y-C. Wang<sup>1</sup>, C.-P Chang<sup>2</sup>, T-C. Wu<sup>1</sup>, B-Y. Lee<sup>3</sup>  
<sup>1</sup>*Department of Mechanical Engineering, National Yunlin University of Science and Technology, Yunlin 640, Taiwan*  
<sup>2</sup>*Department of Mechanical and Energy Engineering, National Chiayi University, Chiayi 600, Taiwan*  
<sup>3</sup>*Department of Mechanical and Computer-Aided Engineering, National Formosa University, Yunlin 632, Taiwan*

**Characterisation of an air plasma torch for in-situ  
surface processing**

**103**

K. Gobey<sup>1</sup>, A. Bennett<sup>1,2</sup>, N. Yu<sup>3</sup>, M. Castelli<sup>2</sup>, C.  
Sansom<sup>4</sup>, P. King<sup>4</sup>, T. Urayama<sup>5</sup>

<sup>1</sup>*Surface Engineering and Precision Institute, Cranfield  
University, UK*

<sup>2</sup>*Cranfield Plasma Solutions, UK*

<sup>3</sup>*Institute of Material and Processes, University of  
Edinburgh, UK*

<sup>4</sup>*Renewable Energy Systems Centre, Cranfield University,  
UK*

<sup>5</sup>*Adtec Plasma Technology Co., Ltd., Japan*

# Keynotes

## **The future of global manufacturing and machine tool industry**

Dr Masahiko Mori  
*DMG MORI, JP*

### **Abstract**

In the field of manufacturing, optimized machining process and its highly operable surroundings are the main drivers to maximize the whole productivity.

For decades, machining process has been improved in the course of the development of 5-axis or multi-axis machine tools as well as the process integration into single machine tool. It has now come to the era of automation and digitization, supported by the growing global demand for skilled operators, which is capable of unmanned operations and continuous monitoring, analysis and thus improvement of the process.

This presentation shows how the global manufacturing and machine tool industry have been changing, and how DMG MORI plays a role of a machine tool manufacturer who enables its customers worldwide take part in the continuous circle of productivity improvement.

## **Metrology enabled robotic machining**

Prof. Patrick Keogh  
*University of Bath, UK*

### **Abstract**

Serial-link industrial robots are relatively inexpensive systems that have large working volumes. They are used for many manipulative tasks, particularly those that are repetitive and do not depend on fine precision. Limitations arise from revolute joint backlash, friction and low stiffness, which induce nonlinear dynamic effects. Control using internal encoders is not generally effective for precision robotic machining, both for absolute positioning and relative surface finish. The robot control is generally of low bandwidth ( $< 10$  Hz) and not able to compensate for higher bandwidth dynamics induced by machining processes. It is possible to compensate for positioning errors by introducing external metrology, for example, using a laser tracker to monitor a tool path and providing additional feedback to the robot controller. Higher frequency compensation of machining processes requires additional actuation that is mobile with the robot motions. External inertial actuators close to the machine tool may be used to apply compensating dynamic forces. Laser tracker feedback of displacement signals may be adequate if vibration levels are within resolution, otherwise displacement roll-off with frequency may be covered by accelerometer signal feedback. The keynote will also address control strategies that are effective for such external metrology in reducing machining errors.

## **Machine performance evaluation for metal additive manufacturing**

Shawn Moylan

*National Institute of Standards and Technology, US*

### **Abstract**

A qualified additive manufacturing (AM) part will only come from a qualified AM machine, and machine qualification requires machine performance evaluation. Although additive manufacturing is a relatively new process and machines are continually changing, the test methods used in their performance evaluation can leverage expertise developed in other areas, especially machine tool metrology. Performance evaluation can take several approaches, from building and measuring a test artifact, to evaluating individual machine components, to a combination or hybrid approach. Best practices specific to additive manufacturing machines are currently under development and evaluation, but much is already known. This presentation will discuss ongoing work on this topic at the National Institute of Standards and Technology, with a particular focus on laser powder bed fusion AM machines.

## **Correction of thermo-elastic errors in machine tools – How digital twins help to minimize TCP deviations**

Prof. Dr.-Ing. Steffen Ihlenfeldt

*Fraunhofer Institute for Machine Tools and Forming Technology IWU,  
DE*

### **Abstract**

A central goal of machine tool development is to improve manufacturing productivity and accuracy. Increasing the productivity usually causes larger heat input into machine structures, which deforms them thermo-elastically, and subsequently, reduces machining accuracy. The speech discusses a digital-twin based correction method, which uses a computer model to calculate the thermo-elastic errors at the Tool Center Point (TCP) based on current data from the control system and ambient temperature sensors. Finite element machine models describe the machine structure, the structural variability due to traverse movements of the feed axes, and physical relationships. Model-order-reduction methods enable process-parallel computation of high-resolution models in thermal real-time. The machine models need constant updating; new methods allow identifying larger structural models by condensing parameters to a minimum. Volumetric correction in the control system reverses numerically predicted thermo-elastic errors at TCP in the workspace. Photogrammetric measurement systems verify the correction results. The talk concludes with the implementation of all measures in a conceptual machine tool at Technische Universität Dresden.

## **Enabling technologies for data and knowledge driven software services in manufacturing**

Dr Tom McLeay  
*Sandvik Coromant, SE*

### **Abstract**

At Sandvik Coromant we have a long history of supplying cutting tools and face-to-face application knowledge to customers. In today's world, more and more knowledge is delivered remotely and digitally. Our approach to this is to build intelligent software services that ensure our customers and our tools are the most productive they can be. We believe that this objective can only be achieved by combining advanced sensing, computer intelligence and machine knowledge.

## **Additive manufacturing with electrons**

Ian Laidler

*Wayland Additive, UK*

### **Abstract**

Electron beam additive manufacturing was introduced as a process over 20 years ago, along with its competing technology selective laser melting. Both have advanced and developed in that time. These two technologies offer the user something different. Wayland is a new entrant to the metal additive market, offering a 3rd way, with a new technology “NeuBeam” that has electron beam melting at its core. Wayland have started a fresh and developed the technology from the ground up. This paper looks at electron beam AM / NeuBeam from a machine builder’s perspective as well as the users’ perspective, sharing the fundamental aspects of the technology to the realisation of a manufacturing process. The inherent advantages of the technology are mapped through to end use benefits, such as productivity, controllability, flexibility and quality assurance. Electron beam AM is one of the tools in the additive manufacturing tool set, but one that is less well known. Development of NeuBeam by Wayland Additive will be presented and its implications for the user will be discussed.

## **Next-generation sensors and the disconnect with traditional metrology requirements**

Chris Ivory, Oliver Noakes  
*Hexagon MI, UK*

### **Abstract**

A review of real-world applications across multiple sectors and sub-sectors, where new sensor technologies can offer far greater data and insight, however, have been limited in their application by the old or existing methodologies.

A look at, why these limitations appear, what these limitations are and examples of applications using modern sensor technology to collect impressive, informative, actionable datasets that struggle to conform to out-dated requirements.

## **Dimensional measurement traceability by X-ray computed tomography – where are we?**

Massimiliano Ferrucci

*National Institute of Standards and Technology, US*

### **Abstract**

Long synonymous with medical imaging, X-ray computed tomography (CT) is proving its worth in industrial applications such as material characterization, defect analysis, and dimensional inspection, e.g., of additively manufactured components. Since 2005, when the first purpose-built industrial X-ray CT instrument was made commercially available, there have been significant efforts to understand just how reliable dimensional measurements by X-ray CT are. In metrology, the ultimate measure of confidence is metrological traceability—a clearly-defined but often not well-understood property of a measurement result. Metrological traceability places measurements on a comparable scale and provides a quantitative indication of measurement quality in the form of an uncertainty statement. In this keynote presentation, we provide a high-level discussion about traceability of X-ray CT dimensional measurements to the SI unit of length, review relevant work in empirical determination of X-ray CT measurement uncertainty, and propose a framework for model-based uncertainty assessment and instrument scale calibration as a unified approach to traceability.

## **Invited Presenters**

# **Recent developments in freeform grinding for large EUV lithography optics and head-up display mirrors using a bespoke tool path generation package, MöbiusCAM**

Mark Stocker

*Cranfield Precision, Division of Fives Landis Ltd, UK*

## **Abstract**

Fives, through its R&D centre, Cranfield Precision, Division of Fives Landis Ltd, has recently developed two machines currently being deployed in the manufacture of high precision optics.

A large grinding machine capable of grinding off-axis optics up to 1.6 m (OGM1600) has recently commenced production grinding of large mirrors for extreme ultraviolet (EUV) semiconductor wafer lithography systems. A novel machine concept known as the Twin Turret Grinder (TTG) is being used to develop new manufacturing methods for head-up display mirror molds. Both machines use our custom tool path generation software, MöbiusCAM.

MöbiusCAM uses a step-by-step wizard interface to facilitate the programming of both machines for the grinding and in-situ measurement of complex geometries. The software can also be used to import, analyse and manipulate measurement data from third party, off machine metrology systems. The software is highly flexible and can be made compatible with any machine configuration.

Typical data inputs include, machine axes configuration, including axis limits, tooling available for machining, the surface to be processed and operations to be performed, e.g. freeform spiral, raster, edging etc. Tool paths can be modified to compensate for measured surface errors and rapidly converge on the required form accuracy. For the given required surface geometry and machine, inverse kinematics calculations produce the appropriate machine motions. Conversely, machine axes position data logs (produced during grinding and including logged error motions) can be used to compute the tool position during grinding in order to predict the actual profile ground during machining cycle.

The presentation will include an overview of MöbiusCAM and some recent results from OGM and TTG machines.

## **Standards for machine tools, an update**

Dr Wolfgang Knapp  
*Engineering Office, Switzerland*

### **Abstract**

This is a report on standards activities within ISO/TC 39, machine tools, since the last update presented during Lamdamap 2017. Furthermore, the report contains current standard projects, i.e. standards and technical reports currently under development.

# **Session 1**

## **Machine Tools**

# **Machine tool thermal state representation using modal analysis**

N. Ariaga<sup>1\*</sup>, A.P. Longstaff<sup>1</sup>, S. Fletcher<sup>1</sup>, W. Pan<sup>1</sup>

<sup>1</sup>*Center for Precision Technologies, University of Huddersfield, Huddersfield, UK*

## **Abstract**

Thermally induced deformations degrade the performance of machine tools leading to dimensional errors in manufactured products. Therefore, models are often used to map related observed data such as temperature of key points of the structure to the resultant thermal errors. Predictions from these models are then factored in to the controller commands to offset the errors. However, these data driven models can only learn from the experiences recorded in their training data. Therefore, being able to quantify the state of the machine tool from the data can lead to better modelling results.

This work proposes a novel approach for representing the thermal state of a machine tool. Modal analysis and K-Means clustering are used to extract the descriptor Proper Orthogonal Decomposition (POD) modes in the temperature data which encode the thermal state of the machine tool. These descriptor POD modes identify the different conditions experienced during machining. These features are then used in determining whether any future observed data contains thermal states in the training process. The results obtained show that the approach is able to quantify the differences in the machine's thermal state. These findings will be used to improve thermal error modelling in machine tools.

## **1 Introduction**

Thermally induced errors contribute up to 75% of the overall geometric errors in machine tools[1]. Compensating for these errors using empirical models offers the advantage of being both computationally efficient and applicable after the design and manufacture of the machine tool. Various empirical models have been presented for this use including Neural Network models, Adaptive Neuro-Fuzzy Inference System (ANFIS) models, and linear regression models. In most cases these models are trained off-line and then used online under machining conditions that may differ from those experienced in the training data. This leads to an increase in uncertainties in the model's predictions. Approaches that have been proposed to reduce this uncertainty include online adaptive schemes that tune the model's parameters using process-intermittent probing. Different approaches have been presented for determining when to probe and update the model. This includes using a high sampling rate when training the model and a

lower sampling rate when interrupting the machining process to update the trained model [2]. In [3] an action control limit is placed on the model's predictions which determines when to trigger the probing procedure needed to tune the model. A challenge that may be faced with these approaches is having to retrain a model on data that the model has previously experienced either in the training or update phase. This may lead to unnecessarily high number of probing cycles resulting in reduced throughput in machining. This work proposes the use of modal analysis in identifying machining conditions that have been experienced in the modelling data which can then be used in determining when to gather more data to update the thermal error model. In the instances mentioned above, a compact representation of the thermal state of the machine tool would improve the modelling approaches.

High dimensional data is observed to exist in low-dimensional subspaces in many fields such as image processing, computer vision, pattern recognition and data compression [4]. This can be compared to data in a three dimensional space being closely scattered about a vector or a plane. These low-dimensional subspaces can be extracted through subspace clustering approaches using Principal Component Analysis (PCA) and its variants [5]. PCA is a useful tool in applications such as dimensionality reduction, data visualisation, regression, classification and clustering [6]. An equivalent approach, Proper Orthogonal Decomposition (POD), is used in the analysis of fluid flows, partial differential equations among others from discrete snapshots of data [7], [8]. This approach of snapshots enables the use of POD analysis nonlinear systems even though it is designed for use with linear systems.

This work makes use POD to extract modal data (POD modes) from discrete snapshots of machining data. Sampling and K-Means clustering are then used to extract modal descriptors which encode the thermal state of the machine. These descriptors are then used in determining how similar to the training data is any other data from the machine tool.

## **2 Methodology**

The process of extracting POD modal descriptors of the training data is summarised in *Figure 1*. This process begins with collecting the training data from from the experiment. Snapshots of the input (temperature) data are then obtained by sliding a window of fixed length across the data. A moving average filter is applied to the temperature data to reduce noise in the signal. POD modes are then computed for each snapshot. Random Sample and Consensus (RANSAC) [9] is then used to extract modal descriptors of the training data. To do this, random consecutive modes are then selected and their cluster centroids obtained using K-Means clustering. This sampling and clustering process is repeated for a fixed number of times with the cluster centroids being saved each time. The distance of each POD mode in the training data from each of the saved cluster centroids is calculated. The number of distances whose value is lower than a set threshold is obtained. The cluster centroid with the highest number of distances below the threshold is saved as

one of the modal descriptors of the data. The POD modes whose distance fall below the threshold of that modal descriptor are then removed from the POD modes data under evaluation and the process repeated. This is done until the stop criterion is met. All the saved modal descriptors are then used to identify the training data.

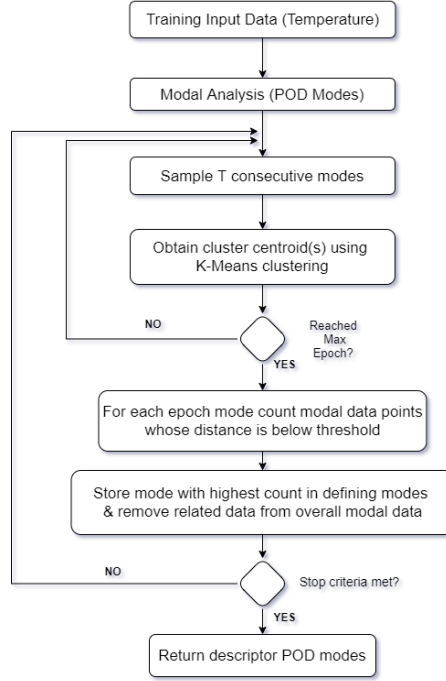


Figure 1: Process of extracting descriptor POD modes from training data

### 2.1.1 Proper Orthogonal Decomposition (POD)

Each snapshot,  $X \in \mathbb{R}^{m \times k}$ , consists of  $k$  discrete samples from  $m$  temperature sensors. The mean of each snapshot is subtracted then Singular Value Decomposition (SVD) is used to extract the Proper Orthogonal Decomposition (POD) modes of the data. This was done using MATLAB R2020a `svd` command.

$$X = U\Sigma V^* \quad (1)$$

The result of SVD are left singular vectors,  $U \in \mathbb{C}^{m \times k}$ , which define the subspaces ( $k$  vectors) in which the snapshot data is spread. These are the POD modes of  $X$ . The singular values,  $\Sigma \in \mathbb{C}^{k \times k}$ , is a diagonal matrix whose values are in decreasing order. Each of the  $k$  singular values captures the scaling of the data along the corresponding left singular vectors. A sharp decrease in the

singular values indicates that most of the data is spread in the leading left singular vectors which forms the basis for subspace clustering and data compression approaches. Finally, the right singular vectors,  $V \in \mathbb{C}^{m \times k}$ , encode the temporal dynamics in the snapshots which is not made use of in POD analysis.

### 2.1.2 K-Means Clustering

$T$  consecutive POD modes are sampled from a random point in the training data. K-Means algorithm is used to group each sampled POD modes,  $\Phi \in \mathbb{R}^{m \times T}$ , into two clusters. Clustering is done using the cosine distance metric which quantifies the angular distance between vectors. The sampling window is made small enough such that it can be assumed to contain modes associated with a heating or cooling cycle or both. Clustering is done by randomly selecting two modes in that act as the cluster centroids,  $\{\varphi_{c_i}\}_{i=1}^2$ . The distance of each mode from the centroids is calculated.

$$d(\varphi_j, \varphi_{c_i}) = 1 - \langle \varphi_j, \varphi_{c_i} \rangle \quad (2)$$

Where  $\langle \varphi_j, \varphi_{c_i} \rangle$  signifies the inner product. These distances are used in determining the cluster that each  $j^{\text{th}}$  POD mode belongs to.

$$c_j = \arg \min_{i=1,2} d(\varphi_j, \varphi_{c_i}) \quad (3)$$

The centroids are then updated by averaging the POD modes in their cluster according to:

$$\varphi_{c_i} = \frac{\sum_{j=1}^T \mathbf{1}_{c_j=i} \varphi_j}{\sum_{j=1}^T \mathbf{1}_{c_j=i}} \quad (4)$$

Where  $j = 1,2$  and  $\mathbf{1}_{c_j=i} = 1$  if  $j^{\text{th}}$  POD mode belongs to the  $i^{\text{th}}$  cluster and zero otherwise. Steps represented by equations (2) to (4) are repeated to convergence. The distance between the cluster centroids is then evaluated. If this distance is above a set threshold then the sampled POD modes are assumed to have contained POD modes from two distinct heating or cooling cycles. Conversely, if this distance is below the threshold then the sampled POD modes are assumed to have been from the same unique heating or cooling cycle and a single centroid is obtained and returned by another K-Means clustering process.

### 2.1.3 Random Sample Consensus (RANSAC)

Sampling and K-Means clustering is performed for a set number of times,  $P$ , which returns a maximum of  $P$  centroids. RANSAC algorithm is used in determining which centroids returned from the sampling and clustering run are

most significant in defining the data. First, the cosine distance between each centroid and the sum of the number of POD modes whose distance lies below set threshold obtained.

$$s_p = \sum_{j=1}^K (d(\varphi_j, \varphi_{c_p}) \leq Threshold) \quad (5)$$

Where  $\varphi_j$  is  $j^{th}$  POD mode of all the  $K$  POD modes in the training data and  $\varphi_{c_p}$  is the  $p^{th}$  centroid. The most significant centroid that defines the data is chosen as the one that maximizes the number of POD modes that lie below the set threshold:

$$\varphi_d = \arg \max_{p=1, \dots, P} s_p \quad (6)$$

## 2.2 Experiment setup

To test the performance of the proposed approach, experiments were carried out on a small vertical machining centre (VMC). The machine was subjected to two cycles, a random duty cycle heating of the spindle and another random duty cycle heating of the spindle and Z axis. The thermal state of the machine was captured using twenty seven temperature sensors placed in strips at the carrier, spindle boss, axes motors and axes ballscrew nuts. The setup is summarised in *Figure 2*. A sampling rate of 0.1 Hz was used.

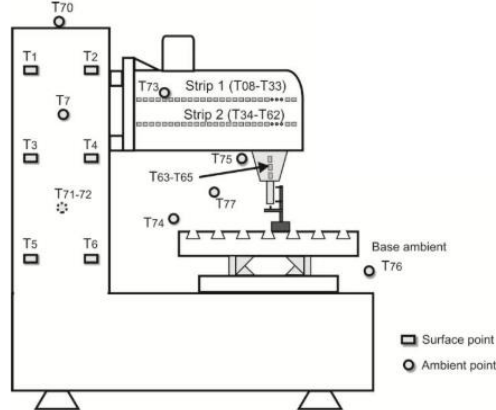


Figure 2: Experiment setup showing location of temperature sensors

## 3 Results and Discussion

The temperature data collected from the twenty-seven temperature sensors in the training phase is summarised in the first plot of *Figure 3*. This data was collected under random duty cycle heating of the spindle conditions. POD

modes were then calculated at each time step from the recent 120 samples (window size) of data resulting in a 27-dimensional vector. These vectors were plotted as a surface plot in the second plot of *Figure 3*. This plot consists of coherent patterns which can be used in identifying the thermal state of the machine. The extracted POD modes show a strong alignment along the 16<sup>th</sup> dimension. This signifies a relatively high dispersion in the 16<sup>th</sup> temperature sensor of the data which was attached to the spindle motor bolt. Though there seems to be a direct mapping from temperature sensor to the dimension of alignment of the POD mode, this is not always the case. For example, after the 300<sup>th</sup> minute, the rate of decrease in temperature readings reduces to a rate matching other temperature sensors. This results in a shift in the POD mode alignment. Thus, the POD modes can encode the dispersions in the data observed over a period to a vector representation.

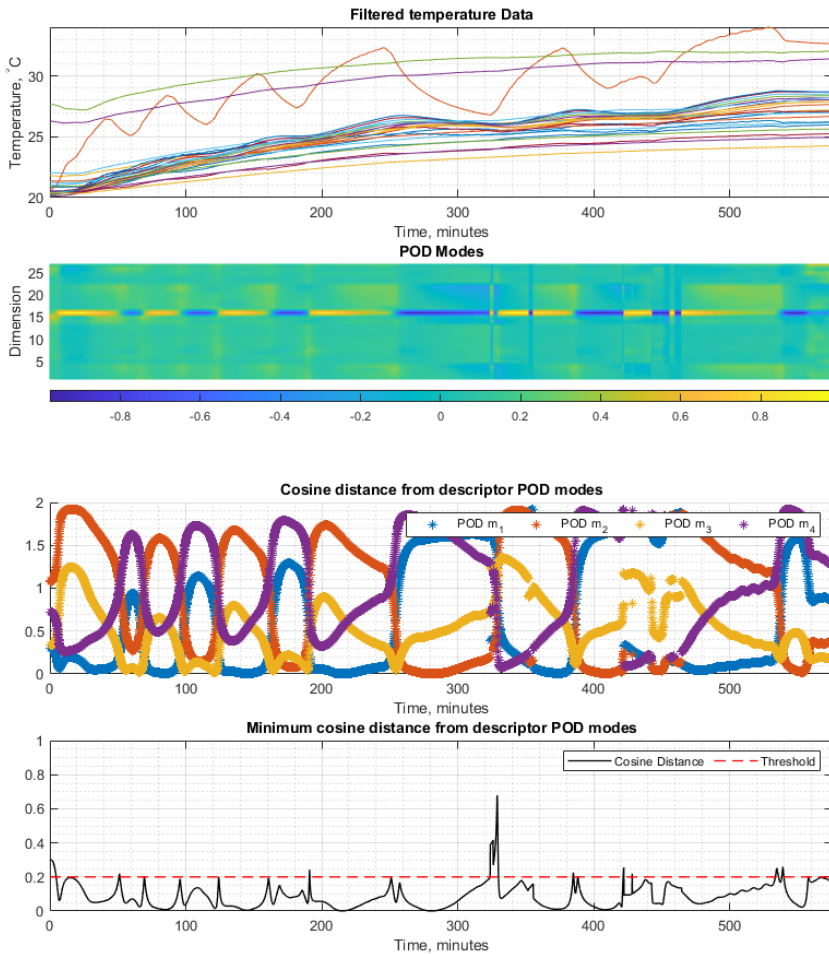


Figure 3: Analysis of temperature data in training dataset

Descriptor POD modes were extracted from the POD modes of the training data using the methodology present in section 2. This resulted in four descriptor POD modes as shown in *Figure 4*. A centroid returned by the K-Means clustering algorithm was considered a descriptor POD mode it had a cosine distance lower than 0.2 from more than 200 samples of POD modes. The cosine distances from these descriptor POD modes to all other POD modes of the training data are shown in the third plot of *Figure 3*. The minimum cosine distance from the descriptor POD modes to the training data POD modes is shown in the fourth plot of *Figure 3*.

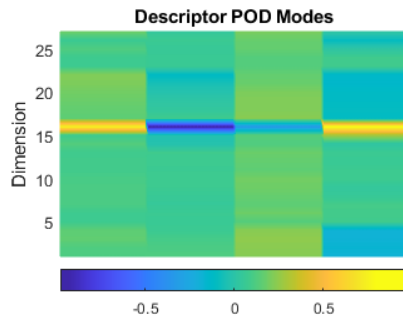


Figure 4: POD mode descriptors extracted from the training dataset

The temperature data and related POD modes of the first test dataset, dataset A, are shown in the first and second plots of *Figure 5* respectively. Dataset A was collected under random duty cycle heating of the spindle and the Z axis conditions. Coherent patterns in the POD modes show that the data is spread within a low dimensional space as did the training data POD modes. The cosine distance from the descriptor POD modes of the training data to POD modes of this test dataset is shown in the third plot of *Figure 5*. The minimum value of the calculated distances is shown in the fourth plot of *Figure 5*. The distances obtained have values significantly higher than the evaluation threshold value of 0.2. Thus, the approach is able to give a measure of difference between thermal states observed in the data. This disparity results from the fact that cycles run on the machine tool resulting in test dataset B were different to those run in to obtain the training dataset.

The second test dataset, dataset B, was collected under machining cycles similar to those of the training dataset. The resultant temperature data and related POD modes are shown in the first and second plots of *Figure 6* respectively. The observed coherent patterns in the POD modes resemble those obtained from the training data. Evaluating the POD modes of this dataset using the descriptor POD of the training dataset results in the third and fourth plots of *Figure 6*. The minimum cosine distance values obtained indicate a close resemblance of the machine tool's thermal state to that experienced under the

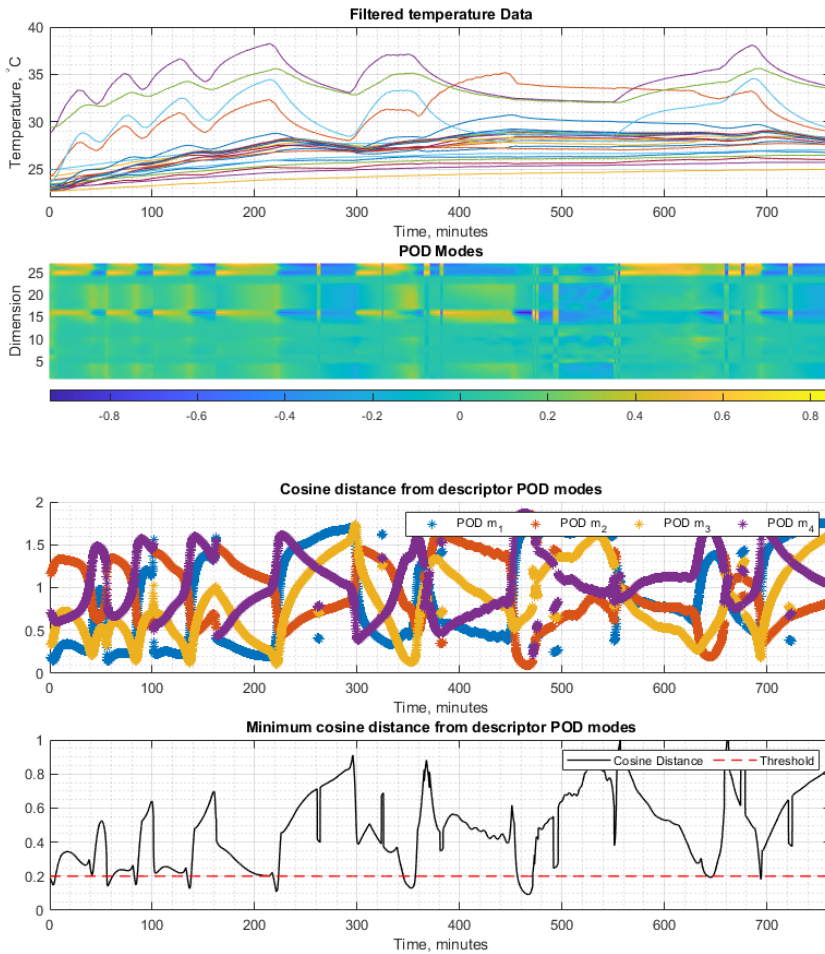


Figure 5: Analysis of temperature data in test dataset A

training data machine cycles. With the exception of values about the 300<sup>th</sup>, 410<sup>th</sup> and 550<sup>th</sup> minutes, most of the cosine values fall below the threshold value. The pattern observed in the POD modes at those time stamps are similar and also match the pattern observed in the POD modes of the training data about the 320<sup>th</sup> minute of the second plot in *Figure 3*. Thus, these exceptions in performance may be resolved by further tuning of the algorithm that extracts the descriptor POD modes.

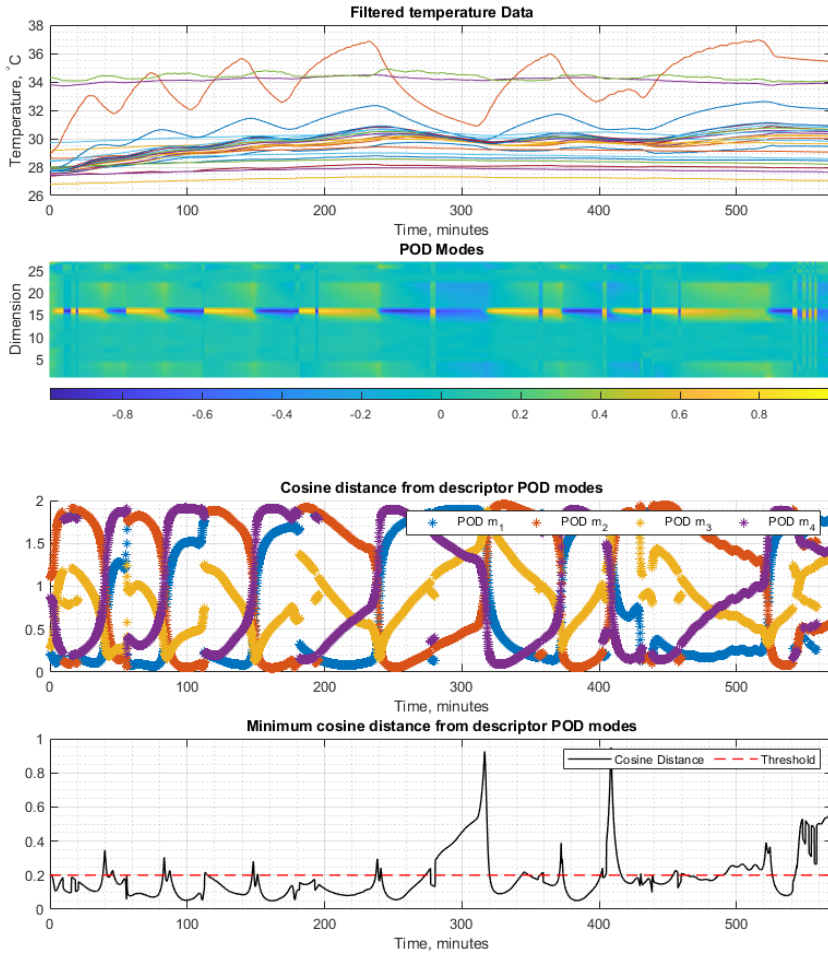


Figure 6: Analysis of temperature data in test dataset B

## 4 Conclusion

A novel approach for quantifying the thermal state of a machine tool from temperature data has been presented in this paper. Descriptor POD modes that encode the dispersion of temperature readings within snapshots of the data were obtained from a training dataset of machining data. The results indicate that the approach does quantify how similar a test dataset is to the training dataset. Similar thermal states have distance values below the evaluation threshold. The number of sensors to use and their placement should adequately detect the thermal gradients that significantly affect the thermal error of the machine tool. The approach can then be used to inform the experiments to be carried out rather

than carrying out a lot of tests that induce heat in a way that would not be seen during normal operation.

The uncertainty of decisions using the first POD mode is captured in the singular values. These values measure the variability of the data represented in each of the POD modes. Further study is being carried out to determine the uncertainty introduced by other factors such as window size selection, resolution of the sensors used, signal to noise ratio and hysteresis.

## **Acknowledgement**

The authors gratefully acknowledge the UK's Engineering and Physical Sciences Research Council (EPSRC) funding of the Future Metrology Hub (Grant Ref: EP/P006930/1).

## **References**

- [1] J. Mayr *et al.*, "Thermal issues in machine tools," *CIRP Ann. - Manuf. Technol.*, vol. 61, no. 2, pp. 771–791, 2012, doi: 10.1016/j.cirp.2012.05.008.
- [2] H. Yang and J. Ni, "Adaptive model estimation of machine-tool thermal errors based on recursive dynamic modeling strategy," *Int. J. Mach. Tools Manuf.*, vol. 45, no. 1, pp. 1–11, 2005, doi: 10.1016/j.ijmachtools.2004.06.023.
- [3] J. Mayr, P. Blaser, A. Ryser, and P. Hernandez-Becerro, "An adaptive self-learning compensation approach for thermal errors on 5-axis machine tools handling an arbitrary set of sample rates," *CIRP Ann.*, vol. 67, no. 1, pp. 551–554, 2018, doi: 10.1016/j.cirp.2018.04.001.
- [4] E. Elhamifar and R. Vidal, "Sparse subspace clustering: Algorithm, theory, and applications," *IEEE Trans. Pattern Anal. Mach. Intell.*, vol. 35, no. 11, pp. 2765–2781, 2013, doi: 10.1109/TPAMI.2013.57.
- [5] F. W. Townes, "Generalized Principal Component Analysis," *arXiv*, vol. 27, no. 12, pp. 1945–1959, 2019, doi: 10.1007/978-981-10-2915-8\_7.
- [6] I. T. Jolliffe and J. Cadima, "Principal component analysis: A review and recent developments," *Philos. Trans. R. Soc. A Math. Phys. Eng. Sci.*, vol. 374, no. 2065, 2016, doi: 10.1098/rsta.2015.0202.
- [7] K. Lu *et al.*, "Review for order reduction based on proper orthogonal decomposition and outlooks of applications in mechanical systems," *Mech. Syst. Signal Process.*, vol. 123, pp. 264–297, 2019, doi: 10.1016/j.ymsp.2019.01.018.
- [8] S. Sahyoun and S. Djouadi, "Local Proper Orthogonal Decomposition based on space vectors clustering," *2013 3rd Int. Conf. Syst. Control. ICSC 2013*, pp. 665–670, 2013, doi: 10.1109/ICoSC.2013.6750930.
- [9] M. A. Fischler and R. C. Bolles, "Random sample consensus," *Commun. ACM*, vol. 24, no. 6, pp. 381–395, Jun. 1981, doi: 10.1145/358669.358692.

# Comparison of measured static and quasi-static deflections of industrial manipulators

Nikolas Alexander Theissen, Monica Katherine Gonzalez, Theodoros Laspas, and Andreas Archenti  
*KTH Royal Institute of Technology, Sweden*

## Abstract

This work presents a comparison of the measured static and quasi-static deflections of industrial manipulators. For the measurement of the static deflections, the manipulator remains in static positions while for the quasi-static deflections the manipulator follows a circular trajectory. The static deflections are measured at discretised static configurations along circular trajectories while the quasi-static deflections are measured under circular motion along the same trajectories. Loads of different magnitudes were induced with the Loaded Double Ball Bar (LDBB). The static and quasi-static displacements are measured using a (Linear Variable Differential Transformer) LVDT embedded in the Loaded Double Ball Bar and a Leica AT901 laser tracker. These measurement procedures are implemented in a case study on a large-sized serial articulated industrial manipulator from ABB in three different positions of its workspace. The presented method shows that the measured quasi-static deflections are on average approximately 22% bigger than the measured static deflections. The quasi-static deflections are at most 32% bigger than the static deflections. Finally, the manuscript concludes with a discussion on how the measurement procedure could be used to analyse the difference between using the static stiffness and the apparent quasi-static stiffness of an industrial manipulator for trajectory optimisation.

## 1. Introduction

The demand for industrial robots has been increasing and can be considered significant, as shown by the market volume of approximately 16.2 billion USD achieved by these products in 2017 [1]. Industrial robots are capable of realizing numerous tasks while at the same time providing modern manufacturing environments with the flexibility to adapt to smaller lot sizes. Additionally, they are cheaper based on price per unit of working space when compared with specialized machinery, e.g., milling machines, lathes, or machining centres.

These capabilities have led to the integration of industrial robots across important industries for a wide variety of commodities such as consumer electronics, industrial machinery, or vehicles and in a variety of applications ever since 1961. For industrial manipulators in conventional metal cutting, stiffness is an informative performance criterion. It is even more important than in machine tools as machine tool tend to be significantly stiffer, i.e. optimising the process parameters more easily yield products of the required Geometric Dimensions and Tolerances (GD&T). The stiffness of a mechanical system can be defined as its capacity to sustain loads, which result in a change of its geometry [4]. One differentiates between static, quasi-static, and dynamic stiffness. This work investigates the difference between static stiffness, i.e. static manipulator, and quasi-static stiffness, i.e. moving manipulator. It is possible that to measure the static and quasi-static stiffness of an industrial manipulator most accurately one should not move the system. From a theory point of view, one can exert static loads, i.e. the frequency is equal to 0 Hz, and the quasi-static loads, i.e. the frequency is greater than 0 Hz and lower than 0.5 Hz, for the identification without moving the industrial manipulator [2]. However, this work follows the idea outlined by Archenti and Nicolescu [3] that to accurately identify a system's capability for an intended task, one should emulate the intended task. Case studies on machine tools, see Laspas et al. [4] and Theissen et al. [5], have implied that there can be differences in the magnitude of the static and quasi-static stiffness. This work quantifies this difference for a single large-sized serial articulated manipulator.

## **2. Methodology**

This section describes the measurement devices, measurement procedures, and data processing for the measurement and identification of the static and quasi-static deflections. The static and quasi-static procedures use the same measurement devices but differ in the measurement procedure and the data analysis. The quasi-static procedure builds on the static procedure.

### **2.1. Measurement devices**

The conceptual measurement setup can be seen in Figure 1. The setup comprises the following equipment: 1) a large-sized serial articulated industrial robot with its corresponding controller (not included in the picture), 2) a Leica AT901-LR laser tracker (not included in the picture) [6] with a 0.5 '' Red Ring Reflector (RRR), 3) the measurement instrument Loaded Double Ball Bar (LDBB) [7] with a DTA-3G8-3-CA LVDT [8], 4) a rigid Table Link (TL), and 5) a dummy end-effector with Tool Centre Point (TCP) and a mechanical interface for the Spherically Mounted Retro-reflector (SMR). The deflection measurements are performed with two different metrology loops. The first metrology loop uses an LVDT for the deflection measurement, the second loop uses the laser tracker.

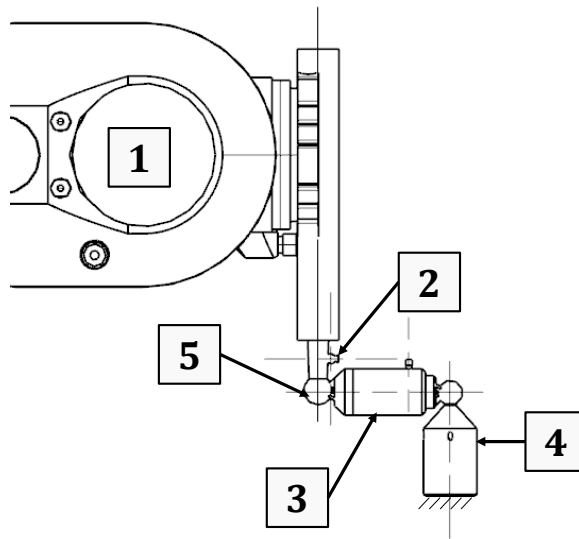


Figure 1: Measurement setup

## 2.2. Measurement process

The static measurement induces loads of 125 N, 250 N, 375 N, and 500 N at 37 indexed positions along a circular trajectory, see Figure 2. Target 1 and 37 are at the same position, i.e. the static circle has the same start and endpoint. Once the manipulator reaches a stable position the static loads are induced at the TCP. Once the LDBB reaches a stable load level, i.e. within a limit of  $\pm 0.7\%$  at 125 N down to  $\pm 0.2\%$  at 500 N, the measurements are acquired with both the laser tracker, using the *Precise* measurement profile, and the LVDT, using continuous data recording at 1000 Hz. The quasi-static measurement procedure induces loads of 125 N, 250 N, 375 N, and 500 N along the circular trajectory with a diameter of approximately 250 mm. In this case, the manipulator executes a trigger movement by moving 1 mm up and down at the start point of the circle, with a velocity of 250 mm/sec. Then the manipulator moves two times clockwise about the same circular trajectory, see Figure 2. The circles were measured with an Angular Overshoot (AOS) of  $180^\circ$  to exclude transient effects from the measurement data [20]. The manipulator followed the trajectory with a Cartesian velocity of 50 mm/sec. At this velocity, dynamic effects can be assumed negligible. Both the laser tracker and the LVDT are set to continuous data recording at 1000 Hz, this dissected the circle into approximately 16,000 measurement points. For both the static and the quasi-static measurement multiple force components were exerted simultaneously. This approach differs from the description of circular testing according to ISO 230-4 [9]. Thus, the Z-axis component's magnitude was chosen to be roughly 1/3 of the total load, while the remaining 2/3 were split between the X- and Y-axis components, whose contribution depended on the position of the LDBB along the circle.

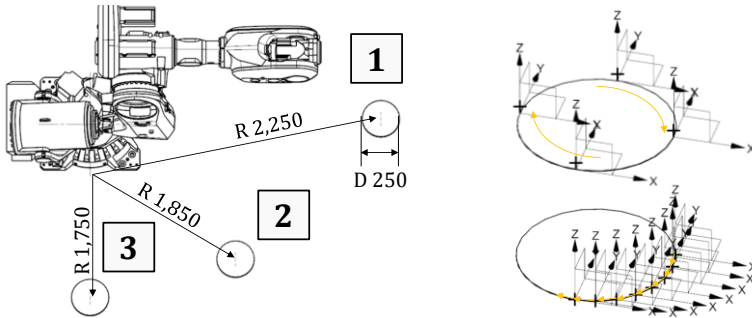


Figure 2: Positions of circles 1.-3. in the robot's base coordinate system (left) and the targets along the circle for the static (right down) and quasi-static measurement (right up). The targets along the circle for the static measurement are exemplified for the first quadrant.

The procedure for both the static and quasi-static measurement is repeated at three positions numbered as Circle 1 to Circle 3 and have different distance  $R$  from Robot's Base Coordinate System (RBCS) origin (see Figure 2) maintaining the same  $Z$  height from the RBCS origin.

### 2.3. Data analysis

The deflections  $\Delta X$  are calculated as the position difference of the loaded TCP position  $X_{i,j}$ , i.e. for the positions  $i$  and the loads  $j = [250\text{ N}, 375\text{ N}, 500\text{ N}]$ , and the reference TCP position  $X_{i,ref}$  at a load of 125 N according to:

$$\Delta X_{i,j} = \begin{bmatrix} \delta x \\ \delta y \\ \delta z \end{bmatrix}_{i,j} = \begin{bmatrix} x \\ y \\ z \end{bmatrix}_{i,j} - \begin{bmatrix} x \\ y \\ z \end{bmatrix}_{i,ref} \quad (1)$$

The magnitude of the deflection  $\|\Delta X_{i,j}\|_2$ , which is referenced in the subsequent section, is calculated as the Euclidean norm of the deflection:

$$\|\Delta X_{i,j}\|_2 = \sqrt{\delta x^2 + \delta y^2 + \delta z^2} \quad (2)$$

Thus, the magnitude of the deflection corresponds to the distance between the loaded and unloaded position. For the static deflections at the  $i = [1, \dots, 37]$  TCP positions this calculation is straight forward for the measurement data from both, the laser tracker and the LVDT. For the quasi-static deflections at the  $i = [1, \dots, 15899]$  TCP positions, first, the AOS needs to be removed then the difference can be calculated. In both, the static and quasi-static case, the measurement from the LVDT needs to be compensated for the deflection of the table link. All deflections are calculated relative to a reference load of 125 N, this removes the influence of the hysteresis in the setup. In the following section, the wording *acting load* is used to highlight this idea. An acting load of 125 N means that the system is loaded with 250 N, but the difference with respect to 125 N is considered.

### 3. Results

The magnitude of the static and quasi-static deflections along Circle 1 for acting loads of 125 N, 250 N, and 375 N can be seen in Figure 3 and Figure 4. Circle 1 is positioned about 2.250 m from origin. The magnitude of the deflection, as one would expect, increases with the load but also changes along the circular trajectory as the Cartesian stiffness of the industrial manipulator depends on the configuration [10]. The data have been measured using the LVDT as well as a laser tracker. The average differences the static and quasi-static deflection between the LVDT and the laser tracker equal around 40  $\mu\text{m}$ . Figure 3 and Figure 4 support the observation that both measurement instruments yield results close to a couple of tenth of micrometres. This differences can be accounted for by the uncertainty of the laser tracker, around 10  $\mu\text{m}$ , as well as the different measurement position, the distance between both measurement points equals approximately 6 mm. The remaining difference of about 30  $\mu\text{m}$  could be explained by an angular error of around 0.3 degrees. This observation is supported by the magnitude of the measured static and quasi-static deflections for Circle 1, to Circle 3, in Table 1 to Table 3. Furthermore, the tables show that the magnitude of the deflections increases with the distance from joint 1, i.e. the origin of the RBCS.

For all acting loads and all circles in the case study, the quasi-static deflections are bigger than the static deflections. The static and quasi-static deflections are very similar in their characteristics but differ in their magnitudes. The measured quasi-static deflections are on average approximately 22% bigger than the measured static deflections. The quasi-static deflections are at most 32% bigger than the static deflections.

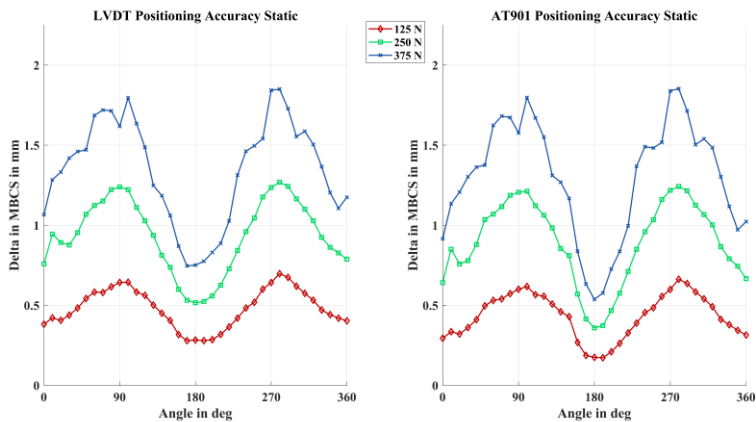


Figure 3: Magnitude of the static difference, i.e. Euclidean norm of the Cartesian deflections, as measured by the LVDT (left) and AT901 laser tracker (right).

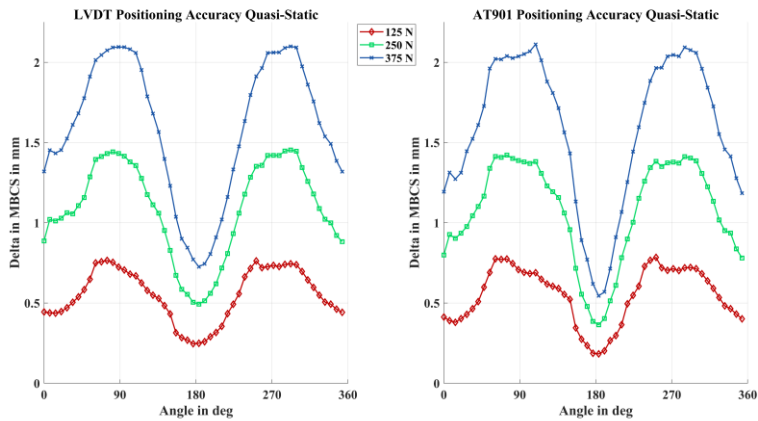


Figure 4: Magnitude of the quasi-static difference, i.e. Euclidean norm of the Cartesian deflections, as measured by the LVDT (left) and AT901 laser tracker (right).

#### 4. Discussions

The results displayed in Table 1 to Table 3 imply that there can be significant differences in the magnitude of the static and quasi-static deflections. It needs to be pointed out that there is no apparent determinism that leads to the observed difference, i.e. from the observations of this case study one cannot derive useful information about other serial articulated manipulators. One cannot even derive further information about the remaining workspace for the investigated industrial manipulator. Further investigations require the analysis of the influence of Cartesian velocities, i.e. friction, as well as different controller settings in terms of operation mode and task program on the difference between static and quasi-static deflections. Nevertheless, the case study shows that the LDBB is capable of accurately identifying the deflections of industrial manipulators along circular trajectories. This may facilitate a pragmatic compliance calibration of industrial manipulators. The pragmatism in that sense lies in the possibility to calibrate an industrial manipulator task-dependent, i.e. in the relevant portion of the workspace with loads in the magnitude of the task. This may make compliance calibration cheaper, faster, and potentially more accurate.

#### 5. Acknowledgement

The authors would like to thank VINNOVA and the SMART advanced manufacturing cluster for funding this research as a part of the COMACH project (Grant Agreement ID: S0120). The authors would like to also express their gratitude to the Centre for Design and Management of Manufacturing Systems (DMMS) for their financial support.

## Laser Metrology and Machine Performance XIV

Table 1: Magnitude of the measured static and quasi-static deflections along circle 1.  
Average of the norm of Cartesian deflections Circle 1 (Distance 2.250 m).

Acting Load in N	Static (S)		Quasi-Static (QS)		QS/S
	LVDT in mm	AT901 in mm	LVDT in mm	AT901 in mm	
125	0.48	0.43	0.55	0.55	+20 %
250	0.94	0.89	1.10	1.10	+18 %
375	1.35	1.30	1.62	1.62	+20 %

Table 2: Magnitude of the measured static and quasi-static deflections along circle 2.  
Average of the norm of Cartesian deflections Circle 2 (Distance 1.850 m).

Acting Load in N	Static (S)		Quasi-Static (QS)		QS/S
	LVDT in mm	AT901 in mm	LVDT in mm	AT901 in mm	
125	0.22	0.24	0.25	0.32	+25 %
250	0.45	0.44	0.55	0.62	+32 %
375	0.69	0.62	0.74	0.90	+25 %

Table 3: Magnitude of the measured static and quasi-static deflections along circle 3.  
Average of the norm of Cartesian deflections Circle 3 (Distance 1.750 m)

Acting Load in N	Static (S)		Quasi-Static (QS)		QS/S
	LVDT in mm	AT901 in mm	LVDT in mm	AT901 in mm	
125	0.14	0.15	0.17	0.20	+28 %
250	0.30	0.30	0.32	0.38	+17 %
375	0.45	0.44	0.47	0.56	+16 %

## References

- [1] INTERNATIONAL FEDERATION OF ROBOTICS. *Executive Summary World Robotics 2018 Service Robots*, 2018.
- [2] Rivin E I. *Handbook on stiffness & damping in mechanical design*. New York: ASME Press, 2010. ISBN 0791802930.
- [3] Archenti A and Nicolescu M. Accuracy analysis of machine tools using Elastically Linked Systems [online]. *CIRP Annals - Manufacturing Technology*, 2013, 62(1), 503-506. ISSN 00078506. Available under: doi:10.1016/j.cirp.2013.03.100
- [4] Laspas T, Theissen N and Archenti A. Novel methodology for the measurement and identification for quasi-static stiffness of five-axis machine tools [online]. *Precision Engineering*, 2020, 65, 164-170. ISSN 01416359. Available under: doi:10.1016/j.precisioneng.2020.06.006
- [5] Theissen N, Laspas T, Szipka K and Archenti A. *Measurement and identification of translational stiffness matrix for static loads in machine tools*. In: *Virtual International Conference 2020*, 2020.
- [6] LEICA GEOSYSTEMS. *User Manual AbsoluteTracker AT901*.
- [7] Archenti, A., Hg. *A Computational Framework for Control of Machining System Capability. From Formulation to Implementation*. Stockholm, 2011. ISBN 978-91-7501-162-2.
- [8] MIRCO-EPSILON USA. *Linear inductive displacement sensors*.
- [9] International Organization for Standardization, *ISO 230-4:2005 Test code for machine tools – Part 4: Circular tests for numerically controlled machine tools*.
- [10] Klimchik A, Furet B, Caro S and Pashkevich A. Identification of the manipulator stiffness model parameters in industrial environment [online]. *Mechanism and Machine Theory*, 2015, 90, 1-22. ISSN 0094114X. Available under: doi:10.1016/j.mechmachtheory.2015.03.002

# **Quantitative assessment of machine tools precision states through fractal analysis of machine error parameters**

Kanglin Xing<sup>1,\*</sup>, Xavier Rimpault<sup>1,2</sup>, J.R.R. Mayer<sup>1</sup>, Jean-François Chatelain<sup>2</sup>, Sofiane Achiche<sup>1</sup>

<sup>1</sup>Department of Mechanical Engineering, Polytechnique Montréal, Montréal, QC H3T 1J4, Canada

<sup>2</sup>Department of Mechanical Engineering, École de technologie supérieure, Montréal, QC H3C 1K3, Canada

## **Abstract**

The precision status of machine tools directly affects parts' quality. Therefore, periodical calibration of machine tools is desirable. Multiple machine error parameters can be acquired in one calibration using automated indirect methods, but to fully automate the calibration, the automation of the results is required. Fractals have been successfully used to process volumetric error vector similarity measures and volumetric error coordinates of machine tools. Herein, fractals are firstly attempted to process the machine error parameters for quantitative assessment of the machine tool precision state. The SAMBA method is used to measure the 13 machine error parameters of the experimental HU-40T five-axis machine tool. Repeated tests are conducted with the machine tool in its normal state, real C-axis encoder and pseudo pitch/straightness error faulty states. In addition, simulated faults with steep and gradual change caused by the manual correction of ISO230-1 error parameters are also considered. As a comparison, the change of machine tool precision state is also recognized by fractal analysis of volumetric error coordinates. Towards the same fault, the proposed method has been found to be an efficient approach to detect faulty states. The fractal analysis application in this study has a comparable performance as fractal analysis of volumetric error coordinates in machine tool precision state recognition. Therefore, fractal analysis of machine error parameters could be an effective tool to detect change in a machine tool status.

## **1 Introduction**

The precision state of machine tools plays a decisive part in modern manufacturing. A stable precision state of machine tool is helpful to ensure the machining quality. However, in practice, factors such as the change of geometric errors, thermal errors, tool wear, etc can all contribute to the machining inaccuracy [1]. Therefore, it is of great importance to identify the precision state of machine tools.

The precision state of machine tools can be accordingly confirmed either by a single machine error or by a qualitative analysis of machine tool errors. A single machine error could be measured using direct methods such as the laser interferometer, laser tracker, or indirect methods such as the scale and master ball artefact (SAMBA) method [2]. Qualitative analysis of machine tool errors has been found in volumetric errors (VEs). For example, VEs have been processed by vector similarity measures and control chart for the identification of machine tools conditions fluctuation. In addition, VEs processed by K-means and principal component analysis can be used for machine tool precision states classification [3, 4]. Moreover, a novel method based on fractal analysis has been used to process VEs coordinates, and provides new measures for VEs feature extraction [5]. The advantage of this method is that the acquired VE vector coordinates are directly processed without any further data pre-processing. Technically, using this fractal analysis approach decreases the complexity in VEs data processing. In addition, similar attempts of fractal analysis could also be found in VEs VSMs. As an alternative method, could the measured/estimated machine error parameters be applied to quantitatively assess the precision state of a machine tool?

Fractal analysis is a technique allowing to quantify the shape pattern(s) of an object at different magnification scales. The complexity of shape pattern(s) can be reflected by the fractal parameters that have a the shape pattern can be reflected by the fractal parameters which have good correlation relationship with the change process of one monitoring object [6], for example, a machine tool evolving state, a machining process and the tool life [7, 8]. Based on the best performance in the above domain and the processing of VEs, therefore, fractal analysis is selected as the main method for processing the machine error parameters.

Therein, the research evaluates the performance of machine tools precision state indicator generated by fractal analysis of machine error parameters. To verify the performance of the proposed method, one published solution based on fractal analysis of VE coordinates has also been included. Validations of the proposed method are conducted using data of a real fault acquired from the experimental machine tool (C axis encoder fault), pseudo-faults (EXX, EYX and EZX) and the simulated faults caused by the gradual and steep change of the modelled "13" machine error parameters. Finally, the conclusions are drawn.

## **2 Machine tools precision state indicator data processing**

Machine tool error parameters are usually acquired at variable times during machine tools maintenance pitstops. Then, these error parameters are be coupled

as the input for fractal analysis. The generated fractal results are assessed in view of the precision state of machine tools.

### 2.1 Machine error parameters and their acquisition

An indirect machine tool calibration method, the SAMBA method is selected to estimate machine error parameters and volumetric errors of a five-axis machine tool. Usually, different machine error parameters could be estimated by the selection of machine error models. The detail of the SAMBA machine error model could be found in [9, 10]. Herein, a "13" machine error model (Figure 1) is selected owing to its advantages in measurement time and model stability. The meaning of each error parameter could be found in Figure 1.

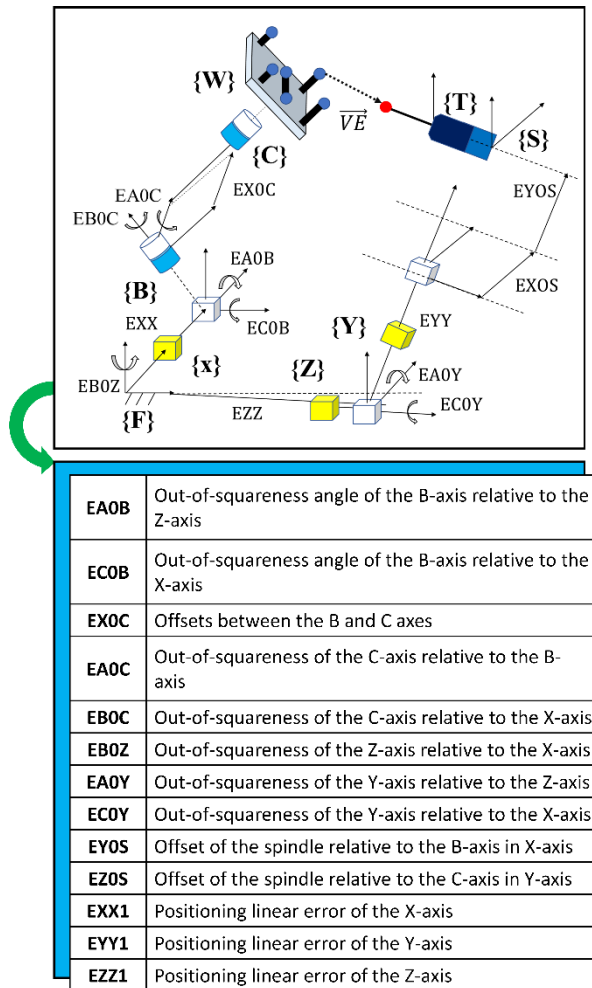


Figure 1. Kinematic chain of HU-40T five-axis machine tool and the meaning of the "13" machine error parameters [9]

After the SAMBA measurement, 13 machine error parameters are combined as a data series (Eq. (1)) for the next fractal analysis.

$$ME_j = [EA0B, EC0B, EX0C, \dots, EYY1, EZZ1] \quad (1)$$

## 2.2 Data processing using fractal analysis

Fractal analysis allows evaluating the fractal characteristics of a dataset, and it includes methods such as correlation and capacity dimensions [11]. Among numerous fractal analyses, the fractal regularization technique is chosen for this research thanks to its relatively good robustness and high degree of automation [11]. It relies on the convolution of a data series "s" with different rectangle sized kernels  $g_a$  – affine function with a width of "a" (Eq. (2)) [6]. Then,  $s_a$  is presumed to have a finite length (la). Finally, a fractal dimension estimation, expressed as the regularization dimension D, is calculated as Eq. (3).

$$s_a = s * g_a \quad (2)$$

$$D = 1 - \lim_{a \rightarrow 0} \frac{\log l_a}{\log a} \quad (3)$$

According to the referenced procedures for the preliminary evaluation [5], the range of the slope determination is obtained. After that, the following three fractal measures can be acquired: the fractal dimension D (slope estimation), the topothesy G (y-intercept) and R2 (auto-scale regularity) [6]. Besides, an index measure considering the above three measures is also used (Eq. (4)) [12]:

$$\text{Index} = \frac{D \cdot G}{R^2} \quad (4)$$

In this research, except the fractal analysis of machine error parameters, fractal assessment of VEs coordinates (Eq. (5)) is also conducted. By comparing of both results, the performance of the fractal analysis of machine error parameters could be investigated. The VE coordinates of one SAMBA measurement are combined as a data series for fractal processing (Eq. (5)). For the detail, please refer to [5].

$$VExyz_i = [VEx_{i,1}, VEy_{i,1}, VEz_{i,1}, \dots, VEx_{i,N}, VEy_{i,N}, VEz_{i,N}] \quad (5)$$

## 3 Machine tools precision state indicator data processing

Machine error parameters for this research comes from the following four sources (Figure 2): A real fault in the continuous measurement of a HU40-T five-axis machine tool; Pseudo-faults generated by the modification of machine error compensation tables; Simulated steep or gradual change fault caused by the correction of one error parameter; A specific simulated fault caused by the manual

correction of EZX error parameter. Regarding the real fault, it is caused by a faulty in the C axis encoder. After detecting this fault, the C axis angular position was control by the C axis motor encoder, which may bring a slight change to positioning capability.

To increase the diversity of the fault types, two pseudo-faults EXX and EYX were applied. For the EXX fault, a U shape error with magnitudes of 35 μm was inputted to the pitch error compensation table for the X axis to decrease the positioning capability of the X- axis. This operation could be reflected in the estimated machine error parameters. The second pseudo-fault EYX was generated by the manual modification of the raw SAMBA probing file. The Y-axis coordinate of each probing position is corrected as a function of its X-axis coordinate [6].

The simulated faults caused by the gradual or steep change of one of the "13" machine error parameters were generated by the AxiSAMBA™ simulator software. The change tendency of one modelled error parameter was set accordingly as the paper [4], while the change of remaining error parameters is in a range of 15% of its normal reading. The same simulation rule has also been applied in the fault simulation of an un-modelled EZX error.

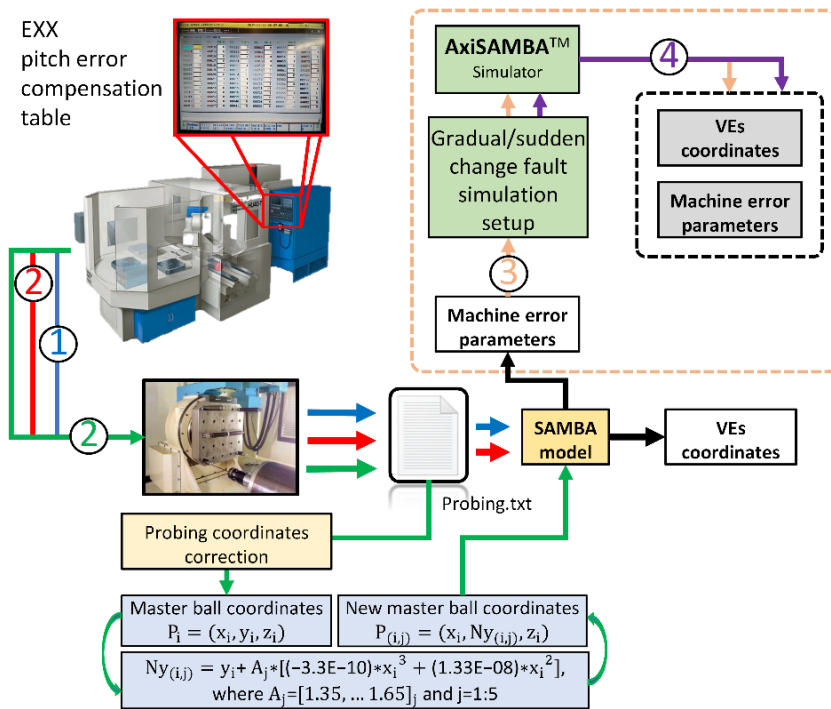


**Figure 2.** faults generated from four paths. Path (1) stands for the real C-axis encoder fault; Path (2) pseudo EXX and EYX faults; Path (3) simulated gradual/steep change fault; Path (4) simulated EZX fault.

## 4 Results and discussion

The fractal measures of machine error parameters and VE coordinates of each SAMBA measurement were calculated, respectively. After that, the detected fault occurrence time using the fractal analysis of two inputs were compared with the known occurrence time.

### 4.1 Real C-axis encoder fault analysis

Four presented fractal measures were used to process the data series of machine error parameters and VE coordinates (Figure 3). The known fault occurrence time is the 13th and it could be well recognized by fractal assessment of VE coordinates and machine error parameters (except the fractal parameter R2). However, a slightly different normal machine condition could only be suggested by the fractal parameters of VE coordinates rather than the machine error's fractal parameters.

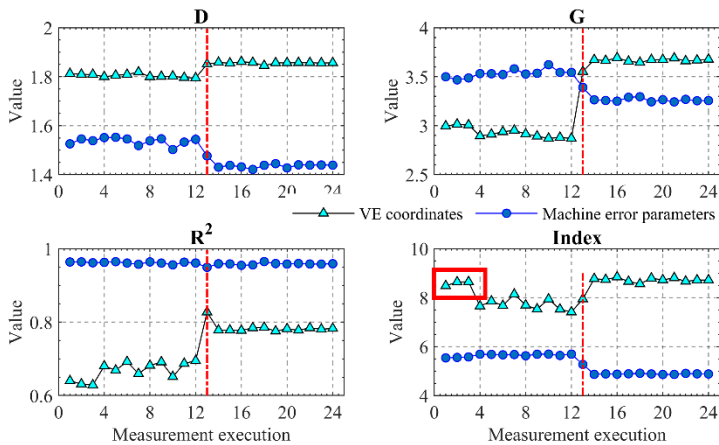


**Figure 3.** Fractal analysis of machine error parameters acquired before and after the occurrence of C axis encoder fault

### 4.2 Pseudo faults EXX and EYX analysis

Figure 4 displays the recognition results of pseudo fault EXX using fractal analysis of VEs coordinates and machine error parameters, respectively. The exact pseudo-fault of EXX occurred at the 7<sup>th</sup> SAMBA measurement, and it could be well detected by the fractal assessment of VE coordinates (D, R2, Index). While the fractal of machine error parameters-R2 and Index parameters had a worse performance in the change detection. This change could only be detected by the D and G measures. Similar conclusions were also drawn from fractal of VEs coordinates and fractal of machine error parameter results for the induced pseudo fault caused by the change of EYX.

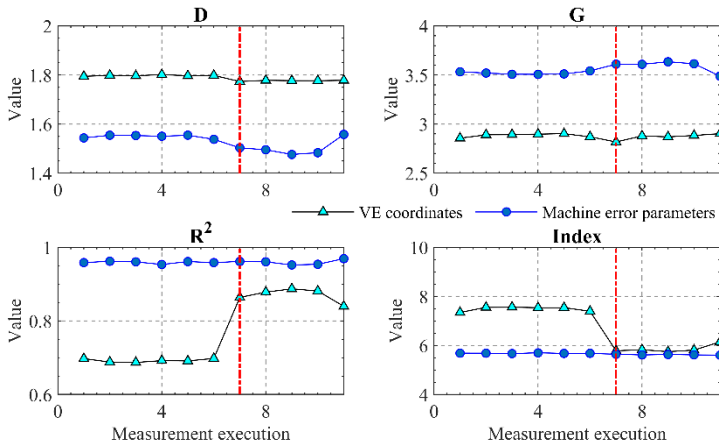


Figure 4. Fractal analysis results of pseudo faults EXX

### 4.3 Simulated EZX fault analysis

To deeply verify the performance of fractal measures of machine error parameters, a fault caused by the gradual and steep change of EZX error, which is not included by the estimated result of the AxiSAMBA™ software, was also simulated. Figure 5 reveals the fractal analysis of EZX fault using the inputs of VE coordinates and machine error parameters.

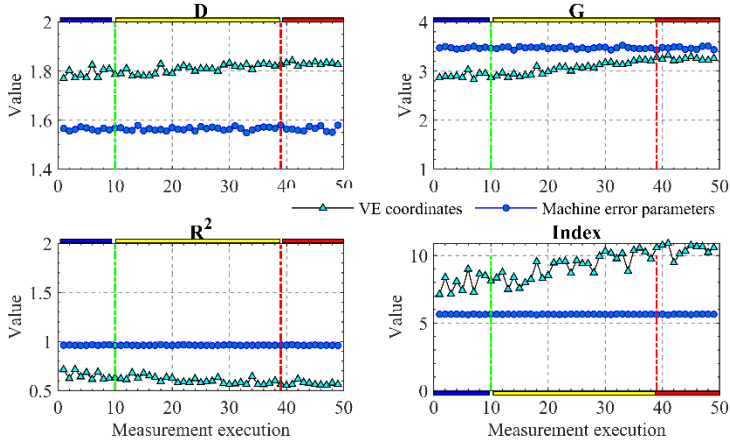


Figure 5. Fractal analysis results of simulated EZX fault using machine error parameters and VEs coordinates; the blue, yellow and red bars show the development of a fault from its normal state, transition state (gradual change) to faulty state; This procedure also works for Figure 6.

The simulated EZX fault could be well recognized in the transition period by the VEs fractal measures D, G and Index. While it cannot be detected by the

fractal analysis of machine error parameters. Similar results could also be found from the EZX fault with steep change.

#### 4.4 Simulated gradual/steep change fault analysis

13 simulated faults with the gradual/steep change of the modelled error of the AxiSAMBA™ software were also included. The recognition result of ECOY fault with steep change is shown in Figure 6. The occurrence time of the simulated steep change fault is 11th and it could be mostly detected by the fractal of VE coordinates and machine error parameters expect fractal measure of VE coordinates Index.

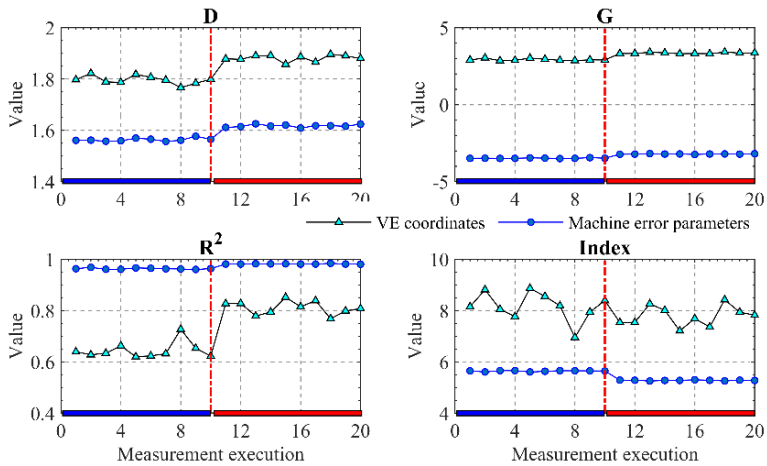


**Figure 6.** Fractal analysis results of simulated ECOY fault using machine error parameters and VEs coordinates

Similar findings could also be obtained from the un-shown recognition results of gradual/steep change faults. Figure 7 shows the statistical results of the performance of fractal measures in the simulated gradual/steep change faults. "1" and "0" are used to represent if a fault can be detected. Take the "0" of EA0B as an example, it means that fractal measure of VE coordinates cannot detect the fault caused by the gradual/steep change of EA0B.

The successful detection number of faults using fractal measures is shown at the bottom of Figure 7. The performance of fractal measure is related to its input. Compared with the fractal measures of VEs coordinates, the fractal measure of machine error (ME) parameters has a better performance in fault detection and the four fractal measures perform equally. As for the fractal measures of VE coordinates, G and R2 can detect more faults.

	D				G				R <sup>2</sup>				Index			
	VE		ME		VE		ME		VE		ME		VE		ME	
EA0B	0	0	1	1	0	0	1	1	0	1	1	1	0	0	1	1
EC0B	0	0	1	1	0	1	1	1	0	1	0	0	0	0	0	0
EX0C	0	0	1	1	1	1	1	1	1	1	1	0	1	1	1	1
EA0C	0	0	1	1	1	1	1	1	0	1	0	0	0	0	1	1
EBOC	0	0	1	1	0	0	1	1	0	1	1	1	0	1	1	1
EBOZ	0	1	0	0	0	1	1	1	0	0	1	1	0	0	1	1
EA0Y	0	0	1	1	1	1	1	1	1	1	1	1	0	1	1	1
EC0Y	1	1	1	1	1	1	1	1	1	1	1	1	0	0	1	1
EY0S	0	0	1	1	1	1	1	1	1	1	1	1	0	1	1	1
EZ0S	0	1	1	1	1	1	1	1	1	1	1	0	1	1	1	1
EXX1	0	0	1	1	0	0	1	1	1	0	1	1	0	0	1	1
EYY1	0	1	1	1	1	1	1	1	1	1	1	1	1	1	1	1
EZZ1	0	0	1	1	1	1	1	1	0	1	1	1	0	0	1	1
	1	4	1	1	8	1	1	1	7	1	1	9	3	6	1	1
			2	2		0	3	3		1	1			2	2	

Figure 7. Statistical results of fractal measures in fault recognition

## 5 Discussion

In this paper, a novel application of fractal analysis in machine error parameters has been proposed to quantitatively assess the precision state of machine tools. This new method was validated by the real C-axis encoder fault, simulated gradual and steep change fault, and pseudo-faults EXX and EYX. As a comparison, fractal assessment of volumetric error coordinates was also conducted. Four fractal measures perform differently in the detection of machine tool precision state. It may be related to the fault type, and it is not recommended to select one based on some cases. For example, G measure has different performances in the real, simulated and pseudo faults. The simulated faults demonstrated that fractal analysis of machine error parameters could have better performance than fractal analysis of VEs coordinates when the fault is caused by the change of one modelled error parameter. However, when the fault is caused by the unmodeled error parameter, fractal analysis of machine error parameters may be ineffective. In this case, fractal assessment of VE coordinate is needed. Therefore, in practice, the two data processing methods could be used together to access the precision of machine tools.

## 6 Conclusions

Therein, fractal analysis of machine error parameters has been found to be a useful solution for the assessment of machine tool precision state. The proposed solution

shows a relatively good detection of the faults related to the modelled or contained machine error parameters. Combined with the fractal assessment of VE coordinates, the change of machine tool precision state could be well detected. Furthermore, the uncertainty and various fault detection performance of the proposed method will be substantially examined with simulated faults caused by the change of multiple machine error parameters rather than one single error parameter.

## **Acknowledgments**

The authors express their sincere thanks for G. Gironne and V. Mayer for conducting the experimental results and supporting in the SAMBA simulation work. This research is supported by the Natural Sciences and Engineering Research Council of Canada (NSERC) and China Scholarship Council.

## **References**

- [1] R. Ramesh, M. A. Mannan, and A. N. Poo, Error compensation in machine tools — a review: Part I: geometric, cutting-force induced and fixture-dependent errors, *International Journal of Machine Tools and Manufacture*, vol. 40, no. 9, pp. 1235-1256, 2000.
- [2] H. Schwenke, W. Knapp, H. Haitjema, A. Weckenmann, R. Schmitt, and F. Delbressine, Geometric error measurement and compensation of machines—An update, *CIRP Annals*, vol. 57, no. 2, pp. 660-675, 2008.
- [3] Kanglin Xing, Sofiane Achiche, and J. R. R. Mayer, Five-axis machine tools accuracy condition monitoring based on volumetric errors and vector similarity measures, *International Journal of Machine Tools and Manufacture*, vol. 138, pp. 80-93, 2019.
- [4] Kanglin Xing, J. R. R. Mayer, and Sofiane Achiche, Machine Tool Volumetric Error Features Extraction and Classification Using Principal Component Analysis and K-Means, *Journal of Manufacturing and Materials Processing*, vol. 2, no. 3, p. 60, 2018.
- [5] Kanglin Xing, Xavier Rimpault, J. R. R. Mayer, Jean-François Chatelain, and Sofiane Achiche, Five-axis machine tool fault monitoring using volumetric errors fractal analysis, *CIRP Annals*, vol. 68, no. 1, pp. 555-558, 2019.
- [6] Kanglin Xing, Xavier Rimpault, J. R. R. Mayer, Jean-François Chatelain, and Sofiane Achiche, Quantitative assessment of machine tools condition through fractal analysis of volumetric error vector similarity measures, *Procedia CIRP*, vol. 86, pp. 145-150, 2019.
- [7] Maryam Jamshidi, Xavier Rimpault, Marek Balazinski, and Jean-François Chatelain, Fractal analysis implementation for tool wear monitoring based on cutting force signals during CFRP/titanium stack machining, *The International Journal of Advanced Manufacturing Technology*, vol. 106, no. 9, pp. 3859-3868, 2020.
- [8] Xavier Rimpault, Marek Balazinski, and Jean-François Chatelain, Fractal Analysis Application Outlook for Improving Process Monitoring and Machine Maintenance in Manufacturing 4.0, *Journal of Manufacturing and Materials Processing*, vol. 2, no. 3, p. 62, 2018.
- [9] J. R. R. Mayer, Five-axis machine tool calibration by probing a scale enriched reconfigurable uncalibrated master balls artefact, *CIRP Annals*, vol. 61, no. 1, pp. 515-518, 2012.
- [10] N. Alami McHichi and J. R. R. Mayer, Axis Location Errors and Error Motions Calibration for a Five-axis Machine Tool Using the SAMBA Method, *Procedia CIRP*, vol. 14, pp. 305-310, 2014.
- [11] G. Losa, Ristanović, D. , Ristanović, D. , Zaletel, I. and Beltraminelli, S., From Fractal Geometry to Fractal Analysis, *Applied Mathematics*, vol. 7, pp. 346-354, 2016.
- [12] Xavier Rimpault, Jean-François Chatelain, Jolanta Ewa Klemberg-Sapieha, and Marek Balazinski, Burr height monitoring while drilling CFRP/titanium/aluminium stacks, *Mechanics & Industry*, vol. 18, no. 1, p. 114, 2017.

## **Session 2**

### **Design**

# Design of a structural strain measurement system based on slotted photomicrosensors

S. Fletcher<sup>1\*</sup>, D. Chuku<sup>1</sup>, T. Furness<sup>1</sup>, A.P. Longstaff<sup>1</sup>

<sup>1</sup>*Center for Precision Technologies, University of Huddersfield, Huddersfield, UK*

## Abstract

Structural deformation in manufacturing machines, either due to thermal or finite stiffness effects, can affect their performance. Measurement of strain of a structural member is common for many safety critical systems but is not used very often for precision machinery to enable correction of resulting errors. This may be due in part to the temperature sensitivity of strain gauges or the complexity of installing many sensors to characterise complex bending of large structures often found on machines. This paper describes the design of a new strain sensing system based on a low-cost displacement sensing technique employing off-the-shelf slotted photomicrosensors and connecting rods to facilitate long range measurement. A small framework of a series of sensors is simulated with detailed analysis of the design. Finally, some preliminary validation results are presented which show sub-micron resolution and repeatability.

## 1 Introduction

Structural deformation in machinery either due to thermal or finite stiffness effects, can affect their performance. Measurement of strain of a structural member is common for many safety critical systems but is not used very often for precision machinery to enable correction of resulting errors. This may be due in part to the accuracy of some strain gauges, the complexity of installing a large number of sensors to characterise complex bending often found on machines and the associated costs. An example where this has been applied is by Biral [2] where a series of fibre optic sensor shave been arranged on a large milling machine structure. A significant challenge of optical methods is the cost of spectrometry. Strain gauges have significant cost advantages and can be applied to flat or curved surfaces, but they are not direct measurement of the overall distortion effect. A review of high resolution sensors that could be used to create strain measurement systems is provided by Fleming [3].

In this paper, a new sensor is design around a slotted photomicrosensor (PMS) arrangement described in [1] which provides differential output that compensates for some of the uncertainty contributors. Figure 1 shows the principal of operation. When the shutter (sometimes called a shield) moves, two sensors allow more light transmission while two allow less. This new design uses a slightly different make and model, a Kingbright KRB011 (<£1 GBP). This has a very small aperture giving 90% change in output for less than 100 µm of movement of the shield (referred to as the shutter in this article).

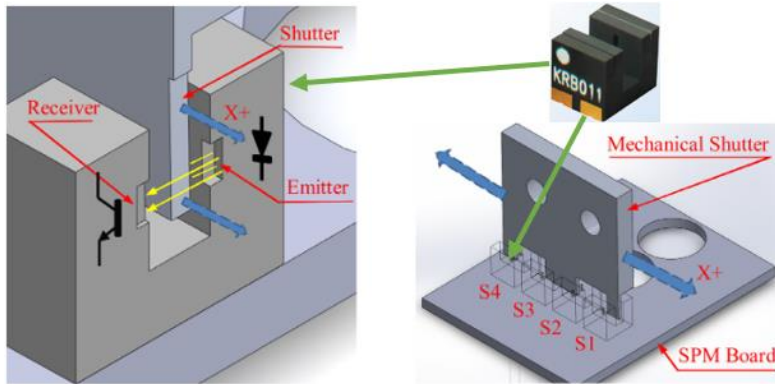


Figure 1. (a) Cross section view of a single sensor and shutter and (b) schematic of the overall system [1].

Equation 1 represents the differential output proportional to displacement of the shutter with output voltages of all the sensors.

$$V_{out} = \frac{[(\frac{v_1-v_2}{2}) + (\frac{v_3-v_4}{2})]}{2} \quad (1)$$

Where,  $v_1$  to  $v_4$  are the sensor voltages and  $V_{out}$  represents the average differential voltage. This method cancels out source voltage drift and potentially differential thermal expansion. Potdar [1] reported a sensitivity of 0.1648 V/µm, a resolution (noise floor) of 21 nm and an accuracy of ±1% of full-scale range of 20 µm.

To exploit the advantages of this sensor to detect displacement as part of a structural strain measurement system, a sensor housing and framework have been created with uncertainty and cost consideration to exploit the key benefits.

## 2 Design analysis

The key aims for the design of the displacement sensor based on the operating principal and application are:

1. Frictionless motion for sub-micron bi-directional movement (section 2.1).
2. Single degree-of-freedom motion to reduce cross talk (section 2.1).
3. Minimise thermal influence (section 2.3.1).
4. Simple manufacture and assembly (section 2.1).
5. Easy installation as a retrofit system and sensor replacement (section 2.2).

Transmissive slotted PMS and low sample rate Analog to Digital Converters (ADCs) are ultra-low cost these days, so restrictions on manufacture in point 4 will influence the design. In this case, a plastic 3D printed solution was adopted, eliminating complex machining of small features and simplifying assembly. The design therefore tries to exploit this method and considers issues such as overhangs, low accuracy, anisotropic properties and poor surface finish.

Before examining the detail in the design for the various requirements, an overview is provided here to aid in the visualisation and operation of the sensor module going forward. Firstly, Figure 2 shows the two main components that make up the sensor housing, with all parts being 3D printable without support structures. The principal of operation of the assembly and setup as a strain sensing framework are shown in Figure 7 and Figure 8 respectively. The PMS circuit board sits in the static part as indicated in Figure 2 (a).

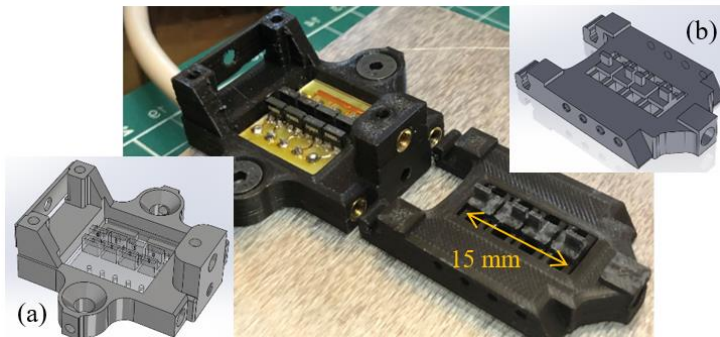


Figure 2. Three main components of the sensor housing (a) static part (with location of PMS circuit board indicated), (b) moving part,

## 2.1 Flexure system

In order to eliminate friction in the mechanism, a flexure system was employed for relative movement between the two parts of the sensor. A disadvantage of the flexure system is the addition of mechanical stiffness therefore the rigidity needs to be as low as possible to minimise forces in the joining mechanism (Figure 8). Figure 3 (a) shows horizontal and Figure 3 (b) vertical flexure elements to constrain the five unwanted degrees of freedom. See Figure 7 for the deflected shape. Figure 3 (b) inset shows the flexure is push fit with three line contact to constrain vertically, reduce stiffness and eliminate bi-directional hysteresis.

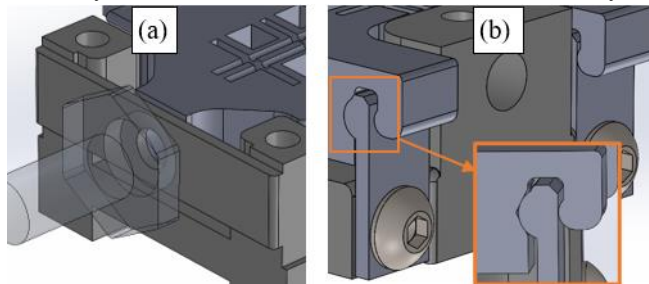


Figure 3. Horizontal (a) and dual vertical (b) flexures for one degree-of-freedom motion

## 2.2 Sensor adjustment post installation

There is significant challenge during assembly to set all 4 sensors close to the middle of their range to maximise the linear regions in the outputs. The KRB011 are soldered onto the circuit board using a fixture to achieve good uniformity. However, it is not sufficiently accurate when combined with the 3D printed housing to get the same voltage output at the nominal position. Individual adjustment is required with very fine control given that the sensitivity of the sensor is so high. Figure 4 shows the four narrow detector slits partially covered by the shutter fingers, all which need individual adjustment. Figure 5 shows M2 grub screws used to push against a taper on a dual flexure to create axial motion of each shutter. The simulation result in Figure 6 shows the single degree of freedom adjustment.

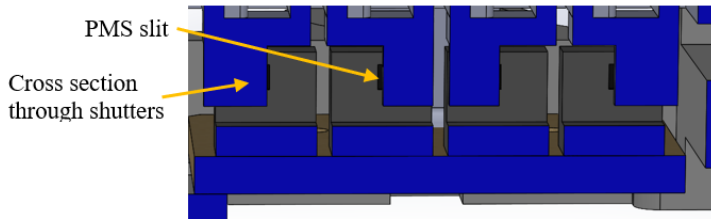


Figure 4. Assembly cross-section showing shutter partial coverage of detector slit

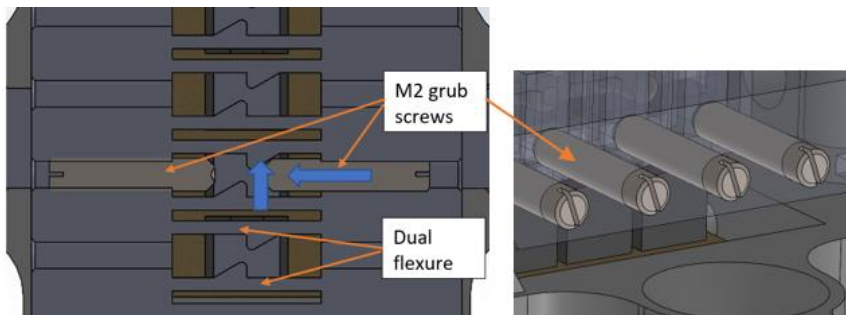


Figure 5. Shutter adjustment mechanism

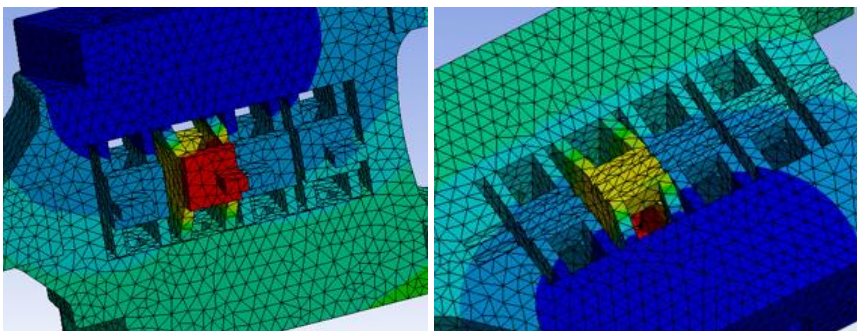


Figure 6. Simulation of the resulting motion of the shutter when adjusted

### 2.3 Sensor simulation

Preliminary validation of the sensor node design is through Finite Element Analysis (FEA). Firstly, the static stiffness was determined using a 1N force applied axially to the moving part of the assembly. The front flexure thickness has already been reduced to the minimum thickness possible using a typical 3D printer nozzle size of 0.4 mm. A Deflection of  $5.9 \mu\text{m}$  equates to a stiffness of  $0.17 \text{ N}/\mu\text{m}$ . The variation in displacement of the face of each shutter was  $0.3 \mu\text{m}$  cause by tension/compression in the housing, a linear constant that is easily calibrated.

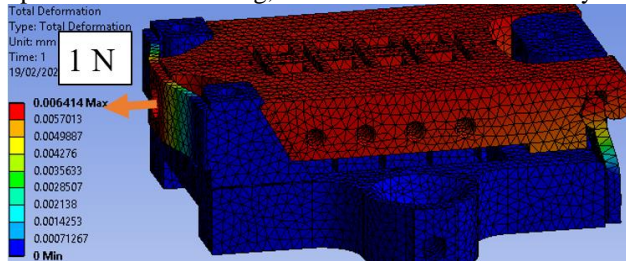


Figure 7. Deflection of the sensor with 1N axial force applied

#### 2.3.1 Multi-sensor strain setup

The joining members provide flexibility over the range of structure being monitored but are also most susceptible to thermal error given that environmental temperature variability may be high in embedded machine monitoring applications. Invar, Uni-directional CFRP and Zerodur bars are all relatively thermally stable options but increase in cost with performance. Figure 8 shows a test setup using 200mm long 10mm square section Zerodur bars, using which loses just 30% of the strain due to the sensor flexure forces. Again, for different rod materials, the stiffness will be calibrated. Residual thermal error includes uncertainty in expansion coefficient and temperature measurement accuracy. At 10 % uncertainty applied to invar ( $1.2\text{ppm}$ ) and  $0.1 \text{ }^\circ\text{C}$  (PT100) respectively, a basic estimate gives  $(0.1 \times 1.2) \times 0.1 \times 0.2 = 0.0024 \mu\text{m}$  for 200mm bar.

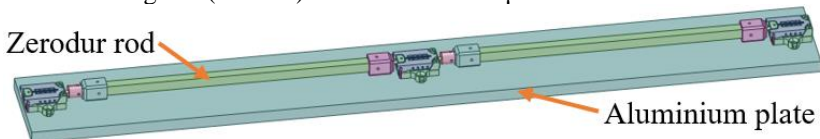


Figure 8. Setup of sensor modules to measure strain of a metal beam.

Although the sensor module is small, 3D printed plastics can have high thermal expansion coefficient resulting in a differential between the moving shutter part and the circuit board assembly. FEA was used to simulate this effect using an average convective coefficient of  $6 \text{ W}/\text{m}/^\circ\text{C}$  and a sink temperature changing from  $20 \text{ }^\circ\text{C}$  to  $45 \text{ }^\circ\text{C}$  in five steps of  $5 \text{ }^\circ\text{C}$ . The expansion of the plate between modules was  $200 \mu\text{m}$ , while the sensors measured  $100 \mu\text{m}$ , an error of  $40 \mu\text{m}$  after accounting for 30% rod tension loss. Using the differential between the inside and outside PMS pairs, which relates to the thermal error, a linear correction can be made which leaves a residual error below  $2 \mu\text{m}$ , much of which is a transient issue with the step change in the simulated ambient conditions.

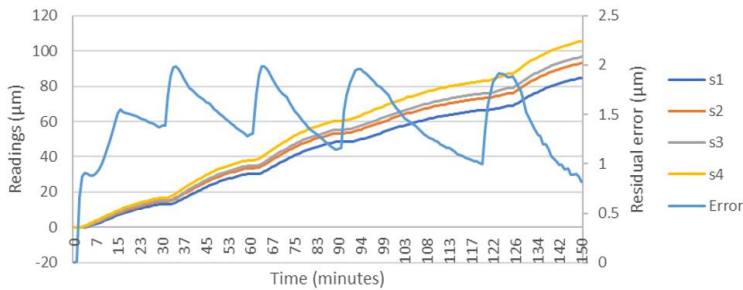


Figure 9. Residual thermal error after differential thermal error correction

## 2.4 Prototype result

The prototype shown in Figure 2 was assembled and preliminary repeatability tests completed using a Thorlabs closed-loop controlled Piezo actuator. Five bi-directional, 20  $\mu\text{m}$  displacements were recorded, indicating an average standard deviation of 11.4 mV for 6 different displacements (bi-directional), equating to 0.047  $\mu\text{m}$  using a sensitivity 0.1648 V/ $\mu\text{m}$  [1].

## 3 Conclusion

A new sensor design has been created that exploits ultra-low-cost (<£1 GBP) slotted PMS to create a displacement sensor that can be configured in a framework for measuring structural distortion. A 3D printable design has been used to reduce manufacturing cost of an intricate flexure design. Simulation results show the low stiffness to reduce compression/tension losses in the connection rods to 30%. Differential thermal error can be corrected using the sensor reading. A prototype has been built using standard PLA material and preliminary functional tests completed. The standard deviation from 5 bi-directional displacement tests using a Piezo actuator is 0.047  $\mu\text{m}$ . Further work is planned to fully evaluate the long-term accuracy, including the latest low cost ADCs.

## Acknowledgement

The authors gratefully acknowledge the UK's Engineering and Physical Sciences Research Council (EPSRC) funding of the Future Metrology Hub (EP/P006930/1)

## References

- [1] Potdar, A. A., Fletcher, S., & Longstaff, A. P. "Performance characterisation of a new photo-microsensor based sensing head for displacement measurement". *Sensors and Actuators, A: Physical*, 238, 2016, p 60-70. doi: <https://doi.org/10.1016/j.sna.2015.12.007>.
- [2] F. Biral, P. Bosetti, R. Oboe, F. Tondini. "A new direct deformation sensor for active compensation of positioning errors in large milling machines." *International Workshop on Advanced Motion Control, AMC*. 2006. p126 - 131. doi: 10.1109/AMC.2006.1631645.
- [3] A. J. Fleming, "A review of nanometer resolution position sensors: Operation and performance", *Sensors and Actuators A: Physical*, v190, 2013, p106-126. doi: <https://doi.org/10.1016/j.sna.2012.10.016>.

# **Modal analysis of a sensing CBN grinding wheel**

Lai Hu, Jun Zha, Zhenggang Chen, M. Bilal, Yaolong Chen\*  
*School of Mechanical Engineering, Xi'an Jiaotong University, 28  
Xianning Road, Xi'an, Shaanxi 710049, P.R. China.*  
*\*Correspondence: [chenzwei@mail.xjtu.edu.cn](mailto:chenzwei@mail.xjtu.edu.cn);*

## **Abstract**

Grinding is one of the high-speed and high-precision processes. In the grinding process, the instantaneous temperature and cutting force of the grinding wheel are two important factors that affect the grinding accuracy. In order to further improve the grinding accuracy, this study mainly designs a sensing grinding wheel. The original grinding wheel structure has been reformed. The temperature and force sensors are embedded into CBN grinding wheel to form sensing grinding wheel. In this paper, considering the influence of the basal body structure, the influence of the grinding accuracy is also very large. Therefore, the vibration frequency analysis of the basal body is also carried out. From the analysis of experimental data, the vibration frequency of the sensing grinding wheel basal body takes the first four orders, and the values are 292.469 Hz, 350.161 Hz, 386.639 Hz and 423.641 Hz, respectively. The vibration frequency ratios are 2.93%, 1.84%, 1.82% and 1.41%, respectively. This value absolutely meets the processing requirements. The idea of sensing grinding wheel lays a good foundation for the follow-up research of adaptive grinding.

Key words: Sensing grinding wheel, Temperature sensor; Force sensor; Vibration frequency

## **1 Introduction**

The research on high-efficiency grinding technology has always been one of the engineering problems that is difficult to break through. The methods to improve grinding accuracy are basically to consider grinding force and grinding temperature. However, there are many researches on grinding accuracy. For example, early Hashimoto F et al. [1] developed an ultra-precision diamond

forming grinder for diamond grinding wheels and a new type of diamond forming grinder to provide grinding accuracy and surface quality. Another example is Zhang X C et al. [2] who studied the micro-vibration phenomenon in grinding, established the mathematical model of aspheric spherical radius deviation caused by micro-vibration, and developed a dynamic high-precision micro-vibration measuring device with an accuracy of  $0.02 \mu\text{m}$ . Zhang M et al. [3] developed an adaptive grinding method for precision casting blades with geometric deviation to improve the processing accuracy, efficiency and automation level. At the same time, some authors [4-5] have also carried out other grinding research. The main purpose is also to improve the grinding accuracy. In this paper, the structure of grinding wheel is innovatively designed. The temperature and force sensors are embedded in the grinding wheel basal body, and the grinding temperature and grinding force are collected. So as to analyze the relationship between temperature and force. This method is also to improve grinding accuracy and efficiency. This paper also analyzes the modal of this sensing grinding wheel basal body. The reliability and practicability of this design are verified again.

## 2 Structural development of sensing grinding wheel

Based on the current situation of grinding wheels, this paper develops a sensing grinding wheel. In the grinding process, it is necessary to collect the grinding force and temperature and analyze the relationship between them. Therefore, it is necessary to use wireless transmission to collect force and temperature. The force sensor wireless transmission module is shown in figure 1. The sensing grinding wheel is shown in figure 2.

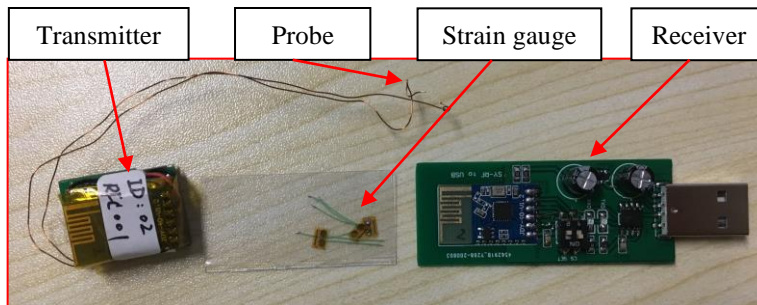


Figure 1: Force sensor wireless transmission module.

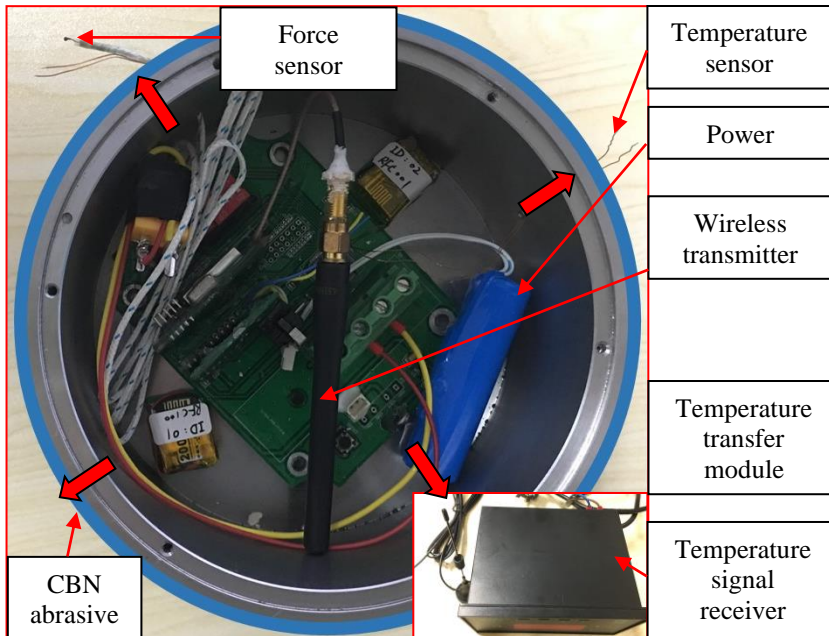


Figure 2: Sensing grinding wheel.

According to figure 1, the force sensor mainly uses strain gauges to measure grinding force. When the shape of the strain gauge changes, it is transmitted to the receiving end through the wireless transmitting end and processed by the signal.

The same transmission mode is used for temperature collection and analysis. As shown in figure 2, that CBN abrasive is adhere to the periphery of the maximum size of the grinding wheel substrate, with a thickness of about 5 mm and a width of about 25 mm. Simultaneously, four groups of holes are respectively opened in the basal body, which are distributed at 90°. The probes of the force sensor and temperature sensor across the holes for data collection. The force signal and temperature signal are actually received by an external wireless receiver. Finally, the two collected signals are processed to obtain the correlation between grinding force and temperature.

### 3 Vibration mode analysis of sensing grinding wheel basal body

Before the sensing grinding wheel is used, the basal body needs to be analyzed. Because the structure of the basal body will have a great influence on the grinding accuracy. In the analysis of the basal body, this paper mainly analyzes its vibration frequency. The purpose is to analyze the relationship between the vibration frequency and the working frequency when the grinding wheel rotates.

So as to verify whether the design of the basal body structure is reasonable. First, let the basal body be in a free state and analyze its vibration frequency, as shown in figure 3.

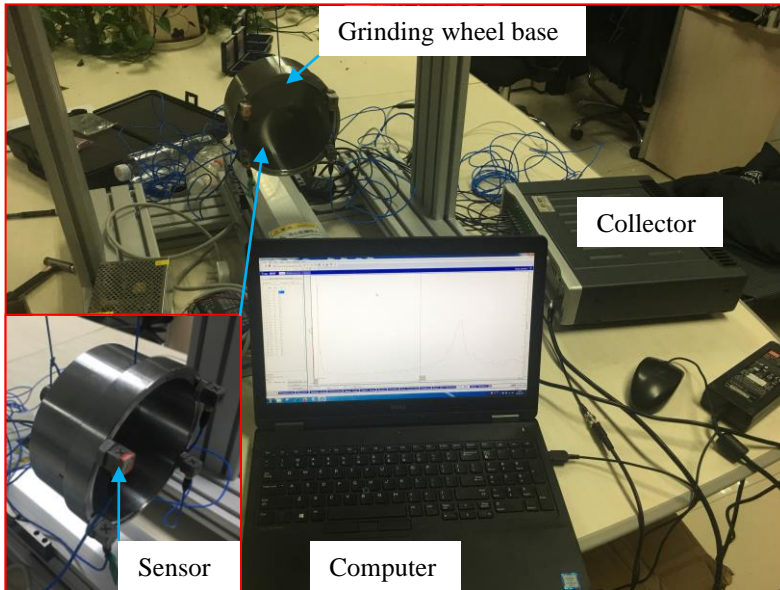


Figure 3: Vibration frequency analysis of sensing grinding wheel basal body.

As shown in figure 3, four sensors are simultaneously distributed on the basal body and tested in two groups. Take X + direction as the knocking point and carry out force hammer knocking. Thus, 8 sets of data and summed data are obtained, as shown in figures 4 and 5, respectively.

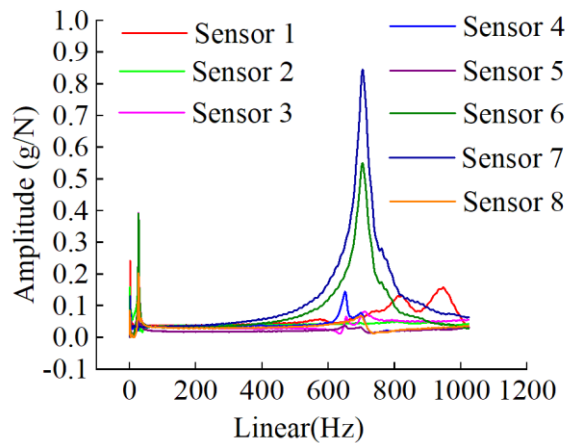


Figure 4: 8 sets of test data.

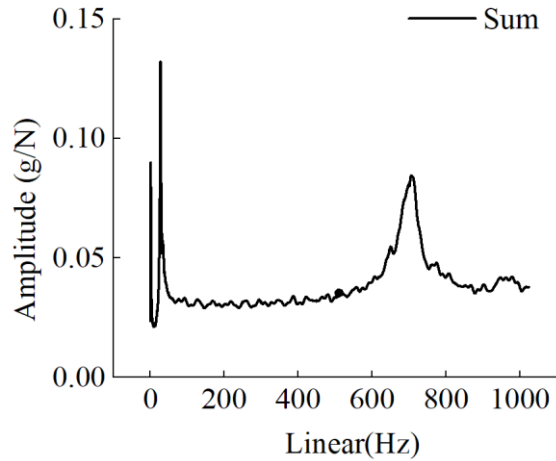


Figure 5: Summing data.

As shown in figures 4 and 5, a vibration frequency is desirable between that amplitude of 0-0.05 g/N. Therefore, the first four modal values are extracted: 292.469 Hz, 350.161 Hz, 386.639 Hz and 423.641 Hz. The vibration frequency ratios are also calculated, which are 2.93%, 1.84%, 1.82% and 1.41%, respectively. In the actual vibration frequency analysis, the first order is mainly analysed. From the equation  $n=60f$ , it is concluded that when  $f$  vibration frequency is 292.469 Hz, the grinding wheel rotation speed is about 17548 r/min. It can be inferred that the natural frequency of the grinding wheel will be greater than the working frequency only when the test speed of the sensing grinding wheel should be less than 17548 r/min. So that resonance does not occur. Because this study mainly tests the instantaneous temperature and force during grinding and analyzes the relationship between them. Therefore, it is not necessary to reach a very high speed. This shows that the design of sensing grinding wheel is reasonable and feasible.

#### 4 Conclusion

This paper mainly makes innovations to the traditional grinding wheel. In order to further obtain the relationship between the instantaneous temperature and force, a sensing grinding wheel was developed. Temperature and force sensors are integrated inside the grinding wheel basal body. The vibration frequency of grinding wheel basal body is emphatically analyzed, and the first four modes are proposed for analysis. Taking the first order vibration frequency as a reference, reverse analysis shows that the test speed of sensing grinding wheel should be less than 17548 r/min. At the same time, the next step is to use this sensing grinding wheel to carry out mass grinding tests. On the contrary, the test data can be used to verify and optimize the sensing grinding wheel.

## **Funding**

This research was funded by the National Key R&D Program of "Manufacturing Basic Technology and Key Components" (No.: 2018YFB2000502 and No.: 2020YFB2009604).

## **References**

- [1] Hashimoto F , Kanai A . High Precision Trueing Method of Regulating Wheel and Effect on Grinding Accuracy[J]. CIRP Annals - Manufacturing Technology, 1983, 32(1):237-239.
- [2] Zhang X C , Cao G H , Nie F M , et al. Study on influence of micro-vibration during the optical aspheric surface ultra-precision grinding on forming accuracy[J]. Acta Armamentarii, 2012, 33(9):1066-1069.
- [3] Zhang M , Chen T , Tan Y , et al. An adaptive grinding method for precision-cast blades with geometric deviation[J]. International Journal of Advanced Manufacturing Technology, 2020(3).
- [4] Matthias S , Franz H , Alexander P , et al. Adaptive Grinding Process (AGriPro) - Prevention of Thermal Damage using OPC UA Technique and in-Situ Metrology[J]. Journal of Manufacturing ence and Engineering, 2017.
- [5] Malkin, S., and Guo, C., 2007, "Thermal Analysis of Grinding," Ann. CIRP, 56(2), pp. 760–782.

# **Session 3**

## **Process Control**

## **Optimization of volumetric error calibration procedures based on a digital twin**

B. Iñigo<sup>1</sup>, N. Colinas-Armijo<sup>1</sup>, G. Aguirre<sup>1</sup>, L.N. López de Lacalle<sup>2</sup>

<sup>1</sup>*Design and Precision Engineering Group, IDEKO, 20870 Elgoibar, Basque Country, Spain*

<sup>2</sup>*Department of Mechanical Engineering, EHU-UPV, 48013 Bilbao, Basque Country, Spain*

### **Abstract**

Following the Industry 4.0 trend, real time monitoring systems have become a crucial element for machine tool manufacturers in order to monitor the state of the machine during its whole lifetime. Concerning the field of machine errors and volumetric accuracy, automatic or semi-automatic measurement systems that can be integrated in the machine are becoming of major importance, in order to perform fast machine calibration and verification procedures. Repeating such measurements frequently allows the user and/or the manufacturer to monitor the volumetric performance of the machine on a day to day basis and take the corresponding preventive actions without affecting the production.

In order to implement a measurement system in every machine and to use it periodically, measurement time and equipment cost are critical in these applications. The approach presented in this work is based on measuring calibrated artefacts within the working volume and extracting the required information on the accuracy of the machine.

Due to the necessity of optimizing different aspects, a Digital-Twin based calibration and compensation procedure is presented. Several aspects of the calibration and compensation process are optimized in order to find the best measurement strategy for each application according to volumetric performance-based criteria. A 3-axis moving-column type milling machine is selected as case study. The resulting calibration strategy represents a cost and time effective procedure that can be integrated in a machine.

## **1 Introduction**

Volumetric accuracy in machine tools was defined as the ability of the machine to produce accurate 3D shapes [1]. The development of volumetric error mapping

strategies, and the compensation of the measured systematic errors, has been the focus of many research projects over the time [2].

There is a trend towards the integration of self-diagnosis systems in machine tools following *Industry 4.0* principles, and the verification and recalibration of volumetric accuracy is one of the key requirements. Artefact based calibration systems find here an important advantage due to their much lower cost compared to laser tracker-based solutions, and they are therefore a reasonable alternative to explore.

In [3] a virtual calibration and compensation procedure was presented, capable to simulate the whole process in order to optimize different aspects of the procedure. This document is presented as a continuation of the this work, but a different approach is used in the modelling of the errors of the virtual machine. A cantilever-type travelling column 3-axis milling machine will be taken as the case study, calibrated with a 1D ball array. Details of the machine are given next.

Kinematic chain: Tool-Y-Z-X-Bed-Workpiece

Workspace (mm): X(0-4000), Z(0-1500), Y(0-1300)

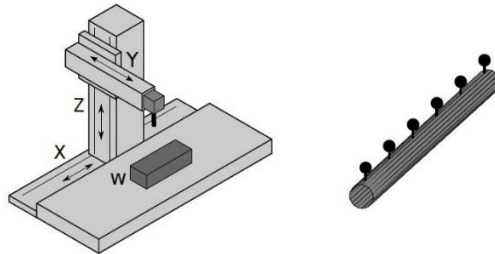


Figure 1. (left) Machine kinematic structure; (right) 1D ball array

## 2 Virtual optimization of the error mapping procedure

The general structure of the virtual error mapping and compensation procedure was presented in [3]. The process is divided in 3 main stages: error mapping test, model estimation and validation test. Two Digital Twins of the machine are used in order to simulate the original machine measured and the compensation model obtained. Additional details of the modelling of these digital twins are given in section 3.

## 3 Digital twin of the machine tool

As mentioned in section 1, cantilever-type travelling column 3-axis milling machine with a large working volume will be taken as the case study. Two digital twins of the machine are required in the implementation of the virtual error mapping procedure. The machine model  $M$  is the one to be calibrated and can include as many effects as needed to be considered in the analysis, as the compensation model  $C$  is the one used to predict the machine behaviour.

The virtual machine models  $VM$  provide the position of the tool centre point (TCP) in the machine's main coordinate system, in function of the programmed axis positions  $X(x, y, z)$ , the tool offset  $t$ , and any other effect that may deviate it, such as guiding errors, backlash, thermal effects, etc., which are parameterized in the model by a set of parameters  $E$ .

$$\begin{cases} M = VM(X, t, E_M) \\ C = VM(X, t, E_C) \end{cases} \quad (1)$$

### 3.1 Modelling strategy

The digital twins presented in the previous section are based in the successive multiplications of Homogeneous Transformation Matrices that represent the kinematics of the specific machine [4]. Translation and rotation of machine axes are included in these transformations, as well as the small displacement and rotation due to different error sources [3].

### 3.2 Machine model

A key element to the success of the optimization procedure presented here is the proper definition of the model that will represent a realistic behaviour of the machine to be calibrated. The magnitude of each error, their shape, how fast they change within the workspace, the relevance of thermal and flexibility errors determines aspects such as the number of measurements needed or the complexity of the compensation model. The experience and engineering judgement is thus important for defining a proper machine model.

In this work, an approach based on the combination of finite element (FE) model simulation results and synthetically generated geometric errors will be used.

### 3.3 FE modelling

The goal of the FE modelling and simulation is to obtain the flexibility behaviour of the machine under the influence of gravity. The interaction between the column (Z axis) and the ram (Y axis) in different axes positions will play a major role in this aspect, as non-rigid body behaviour is expected in this type of machines. This "cross-effect" between axes is described in [5].

A model of a real milling machine has been developed [6]. ANSYS software has been used to perform the simulations and the interfaces between moving parts of the machine has been modelled in a way that relative movement is allowed between them. A 9x15x13 3D point grid has been defined covering the machine volume, positioning the 3 linear axes of the machine in each of them. A static structural simulation has been carried out at each axis position, taking the influence of the gravity under consideration, and the deviations of the Tool Center

Point (TCP) have been obtained in each case. This effect is incorporated to machine model  $M$  with an interpolated 3D error grid.

### 3.3.1 Synthetic polynomial errors

In addition to the errors described in the previous section, synthetically generated polynomial errors have been included in the machine model. These errors intend to reflect the effects that cannot be simulated in a FEM model, i.e., guideways and carriage shape errors, scale errors and other local effects. These errors on individual machine components are expanded to the TCP in the form of positioning, straightness and angular errors.

These geometric errors of the machine have been modelled based on orthogonal Legendre polynomials, which are properly suited to model the characteristic shapes of such errors [7]. Equation 2 shows an example of the positioning error of the X axis and equation 3 shows the definition of orthogonal Legendre polynomials.

$$EXX(x) = a_0 \cdot L_0(\bar{x}) + a_1 \cdot L_1(\bar{x}) + \dots + a_n \cdot L_n(\bar{x}) \quad (2)$$

$$L_n(x) = \frac{1}{2^n n!} \frac{d^n}{dx^n} (x^2 - 1)^n \quad (3)$$

$a_0$ , to  $a_n$  are the model parameters of order  $n$  for each error component, and  $\bar{x}$  is the axis position, here normalized to  $[-1,1]$  range.  $L_n$  represents the Legendre polynomial of order  $n$ . The model is defined here by assigning a uniform probability distribution to each parameter variation range (e.g.  $[-a_0, a_0]$ ).

### 3.3.2 Evaluation of the volumetric error

The volumetric error distribution  $VE_i$  is used as the evaluation criteria for the resulting accuracy of the virtual machine model. It is defined here as the difference between the virtual machine model  $M$  and the same model with all error parameters  $E_M$  set to 0 (i.e. an 'ideal' machine), evaluated in a set of  $X_i$  machine positions (60x20x20 in this work) distributed over the workspace:

$$VE_i = \|M(X_i, t, E_C) - M(X_i, t, 0)\| \quad (4)$$

The volumetric error  $VE$  is defined here as the rms value of the volumetric error distribution  $VE_i$ , and it is used as a measure of the global errors of the machine. By performing Monte Carlo simulations on different combinations of the families of machines defined by the parametric digital twin  $M$ , the probability distribution for the volumetric error distribution  $VE_i$  characterizing this family of machines is obtained (see Figure 2). A volumetric error of 11.9 micrometres is obtained. In Figure 2 resulting volumetric error  $VE_i$  is evaluated in the machine's XY plane.

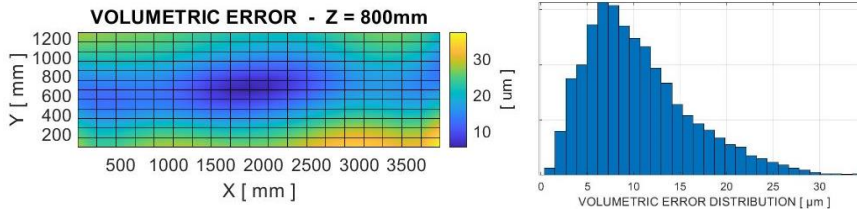


Figure 2. Left:  $VE_i$  Volumetric error of a machine model M in XY plane at  $Z=800$ . Right: Distribution of the volumetric error  $VE_i$ .

### 3.4 Compensation model

The compensation model  $C$  has a similar structure as the virtual machine model  $M$ . A 21 geometric error rigid-body model is used [8], where each of the errors to identify is approximated by parametric functions defined by Legendre polynomials described in equations 2 and 3. The influence of these errors is incorporated in  $C$  with transformation matrices previously described.

In addition to the rigid body model, extra parameters are needed to characterize the cross-effect between  $Z$  and  $Y$  axes described in section 3.3. For this purpose, 2 additional polynomials are incorporated to the compensation model  $C$ . Figure 3 shows a simplified model of the column-ram set, where both elements are modelled as 1 dimensional beams. The column is fixed to the base and the ram transmits a moment due to its own weight, depending on  $Y$  position (horizontal), while the application point depends on  $Z$  position (vertical).

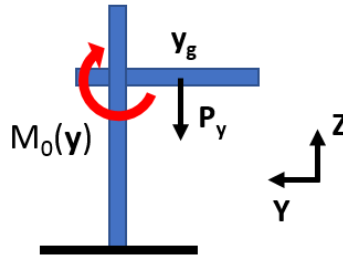


Figure 3. Schematic view of the cross-effect between column and ram.

Following this model, two component errors of the  $Z$  axis will be affected by the  $Y$  axis: The straightness in  $Y$  direction ( $E_{YZ}$ ) and the rotation around  $X$  ( $E_{AZ}$ ). Applying mechanics of materials principles equations 5 and 6 are obtained for the displacement  $E_{YZ}$  and angle  $E_{AZ}$  at the joint. Both expressions can be converted to a parametric second and first order polynomials of  $Z$  respectively, multiplied by the  $Y$  axis. The expressions are shown in equations 5 and 6.

$$E_{YZ} = \frac{-M_0(y) \cdot z^2}{2EI} \rightarrow E_{YZ}(y, z) = (b_0 + b_1 \cdot z + b_2 \cdot z^2) \cdot y \quad (5)$$

$$E_{AZ} = \frac{-M_0(y) \cdot z}{EI} \rightarrow E_{AZ}(y, z) = (c_0 + c_1 \cdot z) \cdot y \quad (6)$$

Both parametric equation are incorporated to the compensation model C, where the parameters  $b_n$  and  $c_n$  are going to be estimated in the error minimization process.

## 4 Model of the error mapping procedure

The error mapping method is based on measuring the position of the balls of a calibrated artefact with a probe incorporated in the machine head. Since the true distance between each pair of balls is known (within error mapping uncertainty in a coordinate measurement machine), it can be compared to the distances as measured by the machine in different positions to obtain information about the positioning accuracy of the machine. A non-linear least square algorithm is used to identify the geometric errors of the machine.

### 4.1 Artefact design and uncertainty

A calibrated ball artefact is used as measuring target in the error mapping process. The design of the artefact is mainly defined by the number of balls and the relative position between them.

In this work, a 1500 mm long 1D artefact with 11 balls is taken as a reference for the analysis, and the effects of its design parameters will be discussed. Regarding its design, small variations in the distribution of the balls are considered here, introducing small offsets (misalignment according to angle  $\theta$  in Figure 4) in their positions, as shown in Figure 4. The parameter  $\theta$  is selected to create vertical and horizontal offsets, as it is considered a feasible variation that does not need to change ball and ball-holder design. The number of balls,  $N_b$ , will be also optimized.

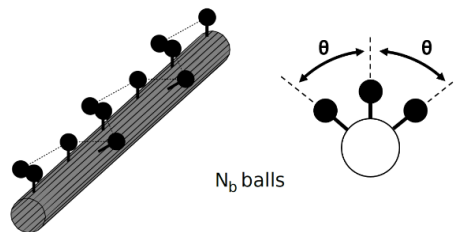


Figure 4. Artefact design according to parameters  $\theta$  (inclination angle) and  $N_B$  (number of balls)

### 4.2 Artefact position sets

The error mapping process is based on measuring the artefact in several positions to cover the workspace of the machine and provide enough information so that all the parameters of the compensation model can be identified with the expected uncertainty.

Different sets of artefact positions can be considered as base components of the measurement strategy. Direct and indirect measurement approaches should be here differentiated, as each methodology will lead to a substantially different strategies [8].

In this work, a more indirect approach is adopted in order to obtain the machine errors in an efficient way. With this approach automatization or semi automatization of the error mapping process is plausible, if a rotation mechanism is implemented in the centre point, allowing azimuth and elevation rotation. In the next figure, the position sets considered for analysis in this work are represented.

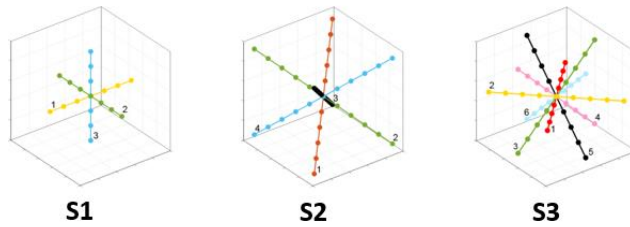


Figure 5. Artefact position sets S1, S2, S3

S1 set includes 3 positions aligned with machines 3 main axes, S2 set consists of 4 position along de 3D diagonals of the machine and the S3 set contains 6 positions crossed in the three main planes (XY, YZ, ZX) of the machine. The artefact position sets do not cover the whole workspace of the machine due to the long travel of the X axis, and therefore more than one set needs to be measured. In this work, the measurement sets are repeated along the X axis to cover the whole workspace.

### 4.3 Validation criteria

The estimated compensation model  $C$  is validated by comparing it to the virtual machine model that represents the machine that has been calibrated  $M$ .

The difference between them defines thus the volumetric compensation error distribution  $ce_i$ , and it can be evaluated in a set of  $X_i$  machine positions distributed over the workspace, in the same way as in Figure 2:

$$VCE_i = \|C(X_i, t, E_C) - M(X_i, t, E_M)\| \quad (7)$$

The volumetric compensated error VCE is defined here as the rms value of the volumetric compensation error distribution  $ce_i$ , and it is used as the quality measure of the error mapping process.

## 5 Optimization of the error mapping procedure

The use of the virtual error mapping optimization procedure presented above is demonstrated here by performing some analysis on the machine and error mapping procedure presented in previous sections. The following design

parameters have been analysed: the number of balls  $N_b$ , the ball misalignment according to angle  $\theta$  and the artefact position set  $S$ .

### 5.1 Artefact design

The optimization procedure is applied here to the optimization of the design of the artefact.

#### 5.1.1 Number of balls

The number of balls in the artefact increases the measurement time but adds measured distances and spatial resolution to the measurement. The nominal value of eleven balls leads to an axial distance between the balls of 150 mm. The artefacts with other number of balls are created keeping the total length of 1500 mm, and thus changing the distance between them. The error mapping and compensation procedure is simulated for seven artefact designs, and their reduction in volumetric error, as defined in Section 4.3, is shown in Figure 6.

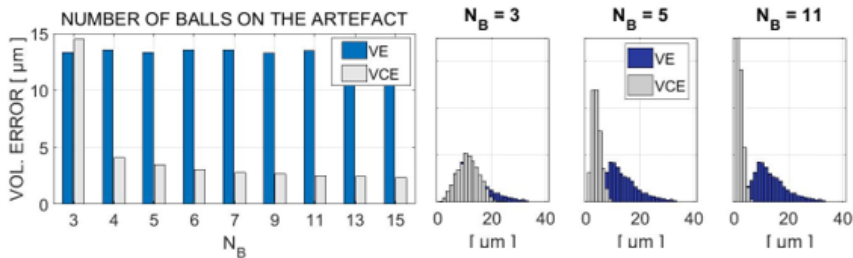


Figure 6. Volumetric error in function of number of balls  $N_b$ , for machine M (VE) and C (VCE). Error distribution is shown for cases 3, 5 and 11.

As expected, the error is reduced with higher number of balls, but the improvement is less significant when this number increases. Considering the longer measurement time, a value of 7 balls will be considered optimal in this case, as 95% of the error improvement is obtained and the time cost of adding more positions is considered inefficient.

Figure 7 shows the trajectory estimation of C for several ball number cases, evaluating the error in a Z axis linear trajectory. Significant improvement in machine trajectory estimation can be observed.

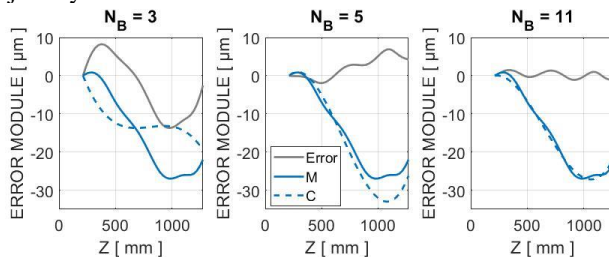


Figure 7. Trajectory estimation along Z of compensation model C (dash blue) compared to machine model M (blue). Cases for NB 3, 5 and 11 are shown.

### 5.1.2 Ball misalignment

The next analysis looks at the horizontal and vertical offset in the position of the spheres that is generated tilting alternate balls with angle  $\theta$  along the longitudinal axis of the artefact. Seven different values have been simulated.

For the analysis, strategies S2 and S2+S3 has been used, measuring the 4 main diagonals for the first case, and adding the 6 face-diagonals for the second (see Figure 5). Results are shown in Figure 8.

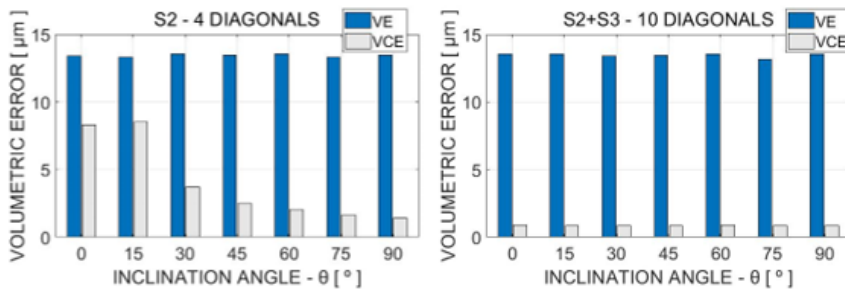


Figure 8. Volumetric error (VE) and compensated error (VCE) in function of the inclination angle  $\theta$ . Results for S2 (left) and S2+S3 (right) strategies are shown

The simulations show that misalignment of the ball array has almost no effect for the S2+S3 measurement strategy. On the contrary, with a less dense measurement strategy like S2 significant improvement is achieved. In general, it can be seen that with greater misalignment, better volumetric error improvement is achieved, and that this misalignment can allow a lower number of measurements.

## 5.2 Measurement strategy

Three basic sets have been analysed (see Figure 5), together with all their combinations, and the compensation error and the measurement time have been considered for a fair comparison.

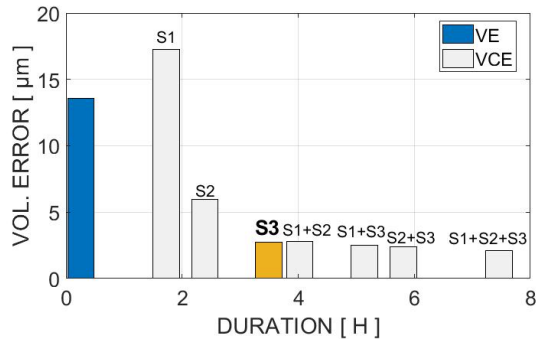


Figure 9. VE and VCE in function of the artefact position set and time. Selected optimal strategy S3 is highlighted.

These results are not so predictable and show how the procedure proposed in this work can help in finding the best result between several, in principle, reasonable approaches, with large differences in measurement time and in the compensation error. S3 could be considered here as an optimal approach.

## 6 Conclusions

An optimization procedure for artefact-based error mapping processes for a large 3 axis machines has been presented. The procedure allows the optimization of the error mapping procedure, considering aspects such as the design of the artefact, or the positions in the workspace where it is measured.

The procedure has been applied on a large milling machine tool, and some analyses have been performed. The relevance of performing such analysis to ensure that error mapping uncertainty and machine occupation time are optimized has been demonstrated. The obtained criteria are valid for the machine that has been simulated, and the analysis should be performed whenever a new machine is addressed, since the optimal procedure will always depend on the characteristics of the machine and the requirements of the application. With these considerations in mind, some conclusions can be drawn from the performed analysis.

The shape of the artefact, represented here as a misalignment of the balls, helps in reducing mapping uncertainty when a reduced number of measurements is performed.

The optimal number of balls in the artefact or the measurement strategy will depend on the expected uncertainty and available measurement time. Sufficiently good estimations for fast machine verification can be obtained in reduced measurement sets.

## References

- [1] McKeown PA, Loxham J. Some aspects of the design of high precision measuring machines. *CIRP Annals* 1973;22.
- [2] Sartori S, Zhang GX. Geometric Error Measurement and Compensation of Machines. *CIRP Annals - Manufacturing Technology* 1995;44:599–609.
- [3] Aguirre G, Iñigo B, Cilla J, Urreta H. Optimal design of artefacts for machine tool calibration. *Euspen 19th International Conference* 2019.
- [4] Lamikiz A, López de Lacalle LN, Ocerin O, Díez D, Maidagan E. The Denavit and Hartenberg approach applied to evaluate the consequences in the tool tip position of geometrical errors in five-axis milling centres. *Int J Adv Manuf Technol* 2008;37:122–39.
- [5] Ibaraki S, Hiruya M. Assessment of non-rigid body, direction- and velocity-dependent error motions and their cross-talk by two-dimensional digital scale measurements at multiple positions. *Precision Engineering* 2020;66:144–53.
- [6] Iñigo B, Colinas-Armijo N, Lopez de la Calle LN, Aguirre G. Ambient temperature effect on the volumetric error of a large milling machine. *Euspen Thermal Issues* n.d.
- [7] Haitjema H. Straightness, flatness and cylindricity characterization using discrete Legendre polynomials. *CIRP Annals* 2020;69:457–60.
- [8] Schwenke H, Knapp W, Haitjema H, Weckenmann A, Schmitt R, Delbressine F. Geometric error measurement and compensation of machines—An update. *CIRP Annals - Manufacturing Technology* 2008;57:660–75.

## **Background noise assessment of low-cost vibration sensors in precision manufacturing applications**

A. Iqbal, N. S. Mian, A. P. Longstaff, S. Fletcher  
*Centre for Precision Technologies, University of Huddersfield,  
Queensgate, Huddersfield HD1 3DH, United Kingdom  
Email: ali.iqbal@hud.ac.uk*

### **Abstract**

Accurate, reliable, and consistent vibration measurements in manufacturing machines such as machine tools, form the basis for predictive maintenance and condition monitoring applications. Recent advancements in Micro Electro-Mechanical Systems (MEMS) has led to a rapid adoption of low-cost industrial grade MEMS vibration sensors in contrast to traditional high-cost Integrated Electronics Piezo-Electric (IEPE) accelerometers which have been typically used in precision manufacturing setups. However, low-cost MEMS accelerometers are subject to various deterministic and stochastic noise phenomenon which often limits their performance especially when subject to low acceleration conditions. Preliminary work has been performed for characterization of baseline errors and uncertainties of such low-cost triaxial vibration sensors to evaluate their viability in metrological applications for Industry 4.0. However, employment of low-cost MEMS sensors for long term vibration measurements requires assessment and quantification of time dependent progression of the noise and its effect. Methods such as Allan Variance which are based on regression analysis of entire time-domain sensor data provide effective modelling and systematic assessment of background noise in MEMS based sensors in accordance with IEEE 1293-2018 standard.

To evaluate the background noise in these low-cost industrial MEMS sensors, continuous long-term data was recorded on a vibrationally stable test bed while establishing traceability according to the ISO 16063-11:1999 and ISO 16063-21:2003 standards. Linear accelerometer analysis was conducted to quantify and characterize various types of noise and random effects contributing to the sensor measurements while ensuring input to the setup is lower than intrinsic noise of the sensors. This work attempts to model noise parameters of low-cost MEMS vibration sensors to mitigate the baseline errors and random noise for employment

in industrial manufacturing setups and smart condition monitoring applications. Results from this study will offer an improved framework for sensor stability through obtaining a low noise floor by a careful consideration of underlying random processes within metrology applications.

## **1 Introduction**

Accurate, reliable, and consistent vibration measurements in manufacturing such as machine tools, form the basis for predictive maintenance and condition monitoring applications [1]. The rise of accelerometer sensors based on Micro Electro-Mechanical Systems (MEMS) technology have already found appreciation in wide area of vibration sensing setups e.g. building structures, remote power setups, smart cities etc [2] due to their lower cost, improved accuracy and digitalization aspects. This has led to a rapid adoption of such low-cost industrial grade MEMS vibration sensors, in contrast to the traditional high cost Integrated Electronics Piezo-Electric (IEPE) accelerometers which have been typically used in precision manufacturing setups [3]. Applications such as machine tool prognostics, smart machining and precision engineering often require low amplitude vibration measurements at low range of frequencies [4]. High sensitivity requirements in various applications of the vibration sensors not only involves estimating the optimum placement of sensors where attenuation to vibration is minimal but also choice of sensors with extremely low noise floor.

However, noise is ubiquitous to such low-cost MEMS sensors and form the source of significant errors in applications where measurement of vibrations with low amplitude and frequency is important. Subsequently, these errors can become more significant if they are progressive over long-term. Therefore, the employment of low-cost MEMS sensors for long term vibration measurements requires assessment and quantification of time dependent progression of the noise and its effect. The issue of noise also necessitates the characterization and modelling of noise-based error models to fulfil need for the required tolerances and accuracy in industrial applications, with the ultimate goal of denoising of sensor measurements [5]. The noise in MEMS vibration sensors consist of both deterministic and stochastic parts [6]. The deterministic errors are often contributed by constant bias (sensor offset), scaling errors, non-linearity and cross axis sensitivity which can be quantified via calibration techniques through establishing traceability [1]. While the stochastic part of the errors in such sensors is due to random phenomenon, the elimination of which, is challenging and requires rigorous modelling and quantification through stochastic techniques.

Several variance-based techniques have been devised for stochastic estimation of sensors noise e.g., Power Spectral Density (PSD), Autocorrelation Function (ACF), Kalman filtering, Allan Variance (AVAR) etc [7]. Out of the various methods Allan Variance which is based on regression analysis of entire time-domain sensor data provides simple and effective modelling technique through a systematic assessment of background noise in MEMS sensors [8]. Preliminary work has been performed for characterization of baseline errors and uncertainties of such low-cost triaxial vibration sensors to evaluate their viability in

metrological applications for Industry 4.0 [3]. This paper progresses to the next step and evaluates the background noise in these low-cost industrial MEMS sensors through implementation of Allan Variance method on measured static long term vibration data.

## **2 Background Noise Estimation**

Noise is an ever-expanding area in engineering that poses practical problems and warrants further research. Noise can include both unavoidable intrinsic noises contributing to the system and noise of extrinsic nature due to operating conditions. Like all sensors and instruments the role of noise in MEMS has two important aspects, first is the sources which contribute to noise and secondly the practical limitations that result due to it [9]. It is a significant fact that noise limits the performance and degrades the measurements of many sensors systems. However, due to the design and size MEMS based accelerometers such noise problems can be acute especially at low values of input, thereby limiting the performance of systems, especially when operating under low acceleration conditions [9]. This accentuates the need for investigation of noise in precision manufacturing setups where the application requires to maintain tight tolerances. The current work focuses on identifying and modelling the background noise in MEMS vibration sensors. While a non-exhaustive list of the noise errors for MEMS can be drawn, this work would focus on the fundamental noise sources intrinsic to MEMS sensors as they can be the limiting factor for device performance in metrological applications.

### **2.1 Common types of noise in MEMS accelerometers**

The most relevant noise errors encountered in MEMS that are being considered for evaluation as part of the work are presented below, with brief description.

#### **2.1.1 Quantization**

It is the noise caused due to Analog to Digital conversion (ADC) errors and relates to resolution of the sensor. With a greater resolution of ADC, the noise due to quantization would be smaller.

#### **2.1.2 Velocity Random Walk (VRW)**

VRW measures the error resulting after integrating accelerometer to get velocity measurements caused by white noise in the sensors.

#### **2.1.3 Bias Instability (BI)**

The source of BI is the electronics components susceptible to random flickering, which manifests as a bias over time. It also called flicker, pink or  $1/f$  noise.

#### **2.1.4 Sinusoidal Noise**

The source of this noise is attributable to periodic environmental changes in the sensor measurements.

#### **2.1.5 Rate Random Walk (RRW)**

Rate random walk appears in acceleration measurements as a random drift rate

#### **2.1.6 Rate Ramp (RR)**

The source of this error is a linear long-term increase of the sensor's rate signal output. In contrast with others, it becomes deterministic in nature over time.

By now it is clear in many sensors that the nature of underlying noise is often unknown. In fact, several different noise sources may contribute simultaneously to corrupt the sensor signals. While, if correctly mathematically modelled tools such as auto-correlation function (ACF) and power spectral density (PSD) estimation can be used but if the noise errors are stochastic or random in nature, these methods do not suffice to characterize the underlying noise. In the next section, an effective method known as Allan variance (AVAR) sensor noise characterization will be introduced and discussed through developing its relationship with the noise terms identified earlier [10].

## 2.2 Allan Variance (AVAR) Method

Allan variance is a time-domain estimation of noise sources through linear accelerometer analysis. The resulting values characterize the noise by quantifying the spread in measurement values (or noise) across various time scales. Therefore, in simple terms the method offers an intuitive understanding of the evolution of noisy sensor signal over time. In general, the Allan variance,  $\sigma_a^2(\tau)$ , of a continuous time signal,  $\Omega(t)$ , is a function of a quantity called averaging time,  $\tau$ , and is given by the following:

$$\sigma_a^2(\tau) = \frac{1}{2(N-2n)} \sum_{k=1}^{N-2n} [\bar{\Omega}_{k+1}(\tau) - \bar{\Omega}_k(\tau)]^2 \quad \text{where } n = \frac{\tau}{\Delta t}$$

Where,  $N$  is the total number of samples in the discretized signal,  $\Delta t$  is the sampling period and  $\bar{\Omega}_k(\tau)$  can be shown as:

$$\bar{\Omega}_k(\tau) = \frac{1}{\tau} \int_{t_k}^{t_k+\tau} \Omega(t) dt, \Delta t \leq \tau \leq N\Delta t/2$$

Essentially, the results are obtained by dividing the sampled signals into clusters,  $\bar{\Omega}_k(\tau)$ , averaging over a duration,  $\tau$ , and computing the variances among groups as a function of varying  $\tau$  in a “non-overlapping” manner, since the clusters  $\bar{\Omega}_k(\tau)$  do not overlap across time.

The different types of random processes can be examined by investigating the Allan variance plot. The Allan variance provides a means of identifying various noise terms that exist in the data as they appear in different regions of  $T$ . A typical Allan variance plot looks like that shown in Figure 1 [11]

This property permits easy identification of various random processes that exist in the data. A summary of various noise sources in their relationship with the AVAR plot can be seen in Table 1. If it can be assumed that the existing random processes are all statistically independent, then it can be shown that the Allan variance at any given  $\tau$  is the sum of Allan variances due to the individual random processes at the same  $\tau$ . This can be modelled mathematically as: -

$$\sigma_a^2(\tau) = \sigma_q^2(\tau) + \sigma_{rw}^2(\tau) + \sigma_{bi}^2(\tau) + \sigma_{rrw}^2(\tau) + \sigma_{rr}^2(\tau) + \dots$$

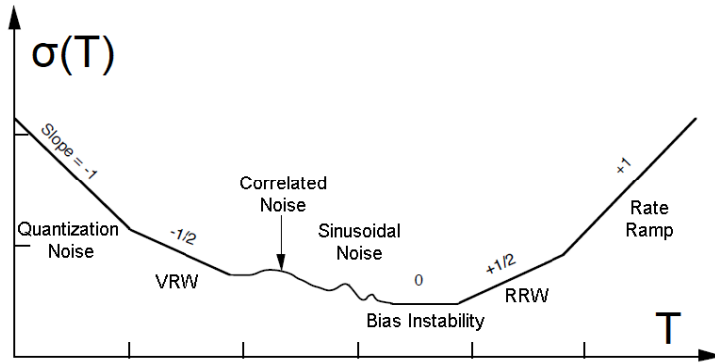


Figure 1 : Typical AVAR plot for MEMS sensors

Table 1: Summary of AVAR slopes for common noise processes [12]

Noise Source	Symbol	Slope (k)	Coefficient Units
Quantization	$\sigma_q$	-1	(m/s <sup>2</sup> )
Velocity Random Walk (VRW)	$\sigma_{rw}$	-1/2	(m/s/ $\sqrt{s}$ )
Bias Instability (BI)	$\sigma_{bi}$	0	(m/s <sup>2</sup> )
Acceleration Rate Random Walk (RRW)	$\sigma_{rrw}$	1/2	(m/s <sup>2</sup> / $\sqrt{s}$ )
Rate Ramp (RR)	$\sigma_{rr}$	1	(m/s <sup>2</sup> /s)

### 3 Methodology

A simple scenario to estimate the sensor self-noise is modelling noise parameters when the input to the sensor is lower than the intrinsic noise. This can be observed by taking measurements on a location where the level of vibration is low and unaffected by background noise factors [13]. Another aspect to be ensured before data collection is to minimize the temperature variation as it can affect the stochastic characteristics of noise parameters to be estimated in low-cost MEMS sensors [14]. The background noise estimation and characterization tests for low-cost accelerometers was conducted by establishing traceability of the setup according to the ISO 16063-21 [15] and ISO 16063-11 [16] standards. These standards provide guidelines for calibration of vibration sensors by comparing their results to a reference transducer and laser interferometry. In this work, the methodology for noise characterization for MEMS based sensors was derived according to the IEEE-STD-1293-2018 [11] which identifies PSD and Allan Variance (AVAR) as key methods for the analysis of noise. However, the current work focuses solely on AVAR as an established technique for time domain analysis to model underlying random processes that give rise to the data noise in accordance with IEEE-STD-952-1997 [12] standard.

For the practical implementation of Allan Variance method to characterize different types and magnitudes of noise error terms in low-cost industrial MEMS

sensors, a continuous long-term static test was conducted based on the aforementioned standards. The test was performed in a vibration-isolated and temperature-controlled environment for the duration of 60 hours. A detailed experimental setup and choice of sensors is explained in the next section.

### 3.1 Experimental Setup

An industrial grade tri-axial digital MEMS sensor (ADXL355) [17] was selected as a low-cost vibration sensor for modelling the noise parameters. While other MEMS sensors are available in the market at a lower price point [2], this (ADXL355) sensor provided high resolution (20-bit) on chip ADC along with required sensitivity for low amplitude measurements. The sensor also boasts ultralow noise features that may be expected from traditional accelerometers while with the added capability of providing the digital communication options (I2C/SPI) for convenient and configurable data acquisition modes. Key specifications for ADXL355 MEMS sensor are shown in Table 2. A tri-axial IEPE accelerometer (PCB 356A02) [18] was employed as a reference transducer in the experiment. A Renishaw XL-80 laser interferometer [19] was used as traceable reference in acceleration measurement mode for benchmarking the vibrational stability of the setup. The sensors were mounted on a 5 mm aluminium plate and secured using bolts, while the sensor cables were secured using adhesive clamps minimizing transmission of unwanted vibrations to the experimental setup. Digital temperature sensors (Maxim DS18B20) [20] were installed on the sensor plate and at a distance of 25 cm as part of the setup to record sensor and environmental temperature variations respectively ,for the entire duration of test. The setup can be seen in Figure 2.

Table 2: Key specifications ADXL-355 Digital MEMS [17]

S No	Parameter	Specification value
1	Measurement Range	$\pm 2.048$ g
2	Sensitivity	256000 LSB/g
3	Non-linearity	$\pm 0.1$ %
3	Axes	Tri-axial
4	Temperature Range	-40 to +125 °C
5	Transverse Sensitivity	$\leq 1$ %
6	Temperature Response	$\pm 0.01$ %/°C

The Data Acquisition Systems (DAQs) for the sensors (MEMS, IEPE and Laser) recorded individual sensor data to a PC. The DAQ of MEMS sensor was based on a Raspberry Pi 3 Model A+ and transmitted data wirelessly to the PC via the I2C protocol. Benchmarking of setup via a Laser was conducted through use of Renishaw’s propriety QuickViewXL software while data acquisition for the IEPE accelerometer was based on the National Instrument (NI) DAQ. To ensure synchronisation of timings across sensors, a shock impact event was created on the CMM bed using a hammer, the rising edge of the impact vibration acted as a trigger point for long term data recording.

In order to characterize and model the noise parameters of the low-cost MEMS sensor, the choice of installation in a vibration-isolated environment is key. Therefore, the test was conducted in a temperature-controlled environment of  $\pm 1\text{ }^{\circ}\text{C}$  on a vibration-isolated stable granite Coordinate Measuring Machine (CMM). Moreover, to ensure a minimal effect of micro-vibrations induced in the sensor from external sources such as floor vibrations, opening and closing of doors, movement of people etc. the test was conducted over the span of a weekend.

The choice of nominal range and sampling rate for sensors is an important and critical aspect within the application of AVAR method. The nominal range of the MEMS sensor was configured as  $\pm 2\text{ g}$  (where  $g=9.81\text{ m/s}^2$ ) to ensure a high sensitivity of operation, while the IEPE sensor was operated in its nominal operating range of  $\pm 500\text{ g}$  to record any high amplitude event that might not be recorded by MEMS sensor due to sensing overload. It is important to point out that MEMS sensor in its  $\pm 2\text{ g}$  configuration, has a very high resolution of  $3.906\text{ }\mu\text{g/LSB}$ , fulfilling a key requirement of modelling underlying noise processes. A sampling rate of approximately  $100\text{ Hz}$ . was chosen for the MEMS sensor while the IEPE sensor sampled the data at higher rate of  $1650\text{ Hz}$  to serve as a reference for any high frequency event in the data which might appear as an outlier in MEMS data. The impact of sensor range and sampling rate on noise analysis for sensors is discussed in detail in the next section which focuses on background noise estimation using AVAR.

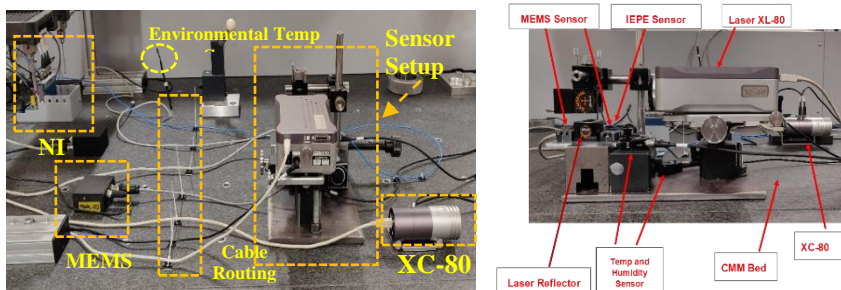
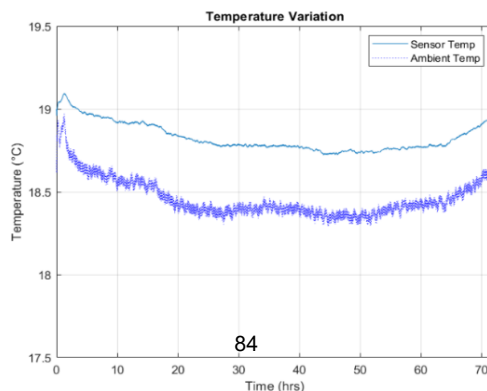


Figure 2 : Experimental Setup on CMM Bed (L) and Sensor Setup (R)

## 4 Results and Discussion

For an effective application of AVAR for modelling the sensor noise, measurements should be obtained in the absence of any input to the sensor, for which, the condition of 'zero excitation' was achieved by placing the sensor on a stable CMM granite bed. The vibrational stability of setup was benchmarked to



be  $\pm 0.316\mu\text{g}$  using a laser interferometer. The sensor was placed in a temperature-controlled room to avoid effects such as environmental induced bias in the characterization of process noise, this can be seen in the plot of temperature vs time in Figure 3.

Through applying AVAR method to the whole data set, a log–log plot of the Allan Variance versus the cluster time as shown in Figure 4 for the three axes of the MEMS accelerometer, was generated in MATLAB. Through the computational analysis of the slopes of the plot according to Table 1 and Figure 1, the various noise terms that were identified are summarized in Table 3, below.

Table 3: Summary of AVAR Results for the ADXL-355

Noise Source	X-Axis	Y-Axis	Z-Axis	Coefficient Units
Quantization	-	-	-	(m/s <sup>2</sup> )
Velocity Random Walk (VRW)	$1.7121 \times 10^{-5}$	$1.6685 \times 10^{-5}$	$2.6592 \times 10^{-4}$	(m/s/ $\sqrt{\text{s}}$ )
Bias Instability (BI)	$3.2454 \times 10^{-5}$	$2.1983 \times 10^{-5}$	$7.4330 \times 10^{-5}$	(m/s <sup>2</sup> )
Acceleration Rate Random Walk (RRW)	$2.1559 \times 10^{-5}$	-	$9.1834 \times 10^{-5}$	(m/s <sup>2</sup> / $\sqrt{\text{s}}$ )
Rate Ramp (RR)	-	-	-	(m/s <sup>2</sup> /s)

It is evident from the plot that the Quantization noise does not exist in any of axes which could be attributed to the 20-bit ADC in MEMS, which provides high resolution. Similarly, the sensor seems not to be affected by RR noise as well. The results clearly indicate that VRW is the dominant error for the short cluster times ( $T < 10$  s), whereas BI is the dominant error for the long cluster times ( $T < 10000$  s).

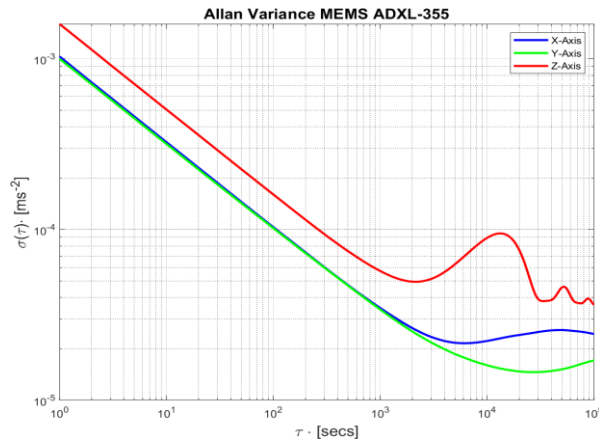


Figure 4 : Allan Variance Plot for MEMS

The X and Z axes of the MEMS seems to be affected by RRW, while the noise term is not detected in Y-axis of the sensor. Therefore, from the analysis of the results, that major noise contribution in MEMS sensor can be attributed to VRW and BI terms, in all the axis.

The estimation quality for computed results can be calculated based on the Allan Variance estimation error equation [12]. Estimation errors were found to be 0.05 % for short cluster times and 4.7 % for long cluster times. Therefore, the maximum uncertainty for computed results is in the order of 4.7 %.

## **5 Conclusion**

The work has characterized and quantified the noise parameters of a low-cost MEMS accelerometer for use in precision manufacturing applications. The work encompassed identifying different noise terms which can affect the accuracy of vibration measurements. Through long-term stable measurements from the sensor and application of Allan Variance method, the noise characteristics of the sensor were modelled. The results obtained from AVAR can be considered satisfactory with the maximum uncertainty for analysed noise parameters computed to be at 4.7 %. The sensor is not affected by quantization noise, rate ramp or sinusoidal noise in any of the axes. While RRW was only found in the X and Z axes of sensor. The major contribution of noise for sensor in all axes is due to VRW and BI noise terms. The results from the work, offer an improved framework for sensor stability for employment of MEMS based sensor in manufacturing and industrial applications.

Based on the quantifiable information computed from AVAR, several denoising techniques such as Kalman filtering, wavelet denoising based on Discrete Wavelet transform (DWT) etc. can potentially be used to improve signal characteristics and obtain low noise floors, as well. Future work can also focus on evaluating the frequency domain noise in such MEMS sensors using techniques such as power spectral density (PSD) as it has been shown to have a strong relationship with AVAR method [11].

## **Acknowledgements**

The authors gratefully acknowledge the UK's Engineering and Physical Sciences Research Council (EPSRC) funding of the Future Metrology Hub (Grant Ref: EP/P006930/1).

## **References**

- [1] M. Galetto *et al.*, "Uncertainty evaluation in calibration of low-cost digital MEMS accelerometers for advanced manufacturing applications," *CIRP Annals*, 2019.
- [2] A. Sabato *et al.*, "Wireless MEMS-Based Accelerometer Sensor Boards for Structural Vibration Monitoring: A Review," *IEEE Sensors Journal*, vol. **17**, no. 2, pp. 226-235, 2017.
- [3] A. Iqbal *et al.*, "Performance evaluation of low-cost vibration sensors in precision manufacturing applications," in *20th International Conference of the European Society for Precision Engineering and Nanotechnology*, 2020, pp. 535-538: euspen.
- [4] G. D'Emilia *et al.*, "Evaluation of aspects affecting measurement of three-axis accelerometers," *Measurement*, vol. **77**, pp. 95-104, 2016.

- [5] K. Jerath *et al.*, "Bridging the gap between sensor noise modeling and sensor characterization," *Measurement*, vol. **116**, pp. 350-366, 2018/02/01/ 2018.
- [6] P. Petkov *et al.*, "Stochastic modeling of MEMS inertial sensors," *Cybernetics and information technologies*, vol. **10**, no. 2, pp. 31-40, 2010.
- [7] M. Matejček *et al.*, "New experience with Allan variance: Noise analysis of accelerometers," in *2017 Communication and Information Technologies (KIT)*, 2017, pp. 1-4.
- [8] J. Jurado *et al.*, "A regression-based methodology to improve estimation of inertial sensor errors using Allan variance data," *Navigation*, vol. **66**, no. 1, pp. 251-263, 2019.
- [9] F. Mohd-Yasin *et al.*, "Topical Review: Noise in MEMS," *Measurement Science & Technology - MEAS SCI TECHNOL*, vol. **21**, 01/01 2010.
- [10] N. El-Sheimy *et al.*, "Analysis and modeling of inertial sensors using Allan variance," *IEEE Transactions on instrumentation and measurement*, vol. **57**, no. 1, pp. 140-149, 2007.
- [11] IEEE, *IEEE STD 1293-2018 (Revision of IEEE STD 1293-1998): IEEE Standard Specification Format Guide and Test Procedure for Linear Single-Axis, Nongyroscopic Accelerometers (IEEE STD 1293-2018)*. IEEE, 2019.
- [12] IEEE, "IEEE STD 952-1998 : IEEE standard specification format guide and test procedure for single-axis interferometric fiber optic gyros," 1998: Institute of Electrical and Electronics Engineers New York, NY.
- [13] R. Brincker *et al.*, "Obtaining and estimating low noise floors in vibration sensors," in *Proceedings of the 25th SEM International Modal Analysis Conference*, 2007.
- [14] M. El-Diasty *et al.*, "Temperature variation effects on stochastic characteristics for low-cost MEMS-based inertial sensor error," *Measurement Science and Technology*, vol. **18**, no. 11, pp. 3321-3328, 2007/09/20 2007.
- [15] B. ISO, "BS ISO 16063-21:2003: Methods for the calibration of vibration and shock transducers. Vibration calibration by comparison to a reference transducer," ed: British Standards Institute, 2003.
- [16] B. ISO, "BS ISO 16063-11:1999: Methods for the calibration of vibration and shock transducers. Primary vibration calibration by laser interferometry," ed: British Standards Institute, 2001.
- [17] A. Devices, "ADXL354/ADXL355 Low Noise, Low Drift, Low Power, 3-Axis MEMS Accelerometers Data Sheet (Rev. A)," 2018.
- [18] P. Piezotronics. (2019). *PCB 356A02 Tri-axial Accelerometer Data Sheet*.
- [19] Renishaw. (2019). *XL-80 Laser Measurement system*.
- [20] D. S. B. P. Resolution. (2018). *DS18B20 1-Wire Digital Thermometer, Data Sheet, Maxim Integrated Products*.

## **Session 4**

### **Additive Manufacturing and Standards**

# **Evaluation of the electron beam spot size in electron beam melting for additive manufacturing**

Z. Lin <sup>a</sup>, X. Zhao, S. Dadbakhsh, A. Rashid

*Production Engineering Department, KTH Royal Institute of Technology, Brinellvägen 68, Stockholm 11428, Sweden*

<sup>a</sup> *zeyul@kth.se*

## **Abstract**

Since electron beam (EB) is the main additive manufacturing (AM) tool in electron beam melting (EBM), EB spot size plays a significant role in the parts quality, surface roughness as well as the microstructure and corresponding properties. So far, the research on measuring EB spot size has been mainly based on printing with/without powder single tracks on a metal plate such as stainless steel. However, this method, due to material thermal properties as well as the melting phenomena, cannot reveal the actual value for the EB spot size. This research is carried out to establish a simple methodology on measuring the EB spot size in a more accurate way at a low cost. To do so, a ceramic surface coating was applied to the surface of a copper starting plate and a stainless steel starting plate respectively. Afterwards, the EB applied the tracks onto the coated starting plate and regular metal starting plate. The analysis showed that the EB tracks on ceramic coated stainless steel plates could be the best replica for the electron beam among those materials tested in this work.

## **1 Introduction**

In comparison to other powder-bed metallic AM processes, EBM offers improved advantages in the build rate, material purity and reduced thermal distortion [1]. As the monopolistic heat source during the entire process, electron beam (EB) plays a main role in determining the stability and the quality of the final product. One important factor demonstrating the EB quality is the corresponding EB spot diameter, which altered via a parameter called focus

offset in a typical EBM machine. This parameter is in fact the current value used for regulating the focusing coils to adjust the concentration of the EB, affecting the EB spot size and the melt pool geometry [2]. This parameter is critical since it influences the input energy intensity and hence the formation of defects, such as porosity, cracking, balling and delamination, as well as the material microstructures [3][4]. In this study, a simple and low cost method has been studied to measure the EB spot size more accurately. This has been practiced via analysing the EB tracks on the coated metal plates with a thin layer of an insulating ceramic.

## 2 Material and Experiment Setup

In order to measure the EB size, EB was radiated to ground and polished 316L stainless steel and Cu-DHP plates with 150 mm×150 mm cross section. The thickness of the stainless steel plate and copper plate was 10 mm and 6 mm respectively. After that, a ceramic coating layer by ‘ESAB jig and tool protector ceramic coating’ was sprayed to the base plate which can resist to heat up to 1300°C [5]. For the levelling purposes, each plate was laid on a stack of IN718 powder bed which had the thickness of 20 mm.

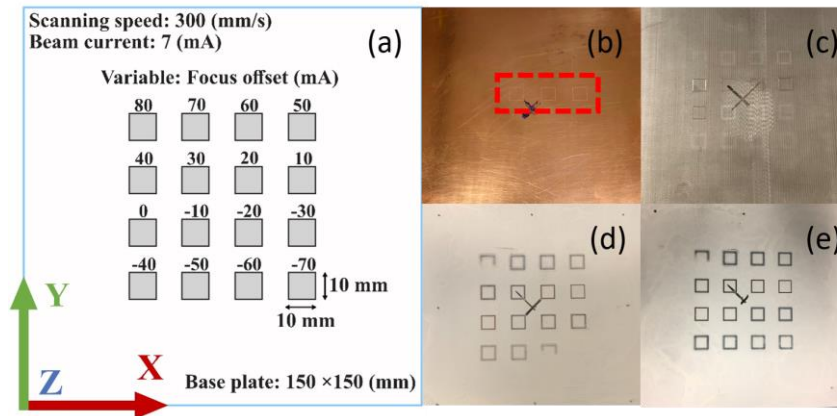


Figure 1. (a) Printing squares model layout and process parameter settings; Surface marking after the EB scanning (b) copper plate; (c) stainless steel plate; (d) copper plate with coating; (e) stainless steel plate with coating

An Arcam A2X EBM system (GE additive, Sweden) was used to perform the experiment. The EB tracks were applied at room temperature with various focus offsets, ranging from 80mA to -70 mA. (Figure 1). Four types of base plate were used, i) copper (Figure 1b), ii) ceramic coated copper (Figure 1d), iii) stainless steel (Figure 1c) and iv) ceramic coated stainless steel (Figure 1e). In each case, a single contour square track with 10 mm length was made for 16 squares with various focus offsets. For all the squares, the scanning speed is 300 mm/s and the beam current is 7 mA. After creating EB tracks, each of the base plate was measured by a zygo NewView™ 7300 white light

interferometer (Lambda Photometrics, UK&Ireland) and Nikon SMZ800 optical microscopy (Nikon metrology, USA). The surface profile measurement of the stainless steel and copper plate have been taken with WLI using 2.5X magnification. As shown in Figure 2, through the visualization and extraction of the surface profile function in mountains8™ software, the EB re-consolidated geometry has been defined and analyzed for each square tracks with different focus offsets.

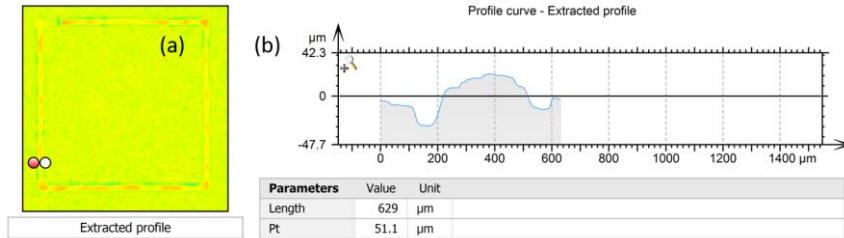


Figure 2. Stainless steel plate surface profile measurement from WLI when focus offset at 10 mA, a) Profile extraction; b) Profile extraction analysis

In addition, Figure 3 shows the example of data acquisition method applied by optical microscopy. Six points on each side has been selected and the dimension of the main EB track and also the EB affected zone have been measured by optical microscopy using both 1X and 10X magnification.

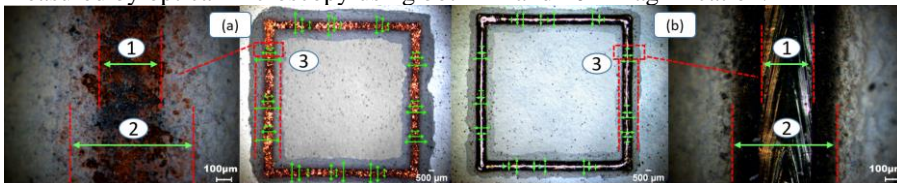


Figure 3. (1) Peak track width (PTW), (2) scanning track width (STW), and (3) full track width (FRW) viewed using optical microscopy in 1X and 10X magnification for (a) ceramic coated copper plate; and (b) ceramic coated stainless steel plate at focus offset of 10 mA

### 3 Results and Conclusion

From Figure 1, there are only three squares visible on the copper plate being marked at the focus offset of 30 mA, 20 mA and 10mA which are located inside of the red dash line box. In comparison to the copper plate, almost all squares are visible for the naked eyes on the stainless steel plates, though their visibility could be so low that might not be detectable under optical microscopy. In contrast to regular plates, for the coated copper and coated stainless steel, all the squares are very clear except the last mark on the coated copper plate which is missing. The lowest number of visible tracks on copper demonstrates the minimum sensitivity of the copper plate to replicate the physical form of an EB. This can be attributed to the higher thermal conductivity of copper, being about

25 times more than stainless steel, dissipating the EB energy quickly. In contrast, all the tracks are well visible on the ceramic coated stainless steel, demonstrating the maximum sensitivity of this material to detect EB.

Results of the measurement from WLI is based on the EB tracks on the copper and stainless steel plate. Thus, the dimension of the EB path width is mainly based on the melting pool size. As shown in Figure 2, the re-consolidated melt pool geometry has a near gaussian distribution shape. Due to surface tension, there are also valleys located between the base plate and the peak track on both side which is the result of introducing the solid to the melt pool.

There are three different level of tracks observed in Figure 3 for tested materials. Peak track width (PTW), which had nearly all the ceramic coating evaporated, seems to be the result of the exposure to the highest level of energy intensity. In comparison, scanning track width (STW), with blackened ceramic coating appears to originate from exposure to lower level of energy intensity. At last, full track width (FTW), which cover the full scanning width has the minimum EB energy intensity.

The conclusion for this study can be given as:

- EB radiation effects varies with respect to the base material properties, mainly due to the thermal conductivity
- The EB tracks on the ceramic coated stainless steel could lead to the best replication to represent the EB profile in comparison with the tracks on other materials tested in this work

## References

- [1] X. Ding, Y. Koizumi, D. Wei, and A. Chiba, "Effect of process parameters on melt pool geometry and microstructure development for electron beam melting of IN718: A systematic single bead analysis study," *Addit. Manuf.*, vol. 26, no. September 2018, pp. 215–226, 2019.
- [2] P. Karimi, E. Sadeghi, J. Ålgårdh, and J. Andersson, "EBM-manufactured single tracks of Alloy 718: Influence of energy input and focus offset on geometrical and microstructural characteristics," *Mater. Charact.*, vol. 148, no. November 2018, pp. 88–99, 2019.
- [3] S. P. Narra, "Melt Pool Geometry and Microstructure Control Across Alloys in Metal Based Additive Manufacturing Processes," *Dissertations*, 2017.
- [4] P. Karimi, *Electron beam-powder fusion of Alloy 718: Effect of process parameters on Microstructure evolution*, ISBN 978-9., no. 1. 2020.
- [5] "ESAB Jig and Tool protection." [Online]. Available: <https://www.esab.it/it/en/products/ppa-accessories/accessories/esab-jig-and-tool-protection.cfm>. [Accessed: 02-Jan-2021].

## **Session 5**

### **Associated Measurement**

# **Optical 3D measurement of cooling holes in gas turbine and aircraft engines**

K. Zangl, R. Danzl, D. Urlep, F. Helmli  
*Bruker Alicona, Austria*

## **Abstract**

The quality control of cooling holes is an important topic for increasing the efficiency and ensuring the safety in high-performance systems. Even if heat-resistant materials are used (Inconel steels), the surface must be cooled because the surrounding gases are in the range of the melting point. This is done with compressed air from the inside of the blade. The position, orientation and shape of the holes thus play a major role in the safety of the turbine. These turbine blades are used in aircraft turbines and gas turbines.

Currently, the geometry is measured using computer tomography or fiber probes. The proposed method (vertical focus probing) offers advantages in terms of measurement time, resolution, non-contact measurement and the possibility to measure deep into the hole. We demonstrate the strength of vertical focus probing for cooling hole measurement by several results of highly accurate 3D measurements of differently shaped holes as well as their geometric inspection.

## **1 Introduction**

Cooling holes have an important functionality to avoid the overheating of turbine blades. By blowing cooling air through these holes, a thin insulating layer is generated between the combustion gases and the blade. In addition to other measurement tasks as e.g. the break edge measurement, the geometric verification of cooling holes is a challenging task in 3D metrology on aerospace parts. The difficulty in the 3D measurement of these holes is based on several aspects. On the one hand, one turbine blade may consist of many differently shaped cooling holes with different sizes, angles, and positions which must fulfil their nominal values in tight tolerances. On the other hand, the measurement of such cooling holes is complicated by their difficult accessibility for measurement (see Figure 1 left for a typical blade including measurement directions for some holes).

There are some approaches to automatically measure micro holes in general and cooling holes in particular including computer tomography, using fiber probes or fringe projection [3, 4, 6]. These methods are either limited by their resolution, their ability to measure deep into the hole, long measurement time or their contact-based measurement where accessibility is based on the probe size and the blade can be damaged.

In this paper, the automatic, repeatable and traceable 3D measurement of different kinds of cooling holes by vertical focus probing (VFP) is presented, which is an extension of focus variation (FV), but enabling the measurement of vertical structure with slope angles  $\geq 90^\circ$ .

## 2 Measurement and results

### 2.1 Measurement principle

For the application, vertical focus probing was used [5]. VFP is an optical measurement principle which measures vertical walls and holes with a slope angle  $\geq 90^\circ$  by focus variation (see also [1, 2]). Typically, FV uses the small depth of focus of an optical system to provide topographical information. Thereby, exactly one z value is measured for each x, y position by vertical scanning and analysis of the focus information along the vertical axis, whereas the measurement of vertical  $90^\circ$  structures is not possible at all. VFP extends this principle by measuring many z values for each position through which vertical structures as holes can be measured. VFP exploits the reflective properties of the surfaces where depending on the type and position of the illumination, the geometry of the sample and the roughness properties of the surfaces always a part of light is reflected to the objective (see Figure 1 right).

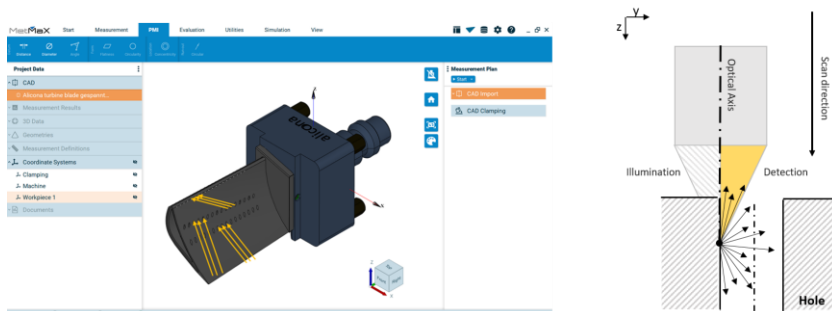


Figure 1: Left: Turbine blade with different kinds of holes. Yellow arrows show typical measurement directions which are parallel to the hole axis using VFP. Right: VFP measurement principle.

### 2.2 Experimental setup

In this paper, a Bruker Alicona  $\mu$ CMM was used for the measurements (see Figure 2a). The measuring instrument has an optical sensor based on focus variation and a measuring volume of 310x310x310 mm [7]. For this application

the measuring instrument was equipped with an automatic tilt and rotation axis and a 5x magnification objective lens.

Since turbine blades including computer-aided design (CAD) data are confidential in most cases, a cooling hole artefact (see Figure 2b and c) was constructed and manufactured. The artefact is a metal plate which consists of differently shaped cooling holes with diameters from 350  $\mu\text{m}$  to 1.6 mm.

For the measurement, the artefact is clamped into a rotation unit to ensure different measurement directions dependent on the hole geometry, position, and orientation. To measure all holes on a turbine blade different measurement directions are needed, as the optical axis of the system is aligned parallel to the hole axis during a vertical focus probing measurement (see Figure 1). For the geometric verification only relevant measuring positions are measured, and those measurements are precisely set in relation to each other. The relevant measurement position can be easily defined by the instrument's software which allows to define them directly on the CAD data, and the software automatically determines the measurement principle, either FV or VFP, as well as the needed measurement directions. A prerequisite for such an automatic measurement is, that the virtual and the real instrument is exactly aligned. Additionally, a rotation- and tilt unit calibration was performed to adjust the unit exactly with respect to the measurement system.

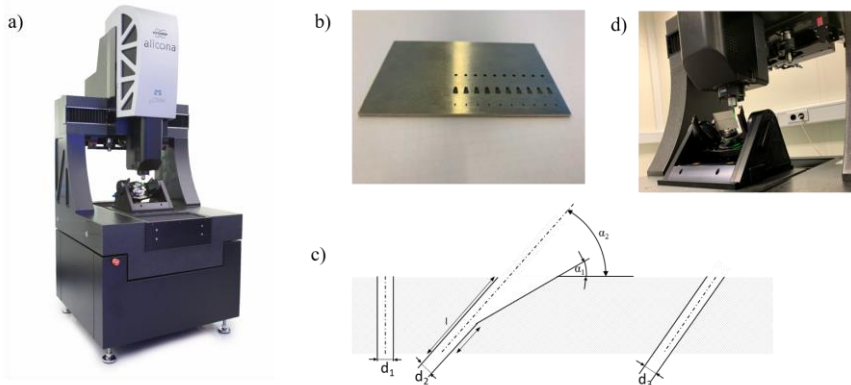


Figure 2: a) Bruker Alicona  $\mu\text{CMM}$ . b) Measurement artefact. c) Schematic cross section of the plate. d) Experimental setup.

### 2.3 Measurement results

Several measurements were performed on the measurement artefact. In Figure 3a, a 3D measurement of a fan-shaped hole is shown. The 3D dataset consists of a FV measurement of the top surface including colour information and a VFP measurement of the cooling hole without colour information which were fused together to one 3D dataset. The hole was measured into a depth of around 3 mm and minimum diameter of 360  $\mu\text{m}$  at the bottom. As these results demonstrate, holes with a diameter:depth ratio up to 1:10 depending on the used objective

lens, the lighting conditions, and the hole geometry can be measured. In Figure 4a, a 3D dataset of a multi-measurement is shown. In each line of the measurement artefact four holes were measured and the single measurements were fused together to one dataset. Thus, each hole geometry (see Figure 2c) was measured four times. Again, each hole measurement of this dataset consists of a top surface measurement using FV, and a VFP measurement of the hole. It can clearly be seen that the orientations and shapes of the holes differ significantly. In Figure 4b, an exemplary geometric verification of a cooling hole is shown. In addition to the orientation, the diameter was verified at three different positions along the hole.

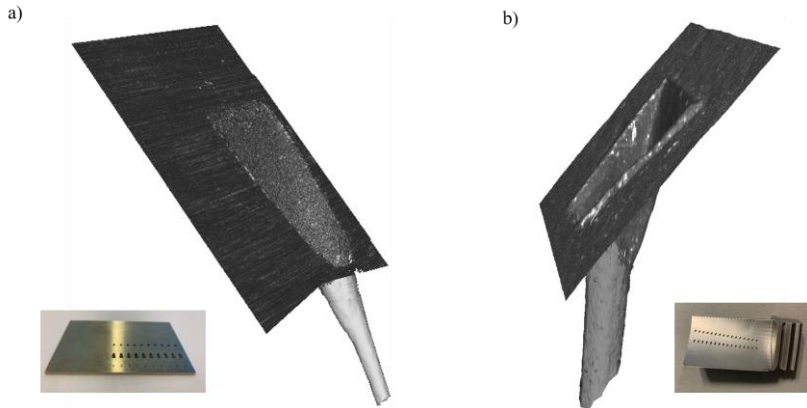


Figure 3: 3D measurements of cooling holes by FV and VFP. The FV measurement of the top surface is fused with the VFP measurement of the hole. a) Cooling hole of the measurement artefact. b) Cooling hole of a turbine blade.

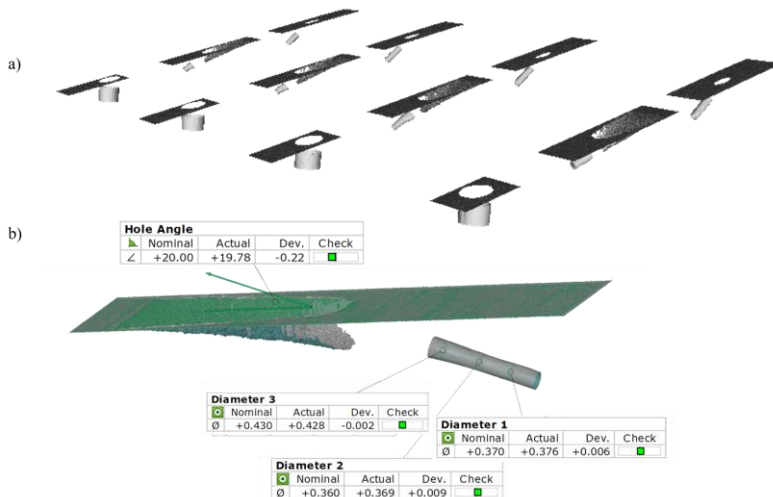


Figure 4: a) Multi-measurement on the plate. b) Geometric verification exemplarily for a fan-shaped cooling hole.

### **3 Conclusion and discussion**

The results show the strength and the high potential of vertical focus probing for high-precision 3D measurements of cooling holes on turbine blades. The main benefits of the proposed measurement principle are the optical and non-destructive data acquisition of holes with a high diameter:depth ratio in combination with a highly accurate multi-measurement procedure which allows the measurement of cooling holes on turbine blades in an automatic, traceable and repeatable manner. Influence factors that need to be considered for VFP are the illumination conditions, the geometry of the measured hole as well as the surface texture properties, as these factors determine how much light is reflected to the lens. A quantification of the VFP performance can be found in [5], whereas the quantification on cooling hole is ongoing work. Current activities include the further evaluation of the measurement principle on different kinds of real turbine blades (see Figure 1 left and Figure 3b for a first measurement). Further research will focus on the further development of vertical focus probing with respect to measurable geometries, so that VFP can be used in a fast and robust manner for different types of cooling holes including those that do not always have a circular geometry inside the hole.

### **References**

- [1] R. Danzl F. Helmli, S. Scherer, *Focus variation—a robust technology for high resolution optical 3D surface metrology*, 2011, J. Mech. Eng.
- [2] F. Helmli, *Focus variation instruments* in *Optical Measurement of Surface topography* edited by R. K. Leach, 2011, Springer, Berlin
- [3] C. Munkelt, P. Kühmstedt, L. Aschermann, F. Seidel, *Automatic complete high-precision optical 3D measurement of air cooling-holes of gas turbine vanes for repair*, 2015, Proc. of SPIE Vol. 9525
- [4] B. Muralikrishnan, J.A. Stone, J.R. Stoup, *Fiber deflection probe for small hole metrology*, 2006, Precision Engineering
- [5] C. Repitsch, K. Zangl, F. Helmli, R. Danzl, *Focus variation* in *Advances in Optical Surface Texture Metrology* edited by R. K. Leach, 2020, IOP Publishing, Bristol UK
- [6] G. Robinson, *Measurement of Cooling Holes in Gas Turbine Blades using Computer Tomography*, Survice Engineering Company, online: [https://www.cmsc.org/stuff/contentmgr/files/0/2bdcf766d9d5daf6e892c46153c591d3/misc/cmsc2011\\_wed\\_gh\\_0800\\_survice.pdf](https://www.cmsc.org/stuff/contentmgr/files/0/2bdcf766d9d5daf6e892c46153c591d3/misc/cmsc2011_wed_gh_0800_survice.pdf)
- [7] K. Zangl, R. Danzl, F. Helmli, M. Prantl, *Highly accurate optical  $\mu$ CMM for measurement of micro holes*, 2018, Proc. CIRP

# **Novel signal processing module of Fabry-Perot interferometer**

Syuan-Cheng Chang<sup>1\*</sup>, Yung-Cheng Wang<sup>1</sup>, Chung-Ping Chang<sup>2</sup>,  
Teng-Chi Wu<sup>1</sup>, Bean-Yin Lee<sup>3</sup>

<sup>1</sup> *Department of Mechanical Engineering, National Yunlin University of Science and Technology, Yunlin 640, Taiwan*

<sup>2</sup> *Department of Mechanical and Energy Engineering, National Chiayi University, Chiayi 600, Taiwan*

<sup>3</sup> *Department of Mechanical and Computer-Aided Engineering, National Formosa University, Yunlin 632, Taiwan*

[\\*tso1147279@gmail.com](mailto:tso1147279@gmail.com)

## **Abstract**

In this investigation based on the self-developed folded Fabry-Perot interferometer, a novel signal processing module is optimized and integrated with others units. In order to acquire refined interferometric signals, the previous piezo transducer (PT) modulation mechanism is modified to improve the signal stability without complex adjustments or arrangements. With the aid of the improved signal processing module, the experimental results have revealed that the maximum standard deviation of the signal gain and its relative zero drift are less than 0.02 V during the linear displacement measurement. Obviously, the testing results performed with the proposed module are more stable and accurate significantly. Finally, interferometer with the improved signal processing module is verified with the commercial interferometer. Experimental results have demonstrated that the difference of the maximum standard deviations between both interferometers is about 0.3  $\mu\text{m}$ .

Key word : Fabry-Perot interferometer, signal processing module, linear displacement measurement

## **1 Introduction**

Due to the demand on high precision measurements or positionings, submicro- or nanometer measurement technology becomes more relevant and necessary. The laser interferometer is a common measurement instrument to realize the calibration of the precision machine tools or the linear positioning of a stage. The signal processing quality is essential for determining the measurement accuracy of the laser interferometer employed for above-mentioned applications.

The usual commercial interferometer based on a non-common optical path structure is sensitive to environmental disturbances and mechanical

vibrations. To eliminate these errors, the proposed Fabry-Perot interferometer system arranged with the common optical path bears the characteristics being more insensitive to such fluctuations. To enhance the measurement stability and accuracy of the developed Fabry-Perot interferometer, its signal processing module has been modified.

In order to verify the feasibility of the optimized system, comparison measurements between the proposed Fabry-Perot interferometer and a commercial interferometers have been conducted. The comparison results analysed according to ISO 230-2 standard have shown that the difference in bidirectional system positioning deviation, repeatability and accuracy are less than 1  $\mu\text{m}$ . It is proved that the proposed system can be employed for high-precision displacement measurements or the calibration for machine tools.

## 2 Measurement Principle

The structure of the proposed Fabry-Perot interferometer with a common optical path shown in Figure 1, compose of the reference mirror and corner cube retroreflector (CCR). The arrangement of the corner cube retroreflector (CCR) realizes that the incident light and the reflected light parallel each other to improve alignment efficiency.

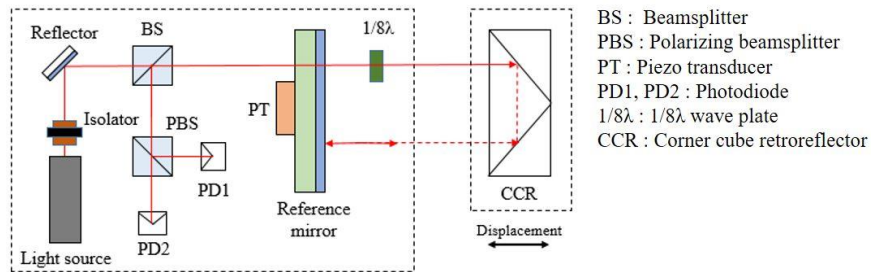


Figure 1: Improved optical structure of Fabry-Perot interferomter

## 3 Signal Processing Module

The interferometric signals are transmitted to two photodiodes which detect the intensity of the emerging interference beam. The signal amplification processing is shown in Figure 2. After the signal amplification processing, the signals will be processed with the low-pass filter circuit to eliminate the DC offset and avoid the signal leakage due to the DC drift, as shown in Figure 3.

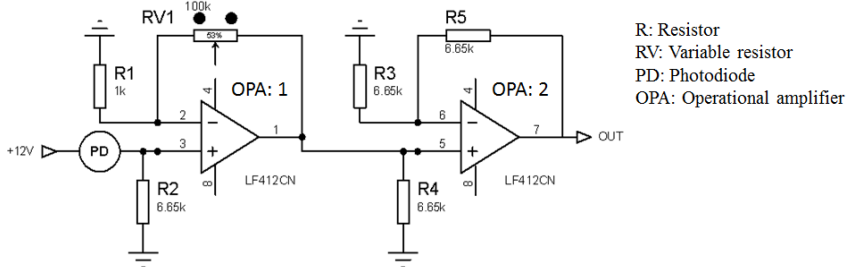


Figure 2: The signal amplification circuit

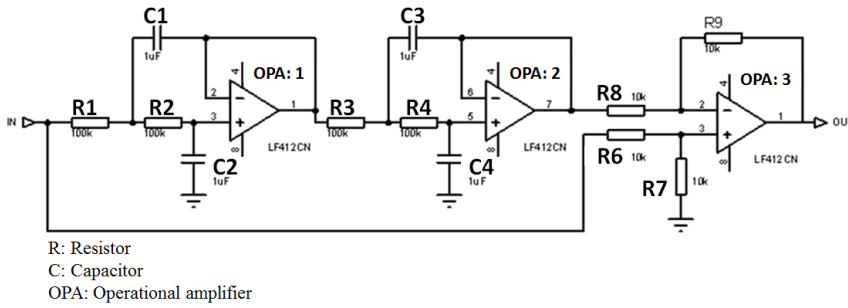


Figure 3: low-pass filter circuit

In this study the piezo transducer actuator is used to generate a micro-displacement of  $\pm\lambda/4$  in the optical cavity for the signal modulation. Its characteristics include fast response, low energy consumption, small size, and immunity to magnetic field interference.

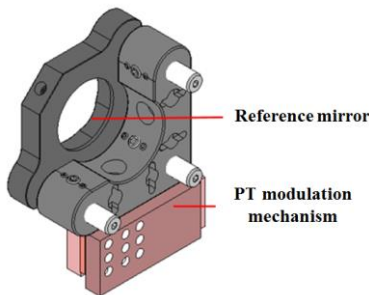


Figure 4: PT modulation mechanism

#### 4 Experimental results

Figure 5 has revealed that the maximum voltage deviation of the signal gain and its relative zero drift are less than 0.02 V. It means that the amplitude of the orthogonal signal was stable from start point (the distance from reference mirror to CCR is about 120 mm) to end point (the distance from reference mirror to CCR is about 220 mm). Consequently, the signal offset in initial point and end points are almost overlapped together.

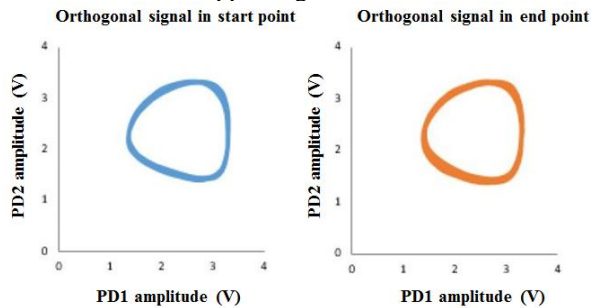


Figure 5: Orthogonal signal comparison between start and end point

In this experiment, the displacement of movement stage are measured by Fabry-Perot interferometer (FPI) and commercial interferometer (CI) in the same time. The results demonstrated that the positioning deviation of the comparison measurement between FPI and CI are less than  $0.3 \mu\text{m}$ , as shown in Figure 6.

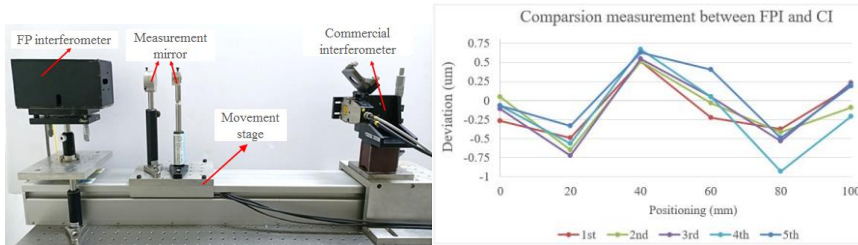


Figure 6: Comparison measurement between FPI and CI

## 5 Conclusion

This investigation based on the self-developed folded Fabry-Perot interferometer aims to the optimization and improvement of the corresponding interferometric signals. Results from the testings of the modified signal module and the comparison measurements demonstrated that the measuring performances have been distinctly improved. The Fabry-Perot interferometer integrated with this module can achieve the measurement demand of the submicron order.

## References

- [1] C.P. Chang, P.C. Tung, L.H. Shyu, Y.C. Wang, and E. Manske, "Modified Fabry-Perot interferometer for displacement measurement in ultra large measuring range", *Review of Scientific Instruments*, Vol. 84, pp.053105, 2013.
- [2] Anthony Chukwujekwu Okafor, Yalcin M. Ertekin, "Vertical machining center accuracy characterization using laser interferometer, *Journal of Materials Processing Technology*, Vol.105, 2000.
- [3] International Standard: ISO230-1, "Test code for machine tools -- Part 1: Geometric accuracy of machines operating under no-load or quasi-static conditions", Third edition, 2012.
- [4] International Standard: ISO230-2, "Test code for Machine Tools-Part 2: Determination of Accuracy and Repeatability of Positioning Numerically Controlled Axes", Third edition, 2014.
- [5] Texas Instruments, "LF412-N Low Offset, Low Drift Dual JFET Input Operational Amplifier", 2014.

# **Characterisation of an air plasma torch for in-situ surface processing**

Katherine Gobey 1, Adam Bennett 1&2, Nan Yu 2&3, Marco Castelli 2, Christopher Sansom 4, Peter King 4, Takuya Urayama 5

1. *Surface Engineering and Precision Institute, Cranfield University, UK*
2. *Cranfield Plasma Solutions, UK*
3. *Institute of Material and Processes, University of Edinburgh, UK*
4. *Renewable Energy Systems Centre, Cranfield University, UK*
5. *Adtec Plasma Technology Co., Ltd., Japan*

## **Abstract**

This study presents the characterisation of an atmospheric pressure plasma (APP) generated using a novel torch device created for cleaning of Concentrating Solar Power (CSP) heliostats. Optical emission spectroscopy (OES) is employed to investigate photonic intensity, and thus energy, of the plasma temporally and spatially. Plasma generated from air is shown to consist mostly of ionised nitrogen species at relatively low intensities, demonstrating the inefficiency of generating plasma from air. Spatial maps of air plasma show an uneven distribution of plasma over the measured area, indicating the need for either reconsideration of torch design, or development of an appropriate tool path to account for this. The relationship between plasma intensity and input parameters such as power and gas flow are investigated, with power shown to have a strong effect on intensity, whereas the effect of the gas flow rate was minimal. Intensity of the air plasma was shown to increase over a period of approximately one hour, which was dependant on the temperature of the input gas, showing the need to include a warm-up period before any processing is undertaken.

## **1 Introduction**

Plasma is an invaluable tool in industry and has a vast field of utilisation: for example in surface cleaning, etching, and surface energy modification for applications such as enhanced wettability and improved adhesion to a substrate [1][2][3][4]. Most frequently, plasma processing occurs under vacuum conditions, necessitating longer processing times, specialist equipment, and in turn higher costs. Atmospheric Pressure Plasma (APP) is a promising alternative

for a wide array of applications and is increasingly the subject of research for both conventional and novel applications, with interesting and favourable results reported in areas such as aerodynamics, generation of electromagnetic radiation (UV), biomedical applications[5][6]. As it does not necessitate a vacuum chamber, samples to be processed can be of any size or shape. It also provides the possibility of processing of samples in-situ with portable plasma systems, opening a huge avenue of applications.

APP, in particular of the Dielectric Barrier Discharge (DBD) design, are a field of increasing interest and research, as their comparatively simple design and ability to produce plasmas without bulky and expensive vacuum systems often seen in industrial applications of plasma, makes them an attractive prospect for the processing of various materials. However, generation of plasma outside of the vacuum systems typically employed in industrial applications presents challenges in obtaining and maintaining a plasma that is stable both spatially and temporally, where failure to do so can result in processing errors and repeatability issues. Consequently, characterisation of the plasma produced is an important tool in understanding and controlling plasma discharge characteristics.

Plasma generated at atmospheric pressure can suffer from temporal and spatial instability, as well as contamination from components in the air such as humidity [7], which can result in processing flaws and repeatability errors. Previous studies were carried out to understand the thermodynamic properties of RF plasma [8][9] and OES characterisation of microwave plasma [10][11], making them available for glass surface modification and polishing. In order to minimise these effects and create an adequately stable plasma, characterisation of the produced plasma was undertaken in this study, such that in process real-time adjustment of the input parameters can be made to control and counter instabilities as they arise.

## **2 Methodology**

### **2.1 Experimental set-up**

In this work, characterisation of the plasma was conducted via spectroscopy, a technique that detects the photons emitted from molecular and atomic transitions in the plasma that occur as a result of decay, when an electron in an excited species falls to a lower energy level, or when a free electron becomes bound to an atom [12]. Substances are generally able to undergo multiple energy transitions which make up emission spectra that are defined, unvarying, and unique to each element, allowing accurate analysis of the composition of a substance. Ultraviolet-visible spectroscopy was chosen as the emissions from air plasmas found in literature typically fall within this range, most prominently from the 2<sup>nd</sup> Positive system of Nitrogen, the major peaks of which occur between 295 nm and 449 nm [13].

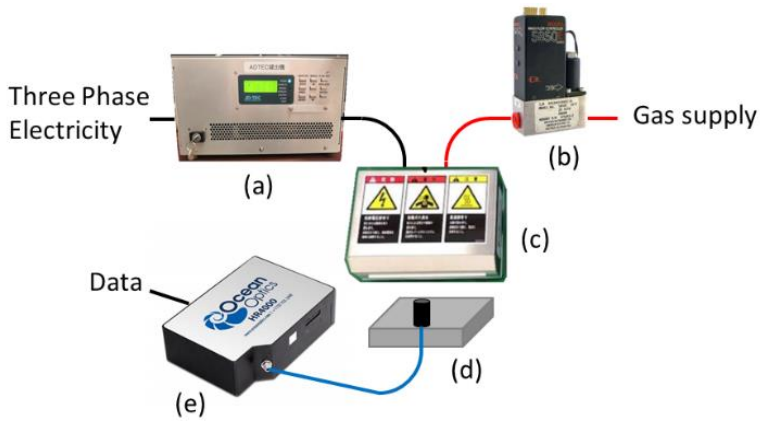


Figure 1: Experimental setup showing: a, generator; b, mass flow controller; c, plasma generating device (torch); d, motion stage; e, spectrometer.

In this work, Ocean Optics HR4000 spectrometers in the wavelength range 300-400 nm and 400-850 nm were used, with optical resolutions of 0.06 nm and 0.24 nm (FWHM) respectively, which were connected to a lens via fibre-optic cables. As displayed in Figure 1, this lens was mounted on a motion stage positioned 10 mm below the torch, to accommodate for the focal length of the lens. The torch was mounted on a bracket and remained stationary throughout. Spectroscopy was used to map the spatial intensity distribution of the plasma, with the lens moving in a series of passes below the torch, thus creating a map of emissions. Conversely, temporal stability was assessed with the lens positioned beneath the torch and retained stationary for the duration of data collection. For all analyses, the spectrometers were set to an integration time of 100 ms with a data refresh interval of 5 ms. All intensities listed are relative, not absolute.

## 2.2 Plasma parameters

Generation of plasma was obtained via bespoke equipment provided by Adtec Plasma Technology Co. Ltd.. such equipment is a dielectric barrier discharge (DBD) torch type, connected to a custom made generator through which power in the plasma was controlled via current, with values between 0.2 A and 0.9 A. The torch was cooled via an inbuilt cooling jacket using a circulating coolant solution at 20 °C. Flow of gas into the torch was controlled via a mass flow controller across the range 10 L/min to 60 L/min.

## 3 Results and discussion

### 3.1 Static spectrum

Data obtained from the static measurements of the plasma over the entire range measured are shown in Figure 2. The spectrum shows peaks that were identified from literature as originating from nitrogen species, with the most prominent

being at 337.13 nm from the (0,0) band of the nitrogen Second Positive system [13][14]. Ozone was produced, as indicated by its distinct smell as well as the triggering of an Ozone detector alarm placed around the measurement enclosure. However this was not detected in the emission data as ozone is a strong absorber of UV, therefore quantitative detection and analysis was not possible [15].

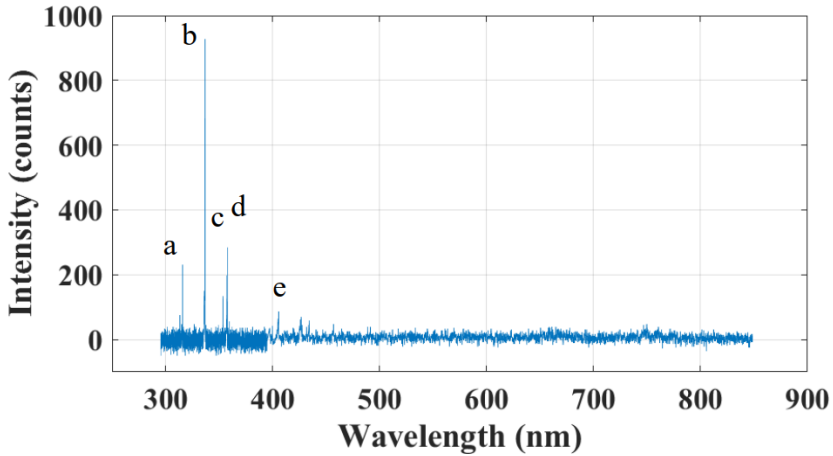


Figure 2: Emmission spectrum of air plasma with peaks labelled as follows: a, NO A-X (0,4); b, N<sub>2</sub> C-B (1,0); c, N<sub>2</sub> C-B (0,0); d, N<sub>2</sub> C-B (0,1); and e, N<sub>2</sub> C-B (0,3).

All subsequent analysis is of the aforementioned 337.13 nm peak in air generated plasmas owing to its higher intensity.

### 3.2 Temporal Stability

Emissions at 337.13 nm peak were analysed at torch start up and during a run for the subsequent two hours, as show in in Figure 3. Results demonstrated that, although the immediate ramp up is effectively instantaneous, it can take some time for the torch to become stabilised and to maximise plasma intensity, with average intensity increasing by 6.2 % over the first hour before stabilising. This effect was particularly evident during cold days, as the air supply to the torch is pulled from the external ambient air, which during the period of data collection was as low as -2 °C.

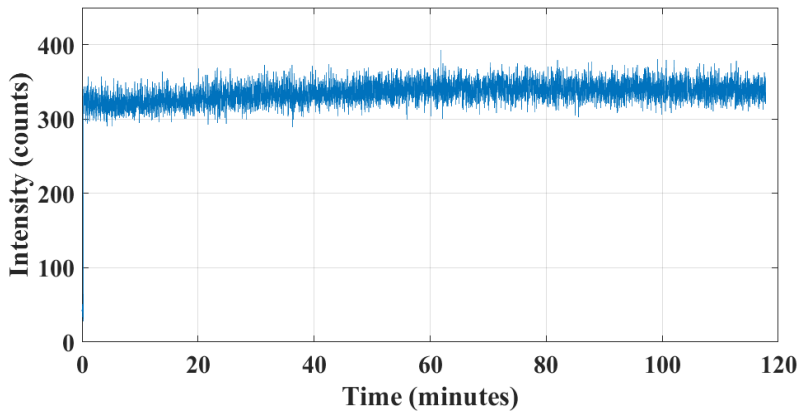


Figure 3: Temporal stability of plasma generated from air at a flow rate of 60 L/min, with current from the generator set to 0.9 A.

### 3.3 Spatial Mapping

When the intensity of the plasma is mapped spatially, 7 distinct regions of plasma generation were observed, as displayed in Figure 4 at the four combinations of parameters extremes (Gas flows of 60 L/min and 10 L/min, and currents of 0.9 A and 0.2 A). This distribution is as a result of the torch design, currently protected intellectual property therefore not discussed in this work.

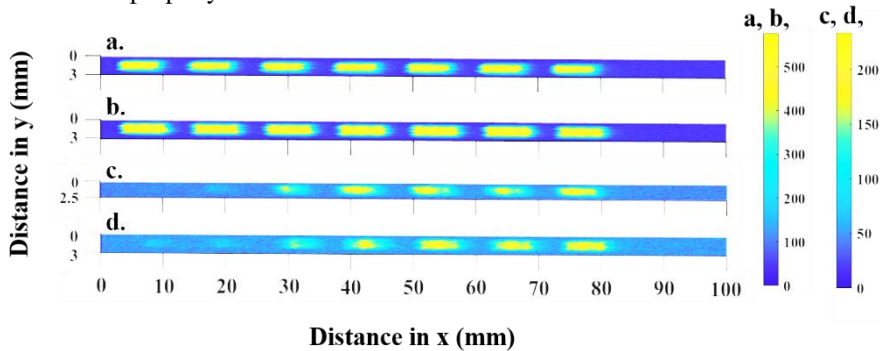


Figure 4. Spatial maps of intensity of 337.13 nm peak in plasma generated from air with the parameters: **a.** 60 L/min 0.9 A, **b.** 10 L/min 0.9 A, **c.** 60 L/min 0.2A, **d.** 10 L/min 0.2 A.

The intensity of these regions was shown to correlate strongly with the current from the generator (Figure 5), but was negligibly linked to the gas flow (Figure 6). Also observed was that the intensity of the plasma was linearly correlated to the current at values between 0.4 A and 0.9 A, however at 0.2 A and 0.3 A the plasma generated at the first two regions was significantly lower in intensity than in the regions 3 to 7. This may be due to a combination of the locations of the electrode structures within the torch, and the distribution of flow of air across these electrodes.

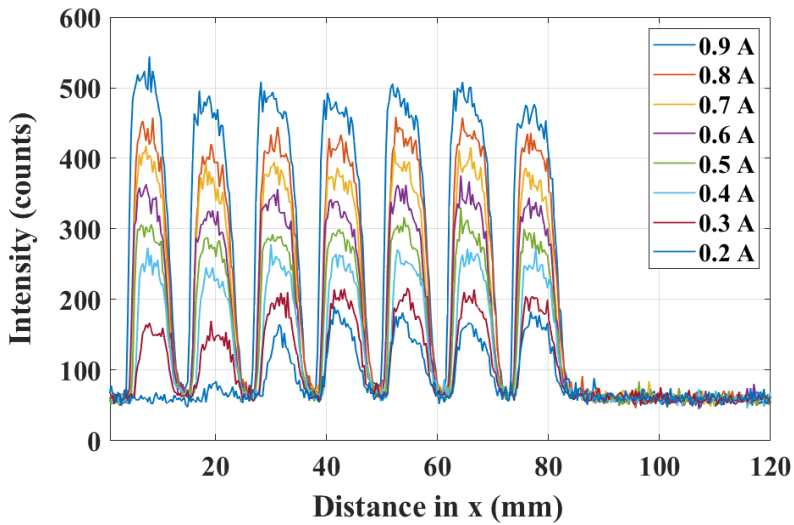


Figure 5. Intensity of the 337.13 nm peak in plasma generated with air at 60 L/min, with a range of currents.

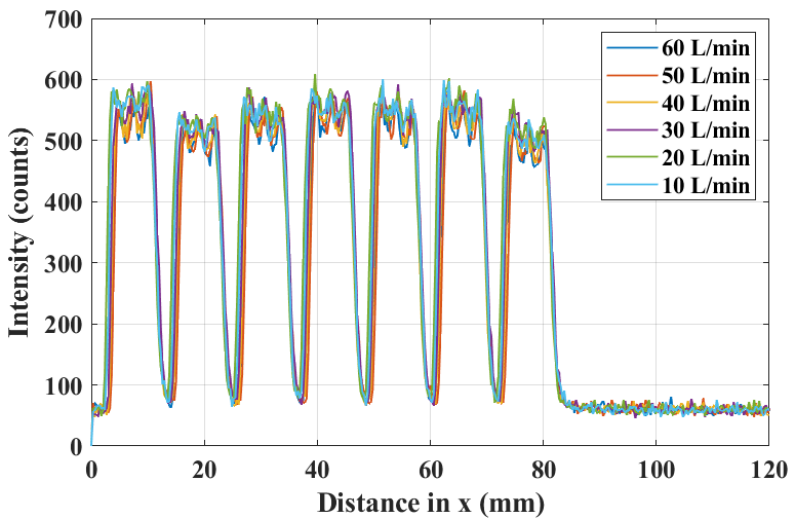


Figure 6. Intensity of the 337.13 nm peak in plasma generated with air at 0.9 A, with a range of gas flow rates.

#### 4 Conclusion and Future Work

The work presented here shows the value offered by spectroscopic characterisation of plasma. The knowledge gained from this work will provide invaluable feedback for optimal torch design and processing procedures. It has been demonstrated that, although DBDs are a robust technology that are generally able to produce a stable plasma, energy coupling and thus plasma intensity are affected by a number of input parameters and environmental conditions that

should be carefully understood and where possible controlled, in order to produce a plasma that is stable both spatially and temporally. For plasma processing, such a stable plasma is vital for processes that need to be controllable, repeatable, and precise. Whilst this work was conducted on a torch that was separate from any processing system, it is possible to mount a lens so that spectroscopy can be conducted in-situ, with appropriate data processing enabling real time characterisation of the plasma, which would allow instabilities to be immediately detected and plasma parameters adjusted accordingly to ensure stability in the plasma and reduce processing errors.

The authors envisage that future work will compound understanding of the distribution of plasma generated from the torch, and how this is affected by input parameters including temperature of the source gas. Three dimensional spatial maps would be beneficial to investigate intensity of the plasma within the plume for different stand-off distances between torch tip and substrate. This would reveal the effect of a parameter identified as key for processing by previous work [16]. Also to be investigated is the temperature of the plasma and its energy transfer mechanisms to the surface, knowledge of which could determine which materials could be processed and how thermal effects influence such processing

## **Acknowledgements**

This work was supported by the UK EPSRC under grant EP/K503241/1 (Centre for Doctoral Training in Ultra Precision Engineering) and EP/L016389/1 (Centre for Doctoral Training in Sustainable Materials and Manufacturing). The author would also like to thank ADTEC Plasma Technology & ADTEC Europe for providing financial and technical support and bespoke plasma equipment, and Cranfield Plasma Solutions for technical advice and knowledge.

## **References**

1. Kogelschatz U. Atmospheric-pressure plasma technology. *Plasma Physics and Controlled Fusion*. 2004; 46(12 B). Available at: DOI:10.1088/0741-3335/46/12B/006
2. Pochner K., Neff W., Lebert R. Atmospheric pressure gas discharges for surface treatment. *Surface and Coatings Technology*. 1995; 74–75(PART 1): 394–398. Available at: DOI:10.1016/0257-8972(95)08325-1
3. Malyshev M V., Donnelly VM., Downey SW., Colonell JI., Layadi N. Diagnostic studies of aluminum etching in an inductively coupled plasma system: Determination of electron temperatures and connections to plasma-induced damage. *Journal of Vacuum Science & Technology A: Vacuum, Surfaces, and Films*. 2000; 18(3): 849–859. Available at: DOI:10.1116/1.582266
4. Homola T., Matoušek J., Kormunda M., Wu LYL., Černák M. Plasma treatment of glass surfaces using diffuse coplanar surface barrier discharge in ambient air. *Plasma Chemistry and Plasma Processing*.

- 2013; 33(5): 881–894. Available at: DOI:10.1007/s11090-013-9467-3
5. Scholtz V., Pazlarova J., Souskova H., Khun J., Julak J. Nonthermal plasma - A tool for decontamination and disinfection. *Biotechnology Advances*. Elsevier Inc.; 2015; 33(6): 1108–1119. Available at: DOI:10.1016/j.biotechadv.2015.01.002
6. Kostov KG., Nishime TMC., Castro AHR., Toth A., Hein LRO. Surface modification of polymeric materials by cold atmospheric plasma jet. *Surface and Coatings Technology*. 2014; 314. Available at: DOI:10.1016/j.apsusc.2014.07.009
7. Pavlovich MJ., Clark DS., Graves DB. Quantification of air plasma chemistry for surface disinfection. *Plasma Sources Science and Technology*. 2014; 23(6). Available at: DOI:10.1088/0963-0252/23/6/065036
8. Yu N., Jourdain R., Gourma M., Shore P. Analysis of De-Laval nozzle designs employed for plasma figuring of surfaces. *International Journal of Advanced Manufacturing Technology*. 2016; 87(1–4): 735–745. Available at: DOI:10.1007/s00170-016-8502-y
9. Yu N., Yang Y., Jourdain R., Gourma M., Bennett A., Fang F. Design and optimization of plasma jet nozzles based on computational fluid dynamics. *International Journal of Advanced Manufacturing Technology*. The International Journal of Advanced Manufacturing Technology; 2020; 108(7–8): 2559–2568. Available at: DOI:10.1007/s00170-020-05568-4
10. Bennett A., Yu N., Castelli M., Chen G., Fang F. Etching characteristics of crystal quartz by surface wave microwave induced plasma. 2020; 1156807(November): 10. Available at: DOI:10.1117/12.2574947
11. Bennett A., Yu N., Castelli M., Chen G., Balleri A., Urayama T., et al. Characterisation of a microwave induced plasma torch for glass surface modification. *Frontiers of Mechanical Engineering*. 2020; Available at: DOI:10.1007/s11465-020-0603-5
12. Fantz U. Basics of plasma spectroscopy. *Plasma Sources Science and Technology*. 2006; 15(4). Available at: DOI:10.1088/0963-0252/15/4/S01
13. Pearse RWB., Gaydon AG. *The Identification of Molecular Spectra*. 1963.
14. Machala Z., Janda M., Hensel K., Jedlovský I., Leštinská L., Foltin V., et al. Emission spectroscopy of atmospheric pressure plasmas for biomedical and environmental applications. *Journal of Molecular Spectroscopy*. 2007; 243(2): 194–201. Available at: DOI:10.1016/j.jms.2007.03.001
15. Schulz-Von Der Gathen V., Buck V., Gans T., Knake N., Niemi K., Reuter S., et al. Optical diagnostics of micro discharge jets. *Contributions to Plasma Physics*. 2007; 47(7): 510–519. Available at: DOI:10.1002/ctpp.200710066
16. Castelli M. *Advances in optical surface figuring by reactive atom plasma (RAP)*. Cranfield University; 2012. Available at: <http://dspace.lib.cranfield.ac.uk/handle/1826/10420>

# **Novel Signal Processing Module of Fabry-Perot Interferometer**

Syuan-Cheng Chang<sup>1\*</sup>, Yung-Cheng Wang<sup>1</sup>, Chung-Ping Chang<sup>2</sup>,  
Teng-Chi Wu<sup>1</sup>, Bean-Yin Lee<sup>3</sup>

<sup>1</sup> *Department of Mechanical Engineering, National Yunlin University of Science and Technology, Yunlin 640, Taiwan*

<sup>2</sup> *Department of Mechanical and Energy Engineering, National Chiayi University, Chiayi 600, Taiwan*

<sup>3</sup> *Department of Mechanical and Computer-Aided Engineering, National Formosa University, Yunlin 632, Taiwan*

[\\*tso1147279@gmail.com](mailto:tso1147279@gmail.com)

## **Abstract**

In this investigation based on the self-developed folded Fabry-Perot interferometer, a novel signal processing module is optimized and integrated with others units. In order to acquire refined interferometric signals, the previous piezo transducer (PT) modulation mechanism is modified to improve the signal stability without complex adjustments or arrangements. With the aid of the improved signal processing module, the experimental results have revealed that the maximum standard deviation of the signal gain and its relative zero drift are less than 0.02 V during the linear displacement measurement. Obviously, the testing results performed with the proposed module are more stable and accurate significantly. Finally, interferometer with the improved signal processing module is verified with the commercial interferometer. Experimental results have demonstrated that the difference of the maximum standard deviations between both interferometers is about 0.3  $\mu\text{m}$ .

Key word : Fabry-Perot interferometer, signal processing module, linear displacement measurement

## **1 Introduction**

Due to the demand on high precision measurements or positionings, submicro- or nanometer measurement technology becomes more relevant and necessary. The laser interferometer is a common measurement instrument to realize the calibration of the precision machine tools or the linear positioning of a stage. The signal processing quality is essential for determining the measurement accuracy of the laser interferometer employed for above-mentioned applications.

The usual commercial interferometer based on a non-common optical path structure is sensitive to environmental disturbances and mechanical

vibrations. To eliminate these errors, the proposed Fabry-Perot interferometer system arranged with the common optical path bears the characteristics being more insensitive to such fluctuations. To enhance the measurement stability and accuracy of the developed Fabry-Perot interferometer, its signal processing module has been modified.

In order to verify the feasibility of the optimized system, comparison measurements between the proposed Fabry-Perot interferometer and a commercial interferometers have been conducted. The comparison results analysed according to ISO 230-2 standard have shown that the difference in bidirectional system positioning deviation, repeatability and accuracy are less than 1  $\mu\text{m}$ . It is proved that the proposed system can be employed for high-precision displacement measurements or the calibration for machine tools.

## 2 Measurement Principle

The structure of the proposed Fabry-Perot interferometer with a common optical path shown in Figure 1, compose of the reference mirror and corner cube retroreflector (CCR). The arrangement of the corner cube retroreflector (CCR) realizes that the incident light and the reflected light parallel each other to improve alignment efficiency.

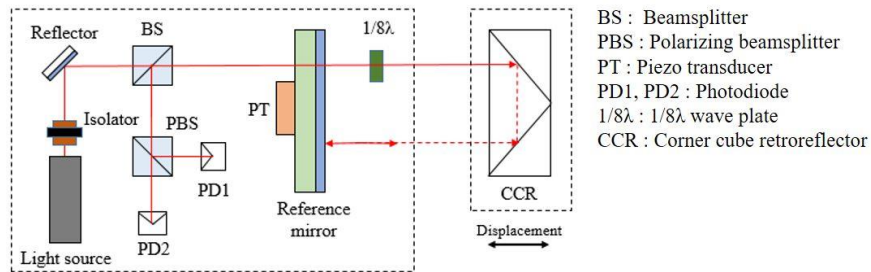


Figure 1: Improved optical structure of Fabry-Perot interferomter

## 3 Signal Processing Module

The interferometric signals are transmitted to two photodiodes which detect the intensity of the emerging interference beam. The signal amplification processing is shown in Figure 2. After the signal amplification processing, the signals will be processed with the low-pass filter circuit to eliminate the DC offset and avoid the signal leakage due to the DC drift, as shown in Figure 3.

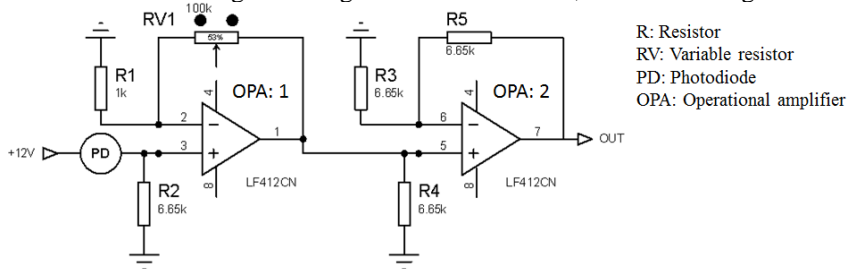


Figure 2: The signal amplification circuit

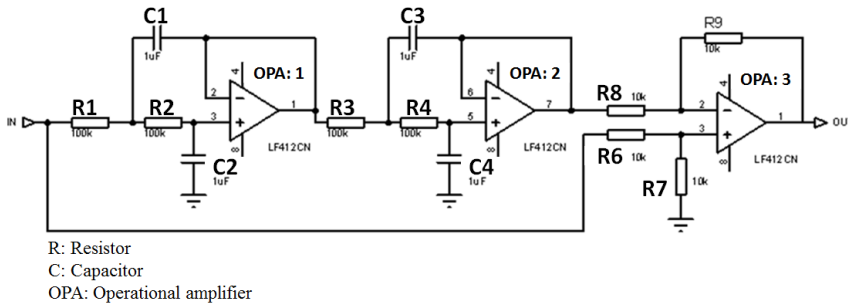


Figure 3: low-pass filter circuit

In this study the piezo transducer actuator is used to generate a micro-displacement of  $\pm\lambda/4$  in the optical cavity for the signal modulation. Its characteristics include fast response, low energy consumption, small size, and immunity to magnetic field interference.

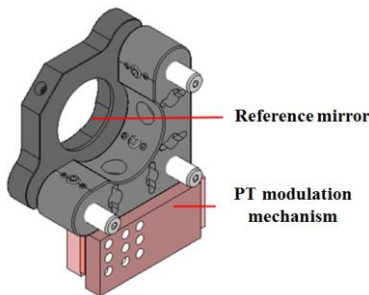


Figure 4: PT modulation mechanism

#### 4 Experimental results

Figure 5 has revealed that the maximum voltage deviation of the signal gain and its relative zero drift are less than 0.02 V. It means that the amplitude of the orthogonal signal was stable from start point (the distance from reference mirror to CCR is about 120 mm) to end point (the distance from reference mirror to CCR is about 220 mm). Consequently, the signal offset in initial point and end points are almost overlapped together.

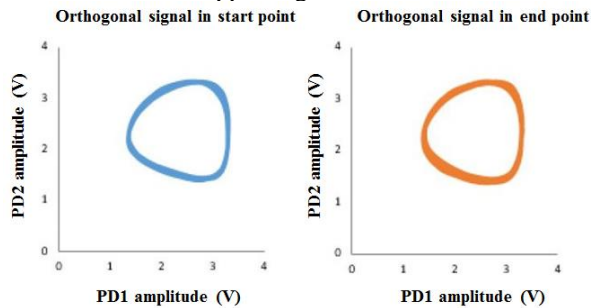


Figure 5: Orthogonal signal comparison between start and end point

In this experiment, the displacement of movement stage are measured by Fabry-Perot interferometer (FPI) and commercial interferometer (CI) in the same time. The results demonstrated that the positioning deviation of the comparison measurement between FPI and CI are less than 0.3  $\mu\text{m}$ , as shown in Figure 6.

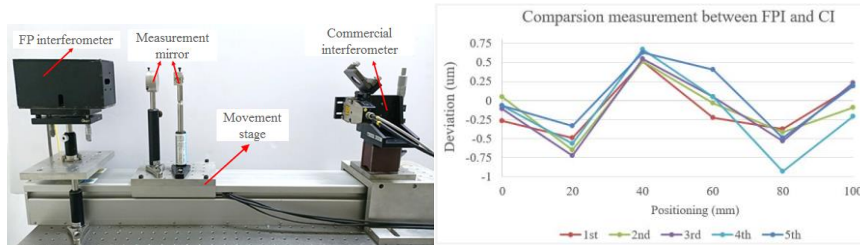


Figure 6: Comparison measurement between FPI and CI

## 5 Conclusion

This investigation based on the self-developed folded Fabry-Perot interferometer aims to the optimization and improvement of the corresponding interferometric signals. Results from the testings of the modified signal module and the comparison measurements demonstrated that the measuring performances have been distinctly improved. The Fabry-Perot interferometer integrated with this module can achieve the measurement demand of the submicron order.

## References

- [1] C.P. Chang, P.C. Tung, L.H. Shyu, Y.C. Wang, and E. Manske, "Modified Fabry-Perot interferometer for displacement measurement in ultra large measuring range", *Review of Scientific Instruments*, Vol. 84, pp.053105, 2013.
- [2] Anthony Chukwujekwu Okafor, Yalcin M. Ertekin, "Vertical machining center accuracy characterization using laser interferometer, *Journal of Materials Processing Technology*, Vol.105, 2000.
- [3] International Standard: ISO230-1, "Test code for machine tools -- Part 1: Geometric accuracy of machines operating under no-load or quasi-static conditions", Third edition, 2012.
- [4] International Standard: ISO230-2, "Test code for Machine Tools-Part 2: Determination of Accuracy and Repeatability of Positioning Numerically Controlled Axes", Third edition, 2014.
- [5] Texas Instruments, "LF412-N Low Offset, Low Drift Dual JFET Input Operational Amplifier", 2014.

# **Characterisation of an air plasma torch for in-situ surface processing**

Katherine Gobey<sup>1</sup>, Adam Bennett<sup>1,2</sup>, Nan Yu<sup>2,3</sup>, Marco Castelli<sup>2</sup>, Christopher Sansom<sup>4</sup>, Peter King<sup>4</sup>, Takuya Urayama<sup>5</sup>

- 1. Surface Engineering and Precision Institute, Cranfield University, UK*
- 2. Cranfield Plasma Solutions, UK*
- 3. Institute of Material and Processes, University of Edinburgh, UK*
- 4. Renewable Energy Systems Centre, Cranfield University, UK*
- 5. Adtec Plasma Technology Co., Ltd., Japan*

## **Abstract**

This study presents the characterisation of an atmospheric pressure plasma (APP) generated using a novel torch device created for cleaning of Concentrating Solar Power (CSP) heliostats. Optical emission spectroscopy (OES) is employed to investigate photonic intensity, and thus energy, of the plasma temporally and spatially. Plasma generated from air is shown to consist mostly of ionised nitrogen species at relatively low intensities, demonstrating the inefficiency of generating plasma from air. Spatial maps of air plasma show an uneven distribution of plasma over the measured area, indicating the need for either reconsideration of torch design, or development of an appropriate tool path to account for this. The relationship between plasma intensity and input parameters such as power and gas flow are investigated, with power shown to have a strong effect on intensity, whereas the effect of the gas flow rate was minimal. Intensity of the air plasma was shown to increase over a period of approximately one hour, which was dependant on the temperature of the input gas, showing the need to include a warm-up period before any processing is undertaken.

## **1 Introduction**

Plasma is an invaluable tool in industry and has a vast field of utilisation: for example in surface cleaning, etching, and surface energy modification for applications such as enhanced wettability and improved adhesion to a substrate [1][2][3][4]. Most frequently, plasma processing occurs under vacuum conditions, necessitating longer processing times, specialist equipment, and in turn higher costs. Atmospheric Pressure Plasma (APP) is a promising alternative

for a wide array of applications and is increasingly the subject of research for both conventional and novel applications, with interesting and favourable results reported in areas such as aerodynamics, generation of electromagnetic radiation (UV), biomedical applications[5][6]. As it does not necessitate a vacuum chamber, samples to be processed can be of any size or shape. It also provides the possibility of processing of samples in-situ with portable plasma systems, opening a huge avenue of applications.

APP, in particular of the Dielectric Barrier Discharge (DBD) design, are a field of increasing interest and research, as their comparatively simple design and ability to produce plasmas without bulky and expensive vacuum systems often seen in industrial applications of plasma, makes them an attractive prospect for the processing of various materials. However, generation of plasma outside of the vacuum systems typically employed in industrial applications presents challenges in obtaining and maintaining a plasma that is stable both spatially and temporally, where failure to do so can result in processing errors and repeatability issues. Consequently, characterisation of the plasma produced is an important tool in understanding and controlling plasma discharge characteristics.

Plasma generated at atmospheric pressure can suffer from temporal and spatial instability, as well as contamination from components in the air such as humidity [7], which can result in processing flaws and repeatability errors. Previous studies were carried out to understand the thermodynamic properties of RF plasma [8][9] and OES characterisation of microwave plasma [10][11], making them available for glass surface modification and polishing. In order to minimise these effects and create an adequately stable plasma, characterisation of the produced plasma was undertaken in this study, such that in process real-time adjustment of the input parameters can be made to control and counter instabilities as they arise.

## **2 Methodology**

### **2.1 Experimental set-up**

In this work, characterisation of the plasma was conducted via spectroscopy, a technique that detects the photons emitted from molecular and atomic transitions in the plasma that occur as a result of decay, when an electron in an excited species falls to a lower energy level, or when a free electron becomes bound to an atom [12]. Substances are generally able to undergo multiple energy transitions which make up emission spectra that are defined, unvarying, and unique to each element, allowing accurate analysis of the composition of a substance. Ultraviolet-visible spectroscopy was chosen as the emissions from air plasmas found in literature typically fall within this range, most prominently from the 2<sup>nd</sup> Positive system of Nitrogen, the major peaks of which occur between 295 nm and 449 nm [13].

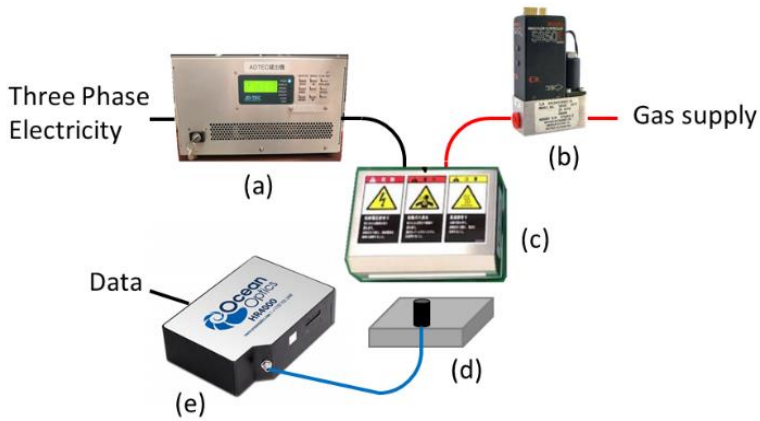


Figure 1: Experimental setup showing: a, generator; b, mass flow controller; c, plasma generating device (torch); d, motion stage; e, spectrometer.

In this work, Ocean Optics HR4000 spectrometers in the wavelength range 300-400 nm and 400-850 nm were used, with optical resolutions of 0.06 nm and 0.24 nm (FWHM) respectively, which were connected to a lens via fibre-optic cables. As displayed in Figure 1, this lens was mounted on a motion stage positioned 10 mm below the torch, to accommodate for the focal length of the lens. The torch was mounted on a bracket and remained stationary throughout. Spectroscopy was used to map the spatial intensity distribution of the plasma, with the lens moving in a series of passes below the torch, thus creating a map of emissions. Conversely, temporal stability was assessed with the lens positioned beneath the torch and retained stationary for the duration of data collection. For all analyses, the spectrometers were set to an integration time of 100 ms with a data refresh interval of 5 ms. All intensities listed are relative, not absolute.

## 2.2 Plasma parameters

Generation of plasma was obtained via bespoke equipment provided by Adtec Plasma Technology Co. Ltd.. such equipment is a dielectric barrier discharge (DBD) torch type, connected to a custom made generator through which power in the plasma was controlled via current, with values between 0.2 A and 0.9 A. The torch was cooled via an inbuilt cooling jacket using a circulating coolant solution at 20 °C. Flow of gas into the torch was controlled via a mass flow controller across the range 10 L/min to 60 L/min.

## 3 Results and discussion

### 3.1 Static spectrum

Data obtained from the static measurements of the plasma over the entire range measured are shown in Figure 2. The spectrum shows peaks that were identified from literature as originating from nitrogen species, with the most prominent

being at 337.13 nm from the (0,0) band of the nitrogen Second Positive system [13][14]. Ozone was produced, as indicated by its distinct smell as well as the triggering of an Ozone detector alarm placed around the measurement enclosure. However this was not detected in the emission data as ozone is a strong absorber of UV, therefore quantitative detection and analysis was not possible [15].

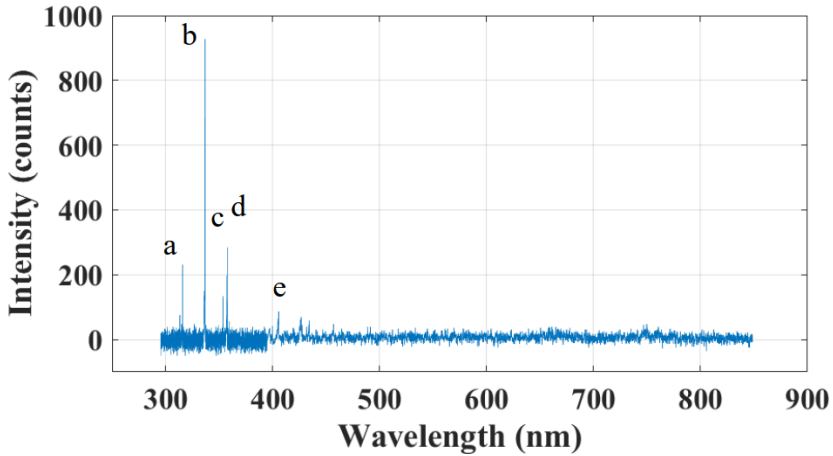


Figure 2: Emmission spectrum of air plasma with peaks labelled as follows: a, NO A-X (0,4); b, N<sub>2</sub> C-B (1,0); c, N<sub>2</sub> C-B (0,0); d, N<sub>2</sub> C-B (0,1); and e, N<sub>2</sub> C-B (0,3).

All subsequent analysis is of the aforementioned 337.13 nm peak in air generated plasmas owing to its higher intensity.

### 3.2 Temporal Stability

Emissions at 337.13 nm peak were analysed at torch start up and during a run for the subsequent two hours, as show in in Figure 3. Results demonstrated that, although the immediate ramp up is effectively instantaneous, it can take some time for the torch to become stabilised and to maximise plasma intensity, with average intensity increasing by 6.2 % over the first hour before stabilising. This effect was particularly evident during cold days, as the air supply to the torch is pulled from the external ambient air, which during the period of data collection was as low as -2 °C.

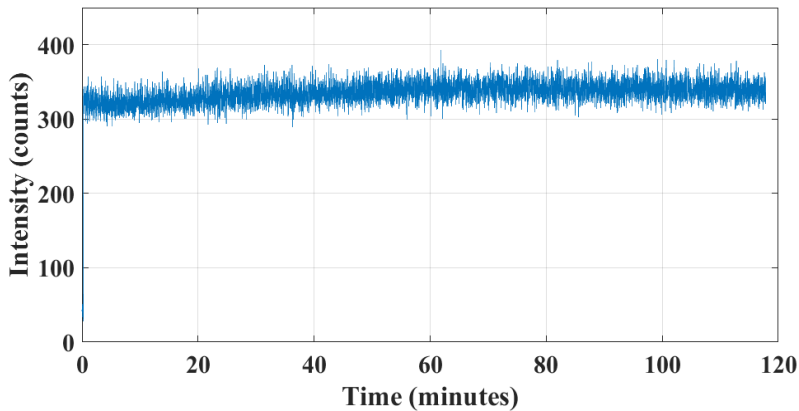


Figure 3: Temporal stability of plasma generated from air at a flow rate of 60 L/min, with current from the generator set to 0.9 A.

### 3.3 Spatial Mapping

When the intensity of the plasma is mapped spatially, 7 distinct regions of plasma generation were observed, as displayed in Figure 4 at the four combinations of parameters extremes (Gas flows of 60 L/min and 10 L/min, and currents of 0.9 A and 0.2 A). . This distribution is as a result of the torch design, currently protected intellectual property therefore not discussed in this work.

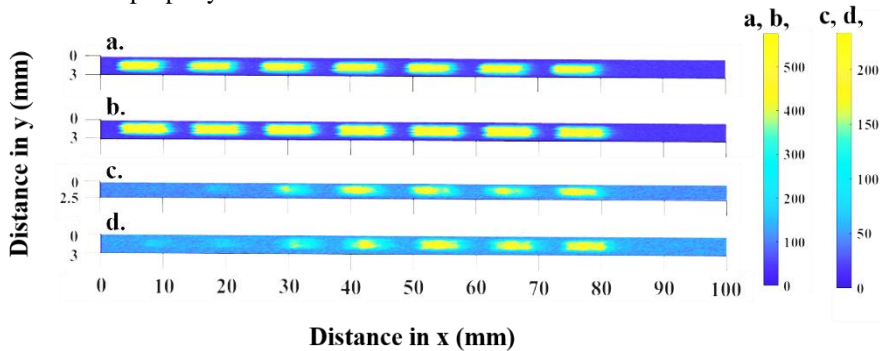


Figure 4. Spatial maps of intensity of 337.13 nm peak in plasma generated from air with the parameters: **a.** 60 L/min 0.9 A, **b.** 10 L/min 0.9 A, **c.** 60 L/min 0.2A, **d.** 10 L/min 0.2 A.

The intensity of these regions was shown to correlate strongly with the current from the generator (Figure 5), but was negligibly linked to the gas flow (Figure 6). Also observed was that the intensity of the plasma was linearly correlated to the current at values between 0.4 A and 0.9 A, however at 0.2 A and 0.3 A the plasma generated at the first two regions was significantly lower in intensity than in the regions 3 to 7. This may be due to a combination of the locations of the electrode structures within the torch, and the distribution of flow of air across these electrodes.

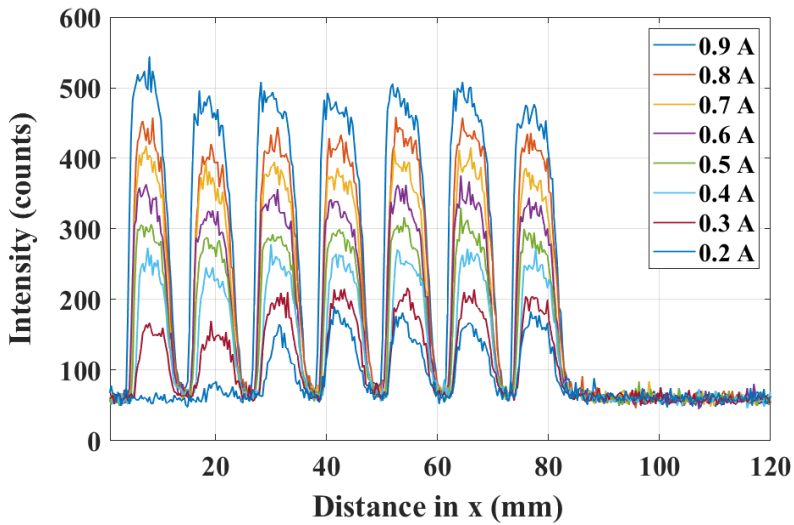


Figure 5. Intensity of the 337.13 nm peak in plasma generated with air at 60 L/min, with a range of currents.

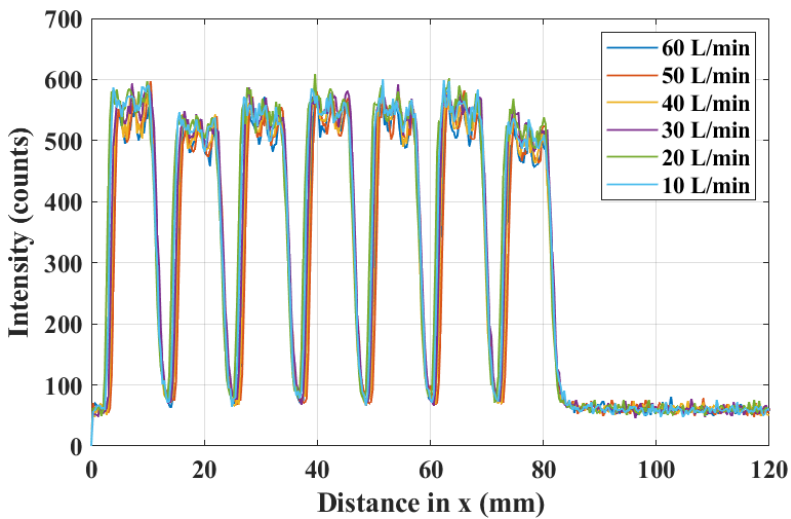


Figure 6. Intensity of the 337.13 nm peak in plasma generated with air at 0.9 A, with a range of gas flow rates.

#### 4 Conclusion and Future Work

The work presented here shows the value offered by spectroscopic characterisation of plasma. The knowledge gained from this work will provide invaluable feedback for optimal torch design and processing procedures. It has been demonstrated that, although DBDs are a robust technology that are generally able to produce a stable plasma, energy coupling and thus plasma intensity are affected by a number of input parameters and environmental conditions that

should be carefully understood and where possible controlled, in order to produce a plasma that is stable both spatially and temporally. For plasma processing, such a stable plasma is vital for processes that need to be controllable, repeatable, and precise. Whilst this work was conducted on a torch that was separate from any processing system, it is possible to mount a lens so that spectroscopy can be conducted in-situ, with appropriate data processing enabling real time characterisation of the plasma, which would allow instabilities to be immediately detected and plasma parameters adjusted accordingly to ensure stability in the plasma and reduce processing errors.

The authors envisage that future work will compound understanding of the distribution of plasma generated from the torch, and how this is affected by input parameters including temperature of the source gas. Three dimensional spatial maps would be beneficial to investigate intensity of the plasma within the plume for different stand-off distances between torch tip and substrate. This would reveal the effect of a parameter identified as key for processing by previous work [16]. Also to be investigated is the temperature of the plasma and its energy transfer mechanisms to the surface, knowledge of which could determine which materials could be processed and how thermal effects influence such processing

## **Acknowledgements**

This work was supported by the UK EPSRC under grant EP/K503241/1 (Centre for Doctoral Training in Ultra Precision Engineering) and EP/L016389/1 (Centre for Doctoral Training in Sustainable Materials and Manufacturing). The author would also like to thank ADTEC Plasma Technology & ADTEC Europe for providing financial and technical support and bespoke plasma equipment, and Cranfield Plasma Solutions for technical advice and knowledge.

## **References**

1. Kogelschatz U. Atmospheric-pressure plasma technology. *Plasma Physics and Controlled Fusion*. 2004; 46(12 B). Available at: DOI:10.1088/0741-3335/46/12B/006
2. Pochner K., Neff W., Lebert R. Atmospheric pressure gas discharges for surface treatment. *Surface and Coatings Technology*. 1995; 74–75(PART 1): 394–398. Available at: DOI:10.1016/0257-8972(95)08325-1
3. Malyshev M V., Donnelly VM., Downey SW., Colonell JI., Layadi N. Diagnostic studies of aluminum etching in an inductively coupled plasma system: Determination of electron temperatures and connections to plasma-induced damage. *Journal of Vacuum Science & Technology A: Vacuum, Surfaces, and Films*. 2000; 18(3): 849–859. Available at: DOI:10.1116/1.582266
4. Homola T., Matoušek J., Kormunda M., Wu LYL., Černák M. Plasma treatment of glass surfaces using diffuse coplanar surface barrier discharge in ambient air. *Plasma Chemistry and Plasma Processing*.

- 2013; 33(5): 881–894. Available at: DOI:10.1007/s11090-013-9467-3
5. Scholtz V., Pazlarova J., Souskova H., Khun J., Julak J. Nonthermal plasma - A tool for decontamination and disinfection. *Biotechnology Advances*. Elsevier Inc.; 2015; 33(6): 1108–1119. Available at: DOI:10.1016/j.biotechadv.2015.01.002
6. Kostov KG., Nishime TMC., Castro AHR., Toth A., Hein LRO. Surface modification of polymeric materials by cold atmospheric plasma jet. *Surface and Coatings Technology*. 2014; 314. Available at: DOI:10.1016/j.apsusc.2014.07.009
7. Pavlovich MJ., Clark DS., Graves DB. Quantification of air plasma chemistry for surface disinfection. *Plasma Sources Science and Technology*. 2014; 23(6). Available at: DOI:10.1088/0963-0252/23/6/065036
8. Yu N., Jourdain R., Gourma M., Shore P. Analysis of De-Laval nozzle designs employed for plasma figuring of surfaces. *International Journal of Advanced Manufacturing Technology*. 2016; 87(1–4): 735–745. Available at: DOI:10.1007/s00170-016-8502-y
9. Yu N., Yang Y., Jourdain R., Gourma M., Bennett A., Fang F. Design and optimization of plasma jet nozzles based on computational fluid dynamics. *International Journal of Advanced Manufacturing Technology*. The International Journal of Advanced Manufacturing Technology; 2020; 108(7–8): 2559–2568. Available at: DOI:10.1007/s00170-020-05568-4
10. Bennett A., Yu N., Castelli M., Chen G., Fang F. Etching characteristics of crystal quartz by surface wave microwave induced plasma. 2020; 1156807(November): 10. Available at: DOI:10.1117/12.2574947
11. Bennett A., Yu N., Castelli M., Chen G., Balleri A., Urayama T., et al. Characterisation of a microwave induced plasma torch for glass surface modification. *Frontiers of Mechanical Engineering*. 2020; Available at: DOI:10.1007/s11465-020-0603-5
12. Fantz U. Basics of plasma spectroscopy. *Plasma Sources Science and Technology*. 2006; 15(4). Available at: DOI:10.1088/0963-0252/15/4/S01
13. Pearse RWB., Gaydon AG. *The Identification of Molecular Spectra*. 1963.
14. Machala Z., Janda M., Hensel K., Jedlovský I., Leštinská L., Foltin V., et al. Emission spectroscopy of atmospheric pressure plasmas for biomedical and environmental applications. *Journal of Molecular Spectroscopy*. 2007; 243(2): 194–201. Available at: DOI:10.1016/j.jms.2007.03.001
15. Schulz-Von Der Gathen V., Buck V., Gans T., Knake N., Niemi K., Reuter S., et al. Optical diagnostics of micro discharge jets. *Contributions to Plasma Physics*. 2007; 47(7): 510–519. Available at: DOI:10.1002/ctpp.200710066
16. Castelli M. *Advances in optical surface figuring by reactive atom plasma (RAP)*. Cranfield University; 2012. Available at: <http://dspace.lib.cranfield.ac.uk/handle/1826/10420>

## INDEX OF AUTHORS

<b>A</b>		<b>K</b>	
Achiche, S	43	Keogh, P	14
Aguirre, G	67	King, P	103
Archenti, A	35	Knapp, W	23
Ariaga, N	25	<b>L</b>	
<b>B</b>		Laidler, I	18
Bennett, A	103	Laspas, T	35
Bilal, M	60	Lee, B-Y	99
<b>C</b>		Lin, Z	89
Castelli, M	103	Longstaff, A.P	78, 25, 54
Chang, C-P	99	Lopez de Lacalle, L.N	67
Chatelain, J-F	43	<b>M</b>	
Chen, Y	60	Mayer, J.R.R	43
Chen, Z	60	McLeay, T	17
Cheng S-C	99	Mian, N	78
Chuku, D	54	Mori, M	13
Colinas-Armijo, N	67	Moylan, S	15
<b>D</b>		<b>N</b>	
Dadbakhsh, S	89	Noakes, O	19
Danzl, R	94	<b>P</b>	
<b>F</b>		Pan, W	25
Ferrucci, M	20	<b>R</b>	
Fletcher, S	78, 25, 54	Rashid, A	89
Furness, T	54	Rimpault, X	43
<b>G</b>		<b>S</b>	
Gobey, K	103	Sansom, C	103
Gonzalez Bassante, M.K	35	Stocker, M	22
<b>H</b>		<b>T</b>	
Helmi, F	94	Theissen, N.A	35
Hu, L	60	<b>U</b>	
<b>I</b>		Urayama, T	103
Ihlenfeldt, S	16	Urlep, D	94
Iñigo, B	67		
Iqbal, A	78		
Ivory, C	19		

<b>W</b>	
Wang, Y-C	99
Wu, T-C	99
<b>X</b>	
Xing, K	43
<b>Y</b>	
Yu, N	103
<b>Z</b>	
Zangl, K	94
Zha, J	60
Zhao, X	89

This book is the edited proceedings for the Fourteenth International Conference on Laser Metrology, CMM and Machine Tool Performance, LAMDAMAP 2021.

The contributions cover the following topics:

- Machine Tools
- Design
- Process Control
- Additive Manufacturing and Standards
- Associated Measurement

---

Lamdmap 2021 was co-ordinated by [www.euspen.eu](http://www.euspen.eu)



ISBN: 978-0-9957751-8-3